FACULTY OF SCIENCE AND TECHNOLOGY

MASTER THESIS

Study programme / specialisation:
Petroleum Geosciences Engineering

The spring semester, 2022

Open

Author: Hanne Gilje

.....
(signature author)

Course coordinator:

Supervisor(s):
Nestor Cardozo (UiS)
Stuart Hardy (ICREA)
Long Wu (Equinor)

Thesis title:
Structural evolution of basement fault bounded fold structures using forward modelling methods: Application to the Beta structure in the Smeaheia area.

Credits (ECTS): 30

Keywords:

Smeaheia

Beta structure

Fault-bend folds

Discrete element modelling

Pages: 89

+ appendix: 8 pages

Stavanger, 14/06/2022

Structural evolution of basement fault bounded fold structures using forward modelling methods: Application to the Beta structure in the Smeaheia area.

by

Hanne Gilje

Master thesis
Presented to the Faculty of Science and Technology

The University of Stavanger
June 2022

Acknowledgements

I wish to express my sincere gratitude to my supervisor Nestor Cardozo for his guidance and expertise throughout this thesis. His valuable suggestions and encouragement are highly appreciated. I would also like to thank my co-supervisors, Stuart Hardy for his technical support, and Long Wu for his geological knowledge and guidance throughout this study. I would also like to express my gratitude to Lothar Schulte for his technical support with the Petrel software. Lastly, I would like to thank my fellow students for making these last five years a lot of fun, and my family and friends for their encouragement and support.

Abstract

In rift systems, extensional fault-related folds play an important part on the deformation pattern, and they are key to understand fault and sediment growth. In this thesis, the Beta structure in the Smeaheia area, Horda platform, northern North Sea is studied. This structure is an anticline in the hanging wall of the Øygarden fault complex (ØFC), which is a west-dipping, non-planar normal fault juxtaposing Precambrian basement on the east with Permian to Cretaceous sediments on the west. The thesis focuses on improving the understanding of the structural evolution of the Beta structure along two selected cross-sections, using seismic data in combination with kinematic modelling and discrete element modelling (DEM). From the DEM modelling, the Beta structure was formed by the normal movement of Permian-Jurassic strata along the non-planar ØFC, together with Late Jurassic-Early Cretaceous sedimentation. Fault bends are critical, with antithetic (to the ØFC) normal faults forming above concave upwards bends and offsetting the forelimb, and synthetic reverse or normal faults forming above convex upwards bends and offsetting the backlimb and crest of the structure. The fit of the DEM to the actual structure is better in section 2, which displays a more complex ØFC geometry with more bends than in section 1. However, extensional fault-bend folding alone cannot simulate a local syncline in the pre-growth and growth-strata close to the ØFC. Tectonic inversion and reactivation of the ØFC as a reverse fault during the Neogene improves the model fit, but it does not replicate the syncline. This “drag fold” is likely due to compaction and/or fault propagation folding. I test this last hypothesis using a trishear model.

Table of Contents

List of Figures

List of Tables

1 Introduction

Folds are important structural traps for both hydrocarbons and CO_2 storage (McHarg et al., 2020; Schlische, 1995). In rift systems, fault-related folds play an important part on the extensional deformation pattern, and they are key to understand fault and sediment growth (Alghuraybi et al., 2022; Ciftci & Bozkurt, 2008; Rotevatn & Jackson, 2014; Serck & Braathen, 2019).

The Horda Platform in the northern North Sea hosts the largest carbon capture and storage (CCS) project in Norway, namely the Northern Lights project. NE of the main CO_2 storage site, Aurora, the smaller Smeaheia prospect is located (Wu et al., 2021). Smeaheia is a fault block bounded by the Vette Fault Zone (VFZ) to the west, and the basement-bounding Øygarden Fault Complex (ØFC) to the east. Two storage prospects, Alpha and Beta, have been identified within the fault block (Mulrooney et al., 2020; Rahman et al., 2022; Wu et al., 2021). The subject of study in this thesis is the Beta structure, a north-south trending fault-related anticline parallel to the ØFC. The Beta structure has been interpreted as a fault-bend fold controlled by normal fault movement along the non-planar ØFC, during the Late Jurassic-Early Cretaceous rifting (Wu et al., 2021). However, there are still some uncertainties in whether the fold also was affected by minor local inversion during the Neogene (Wu et al., 2021).

Previous studies of the Beta structure have focused on structural and fault seal analysis (Wu et al., 2021) together with the structure's style and evolution (Mulrooney et al., 2020) using mainly seismic surveys and well logs. In this thesis, I analyze the evolution of the Beta structure from a mechanical point of view, using the discrete element method (DEM). I also run simple kinematic models (inclined shear and trishear) of the structure, to place the DEM modelling in context. The DEM is a well-established modelling technique which has been applied to a variety of geological problems in two- and three-dimensions. In this thesis, I use a 2D DEM implementation, cdem2D (Hardy, 2019), to model the Beta structure along two selected sections perpendicular to the ØFC, which capture the along-strike variation of the structure.

The results show that fault bends are critical in the formation of the Beta structure. Antithetic normal faults form above concave upwards bends and offsets the forelimb, while synthetic

reverse and normal faults form above convex upwards bends and offsets the backlimb and the crest of the structure. The DEM modelling shows a better fit with the actual structure in section 2, which displays more fault bends than section 1.

The main conclusions are:

- The ØFC geometry changes along strike (N-S), with an accompanying change of fold structure and secondary faulting in the hanging wall.
- The Beta structure was formed by normal movement along the non-planar ØFC, together with Late Jurassic-Early Cretaceous sedimentation.
- The local hanging wall syncline close to the ØFC cannot be replicated by extensional fault bend folding and tectonic inversion, and is likely due to compaction and/or fault propagation folding.
- The estimated displacement along the ØFC is varied: 0.8 km for inclined shear modelling, 1.0 km for DEM modelling, and 0.5 km for trishear-like modelling. However, neither the DEM nor the kinematic models are unique. It may be possible to fit the structure with a DEM model of lower fault displacement (e.g. 0.5 km), and fault propagation.

1.1 Objectives

The aim of this thesis is to gain a better understanding of the evolution of the Beta structure in the Horda platform, North Sea, using 2D DEM forward modelling and kinematic modelling. Two depth-converted seismic sections perpendicular to the Beta structure were the subject of modelling. These sections describe the along-strike variability of the Beta structure.

The main objectives of the thesis are:

- To conduct 2D DEM forward modelling of the Beta structure and analyze “normal fault-bend fold” versus “tectonic inversion/lateral compression” hypotheses, to see how they control the structure’ geometry, strain, and syn-kinematic strata above it.
- To compare the DEM forward modelling with kinematic (inclined shear and trishear) modelling of the structure.
- To summarize how the DEM modelling help us to better understand the evolution of the Beta structure and the basement-bounding ØFC.

2 Extensional fault related folds

Extensional fault related folds have been widely observed in rift systems worldwide (Deng & McClay, 2019; Shaw et al., 1997), and they have a significant influence on the location, thickness, and sediment partitioning in rift basins (Serck & Braathen, 2019). Gaining an understanding of the geometry and evolution of extensional fault-related folds is critical because they can provide information about the geometry and evolution of the associated faults, sediment routing and accommodation space, and potential targets for hydrocarbon exploration or CO_2 storage (Rotevatn & Jackson, 2014).

Extensional fault-related folds are a continuous form of deformation associated with fault propagation and interaction (H. Deng & McClay, 2019), and they form under normal fault stress regimes in extensional settings (Ciftci & Bozkurt, 2008). Extensional faulting can create a wide range of fold styles, which are often classified as longitudinal or transverse folds based on the hinge-line orientations with respect to the fault (Ciftci & Bozkurt, 2008; Deng & McClay, 2019; Schlische, 1995). In longitudinal folds, the hinge line is oriented parallel or sub-parallel to the associated normal fault. In transverse folds, the hinge line is oriented perpendicular to the associated fault (Ciftci & Bozkurt, 2008; Schlische, 1995). Although longitudinal and transverse folds are the most common in extensional settings, folds with oblique hinge orientations also exist, particularly in transtensional settings where the folds are oblique to the associated strike-slip faults (Ciftci & Bozkurt, 2008).

There are several processes resulting in extensional fault-related folding, and the combination of these processes results in mainly three types of folding: (1) extensional fault-propagation folding, (2) extensional fault-bend folding and (3) displacement gradient folding (Ciftci & Bozkurt, 2008). In extensional fault-propagation folding the region in front of the fault tip is folded into a monocline (Figure 1A), and then the monocline is breached by the propagating fault (Figure 1B). The folding results in distinctive hanging-wall synclines, and footwall anticlines (Ciftci & Bozkurt, 2008; Hardy, 2019; Phillips et al., 2020). Early in their formation, growth strata frequently show a pronounced thinning towards the fault-related fold, while latter after breaching, the growth strata become parallel or thicken towards the fault (Gawthorpe et al., 1997).

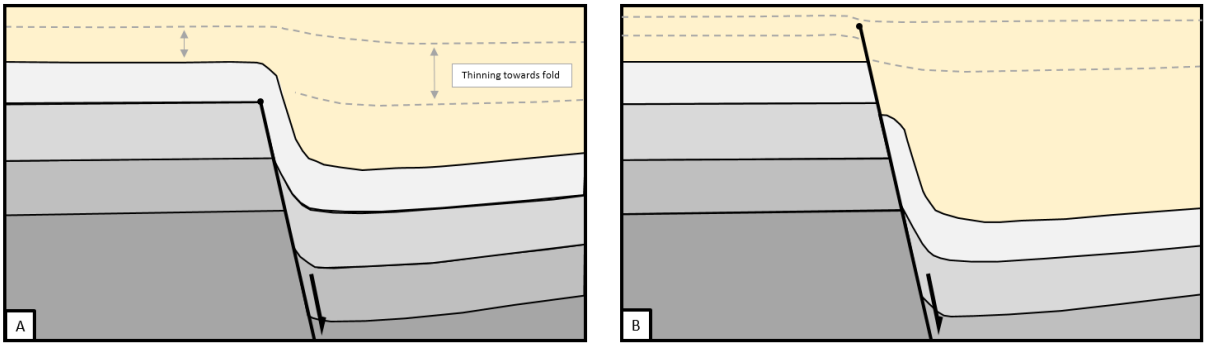

Figure 1: *(A) Initial stage of fault-propagation folding, creating a monocline. (B) Fault-propagation fold after breaching of the monocline. Modified from Phillips et al. (2020).*

In extensional fault-bend folding, the hanging wall moves downwards over a fault bend, which creates a void above the fault bend. The hanging wall will then collapse to fill the gap and thus become folded (Figure 2). Above concave-up fault bends, the hanging wall collapses along shear planes antithetic to the fault (Figure 2A). Above convex-up fault bends, the hanging wall collapses along shear planes synthetic to the fault (Xiao & Suppe, 1992) (Figure 2B).

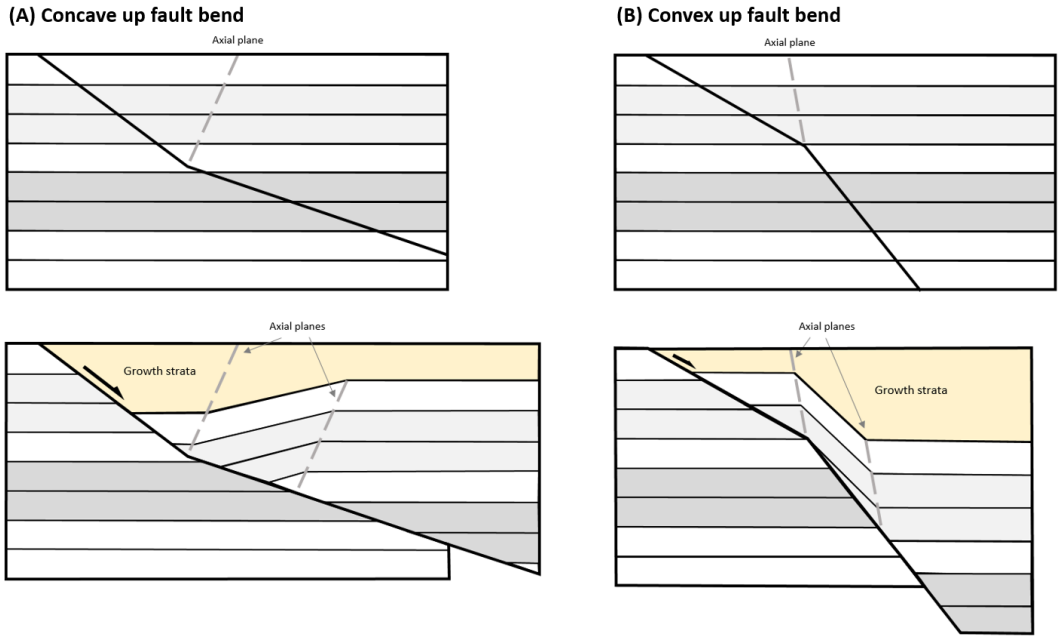

Figure 2: *(A) Extensional fault-bend folding above concave up fault bend, and (B) a convex up fault bend. Modified from Ciftci & Bozkurt (2008) who modified originally from Xiao & Suppe (1992).*

If the slip on the fault is mostly dip-slip, fault-propagation folds and fault-bend folds fall into the category of longitudinal folds, while displacement gradient folds fall into the category of transverse folds. Displacement gradient folds are controlled by lateral variation of

displacement along the fault surface, where the fault displacement gradually increases from zero at the fault tips to a maximum towards the fault center. This displacement gradient results in the deformation of the hanging wall into a broad syncline at the displacement maximum, and anticlines at the displacement minima (Ciftci & Bozkurt, 2008). The fold amplitude increases with displacement gradient.

There is a fourth category of extensional fault-related folds that is not much related to fault displacement, but compaction of the sediments above the normal fault. If the footwall is rigid, and the hanging wall is less consolidated and compacts more than the footwall, a compaction hanging wall syncline is formed (Fossen, 2016; Skuce, 1996) (Figure 3). This mechanism is worth considering in our case since the ØFC puts in contact basement in the footwall, with sediments in the hanging wall.

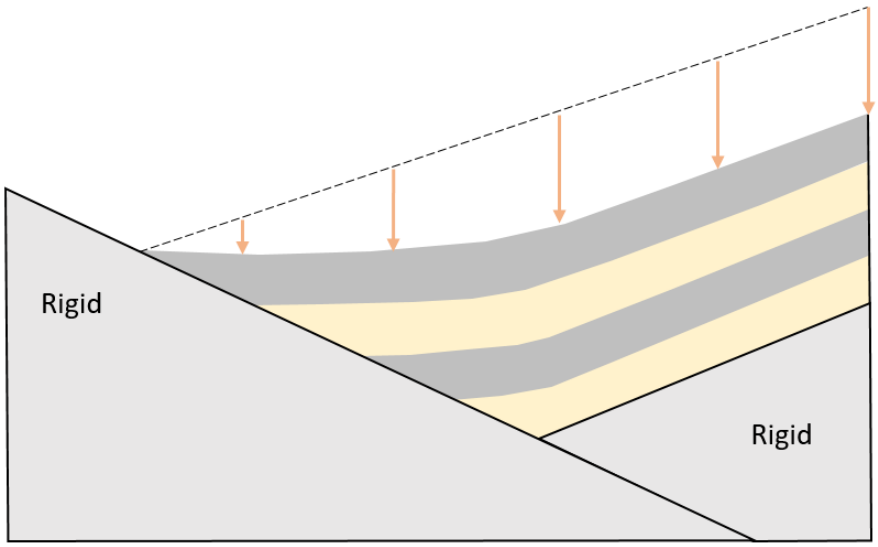

Figure 3: *Compaction hanging wall syncline formed by the hanging wall compacting more than the footwall. Modified from Fossen (2016).*

3 Geological setting

The northern North Sea encompasses an area of approximately 100,000 km^2 between the east Shetland Platform and the western Norway coastline (Phillips et al., 2019) (Figure 4). This area is characterized by large normal faults with N, NE, and NW orientations. The overall structure and fault pattern in the northern North Sea is a result of two major extensional phases, which created tilted fault-blocks and basins bounded by planar or listric faults (Færseth, 1996). The northern North Sea consists of a deep Cretaceous sub-basin, called the Viking Graben, in the central area, flanked by basin margin highs and platforms on either side of the sub-basin centre. The East Shetland Platform is located to the west and the Horda Platform to the east of the Viking Graben (Baig et al., 2019) (Figure 4). The Horda Platform is a N-S trending structural high located along the eastern margin of the northern North Sea (Whipp et al., 2013; Wu et al., 2021). It is bound to the east by the Øygarden Fault Complex (ØFC) and to the north by the Nordfjord-Sogn detachment (Whipp et al., 2013).

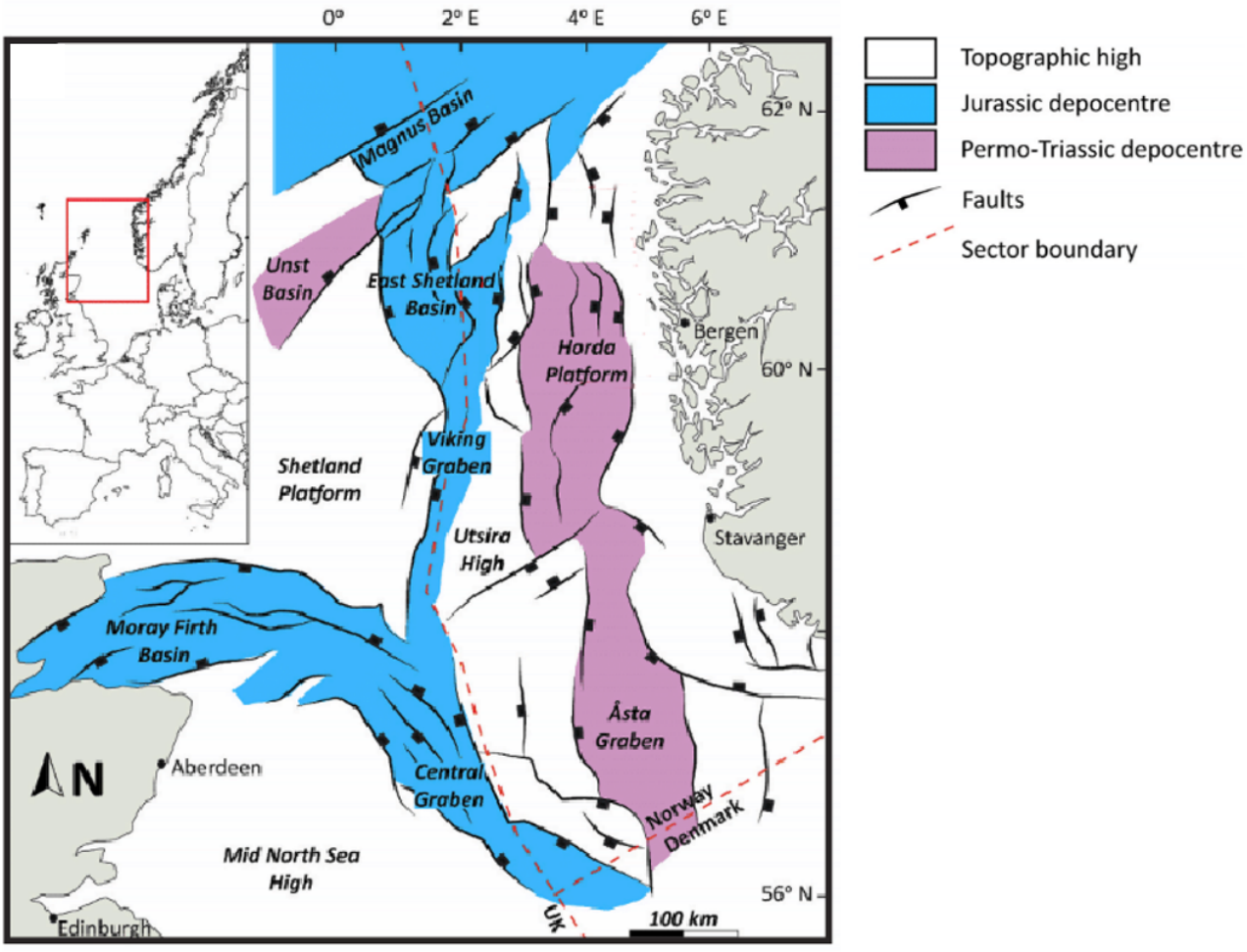

Figure 4: *Structural elements of the North Sea showing faults, basins and structural highs. Modified from Mulrooney et al. (2020).*

3.1 Tectonic framework

3.1.1 The northern North Sea

The crystalline basement of the northern North Sea was formed during the Proterozoic Sveconorwegian orogeny, before it was reworked due to compressional tectonics during the Caledonian and Variscan orogenies (Phillips et al., 2019; Whipp et al., 2013). Due to the collision between Baltica and Laurentia during the Caledonian orogeny, a series of low-angle intermontane basins were produced (Bell et al., 2014). These basins are filled with sandstones and conglomerates eroded from the Caledonian units (Vetti & Fossen, 2012).

The development of the North Sea can be divided into two major extensional events, namely the Permo-Triassic rifting and the Late Jurassic-Early Cretaceous rifting (Aker et al., 2021; Færseth, 1996). Both phases of extension were of roughly the same importance in the development of the North Sea. The Permo-Triassic rifting affected the total width of the northern North Sea, while the Late Jurassic to Early Cretaceous rifting was more localized in the Viking and Sogn grabens (Færseth, 1996).

The first rifting phase occurred during the Late Permian to Early Triassic and was triggered by the break-up of Pangea. E-W extension affected the northern North Sea, resulting in the formation of a N-S basin. This basin consists of easterly tilted half-grabens bounded by major west-dipping, basement-involved normal faults (Bell et al., 2014; Duffy et al., 2015; Whipp et al., 2013). After the first rifting phase, there was a ca. 70 Myr period of relative tectonic quiescence and post-rift thermal subsidence (Phillips et al., 2019; Whipp et al., 2013). Thermal doming during the Early to Middle Jurassic led to erosion of strata across large parts of the North Sea (Phillips et al., 2019).

The collapse of the thermal dome marks the start of the second rifting phase, which lasted from the Late Jurassic to Early Cretaceous (Phillips et al., 2019). This collapse of the dome resulted in the trilete North Sea rift system consisting of the Viking Graben, Central Graben, and Moray Firth (Bell et al., 2014) (Figure 4). The general strike of the faults in the North Sea is N-S, with some NE-SW striking structures. The direction of the extension during the second rifting phase is uncertain, with some studies stating that the extension direction was similar to the E-W extension of the first rifting phase, while other studies suggest that the

extension direction changed to NW-SE during the second rifting phase (Bell et al., 2014; Phillips et al., 2019).

The second rifting phase was followed by a period of thermal subsidence during the Late Cretaceous to Early Paleocene (Baig et al., 2019; Bell et al., 2014; Phillips et al., 2019; Whipp et al., 2013). In the northern North Sea, deposition of siliciclastics continued during the post-rift until the Quaternary. The northern North Sea was dominated by tectonic subsidence during the Late Paleocene-Eocene, and sediments from the uplifted basin margin areas to the west were eroded and deposited in the basin. The area experienced eastward sediment progradation, which continued during the Miocene-Pliocene. During the Quaternary, the sediment progradation direction shifted to the east as SW Norway became the major sediment source area (Baig et al., 2019).

3.1.2 Horda Platform

The Horda Platform consists of a series of easterly tilted half-grabens bounded by large displacement, NS normal faults (Figure 4). The half-grabens contain pre-Jurassic syn-rift strata overlain by strata deposited between the Jurassic and Late Jurassic-Early Cretaceous rifting events. The pre-rift strata are overlain by a package of Late Jurassic-Early Cretaceous syn-rift strata (Whipp et al., 2013). The structure of the Horda Platform primarily developed during the Permo-Triassic rifting phase, evidenced by the large half-grabens with Early Triassic synsedimentary infill (Stewart et al., 1995).

The Troll field is located on the northwestern edge of the Horda Platform. The field is located within three main tilted fault blocks, and is divided into three provinces, namely the Troll East, the Troll West gas province, and the Troll West oil province (Wu et al., 2021) (Figure 5). The fault blocks of the Troll Field were rotated during the Late Jurassic to Early Cretaceous rifting and have an eastward dip. The shallow-marine sandstones of the Sognefjord and Fensfjord formations are the main reservoirs of the Troll Field, and they are sealed by the Upper Jurassic to Lower Tertiary mudstones and marls (Horstad & Larter, 1997). On a geological scale, the presence of the Troll Field reveals a sealed system, even during episodes of tilting and hydrocarbon re-migration in the Neogene (Wu et al., 2021).

The Smeaheia fault block is situated east of the Troll Field. Smeaheia is the easternmost fault block within the Horda Platform, and located between the VFZ to the west and the ØFC to the east (Mulrooney et al., 2020; Rahman et al., 2022; Wu et al., 2021) (Figure 5). The Smeaheia block consists of two structural three-way closures named Alpha and Beta. These structures were penetrated by the wells 32/4-1 and 32/2-1, respectively (Rahman et al., 2022; Wu et al., 2021) (Figure 5). The stratigraphy and faulting styles of the Smeaheia fault block are similar to the Troll fault blocks, but the Smeaheia fault block has experienced more uplift and erosion (Wu et al., 2021).

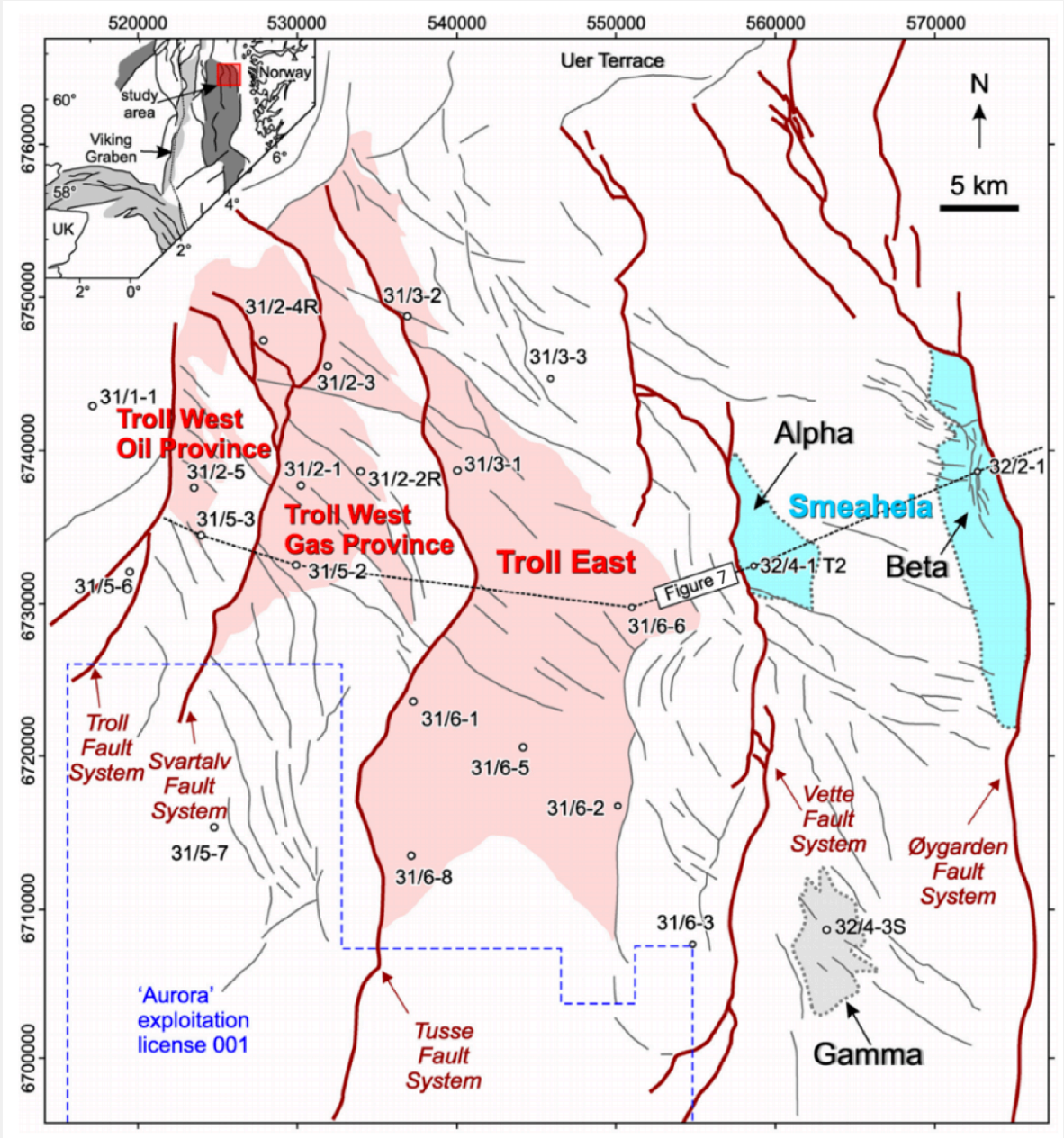

Figure 5: *Structural map of the Horda Platform area. The map includes main faults, the Troll Field, the Aurora CO_2 storage license boundary, the two structures Alpha and Beta within the Smeaheia fault block, and the wells in the area. Location of the section in Figure 7 is also shown. Modified from Wu et al. (2021).*

3.2 Stratigraphic framework

3.2.1 Permo-Triassic

The Permo-Triassic unit is of approximately Asselian to Rhaetian in age and consists of the Hegre Group (Figure 6). The non-marine clastic Hegre Group consists of sandstones and mudstones and is considered the lower part of the pre-rift unit (C. Deng et al., 2017; Whipp et al., 2013).

3.2.2 Lower to Middle Jurassic

The Lower to Middle Jurassic unconformably overlies the Permo-Triassic, and consists of the Statfjord, Dunlin and Brent Groups (Figure 6). These groups are considered the upper part of the pre-rift unit and were deposited in a fluvio-deltaic to shallow marine environment (C. Deng et al., 2017; Whipp et al., 2013).

3.2.3 Middle Jurassic to Lower Cretaceous

The Middle Jurassic to Early Cretaceous syn-rift sequence consists of the Viking Group, which encompasses the shallow marine clastic Krossfjord, Fensfjord and Sognefjord formations (Figure 6). These formations interfinger basinward with the fine-grained shallow marine sandstones of the Heather Formation (Mulrooney et al., 2020; Rahman et al., 2022; Stewart et al., 1995; Whipp et al., 2013). During the Late Kimmeridgian to Late Berriasian, the deep-marine mudstones of the Draupne Formation were deposited as result of flooding of the North Sea Basin (Whipp et al., 2013).

3.2.4 Cretaceous

The Viking Group is capped by the Base Cretaceous Unconformity (BCU) which usually divides the syn-rift and post-rift units in the North Sea. However, minor Cretaceous reactivation caused vertical movements on some large faults (Mulrooney et al., 2020). The BCU is overlain by the deep-water clastics and carbonates of the Cromer Knoll and Shetland groups deposited during the Cretaceous (Mulrooney et al., 2020; Whipp et al., 2013) (Figure 6).

3.2.5 Paleogene

The Paleogene unit consists of the siliciclastic-dominated Rogaland and Hordaland groups (Figure 6). Both of these groups are mainly sourced from the uplifted Shetland Platform and some local sediment source areas in western Norway (Baig et al., 2019; Wu et al., 2021).

3.2.6 Neogene

During Neogene, the Horda Platform was uplifted and eroded, and unconformably overlain by the Nordland Group. The Nordland Group is mainly composed of Quaternary post-glacial deposits (Wu et al., 2021).

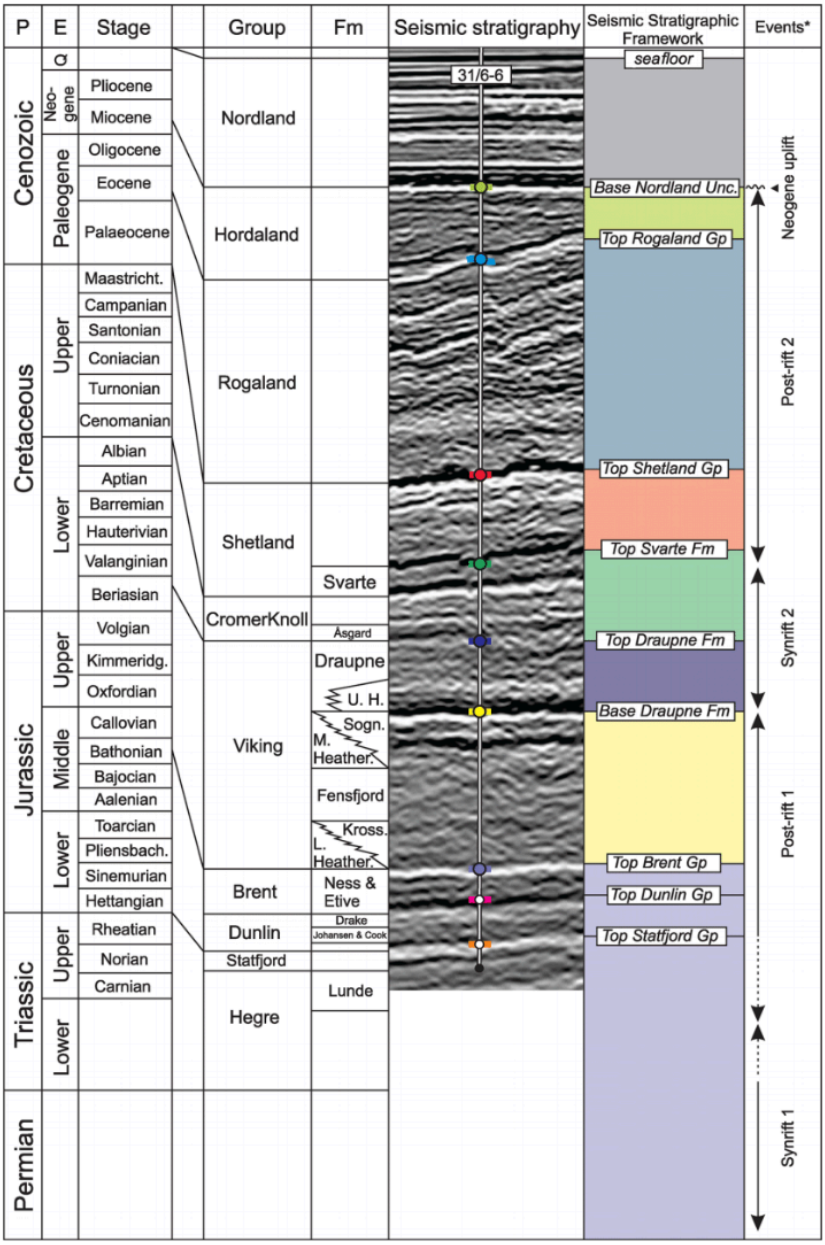

Figure 6: *Tectonostratigraphic chart of the Troll-Smeaheia area. From Wu et al. (2021).*

3.3 The Beta structure

This thesis focuses on the Beta structure, which is in the Smeaheia area, east of the Troll Field (Figures 5 and 7). The Beta structure is a north-south-trending fold parallel to the ØFC, where the Mesozoic strata are juxtaposed against the basement across the ØFC. The basement in the study area can be correlated to outcrops exposed in the western area of Bergen, which consist of pre-Cambrian granitic gneiss and migmatites (Wu et al., 2021). Complex fault systems have been observed in the sediments above the basement on the footwall side, indicating that the basement is fractured and faulted (Lauritsen et al., 2018). This is also supported by the highly fractured basement of the onshore Bergen area (Wu et al., 2021).

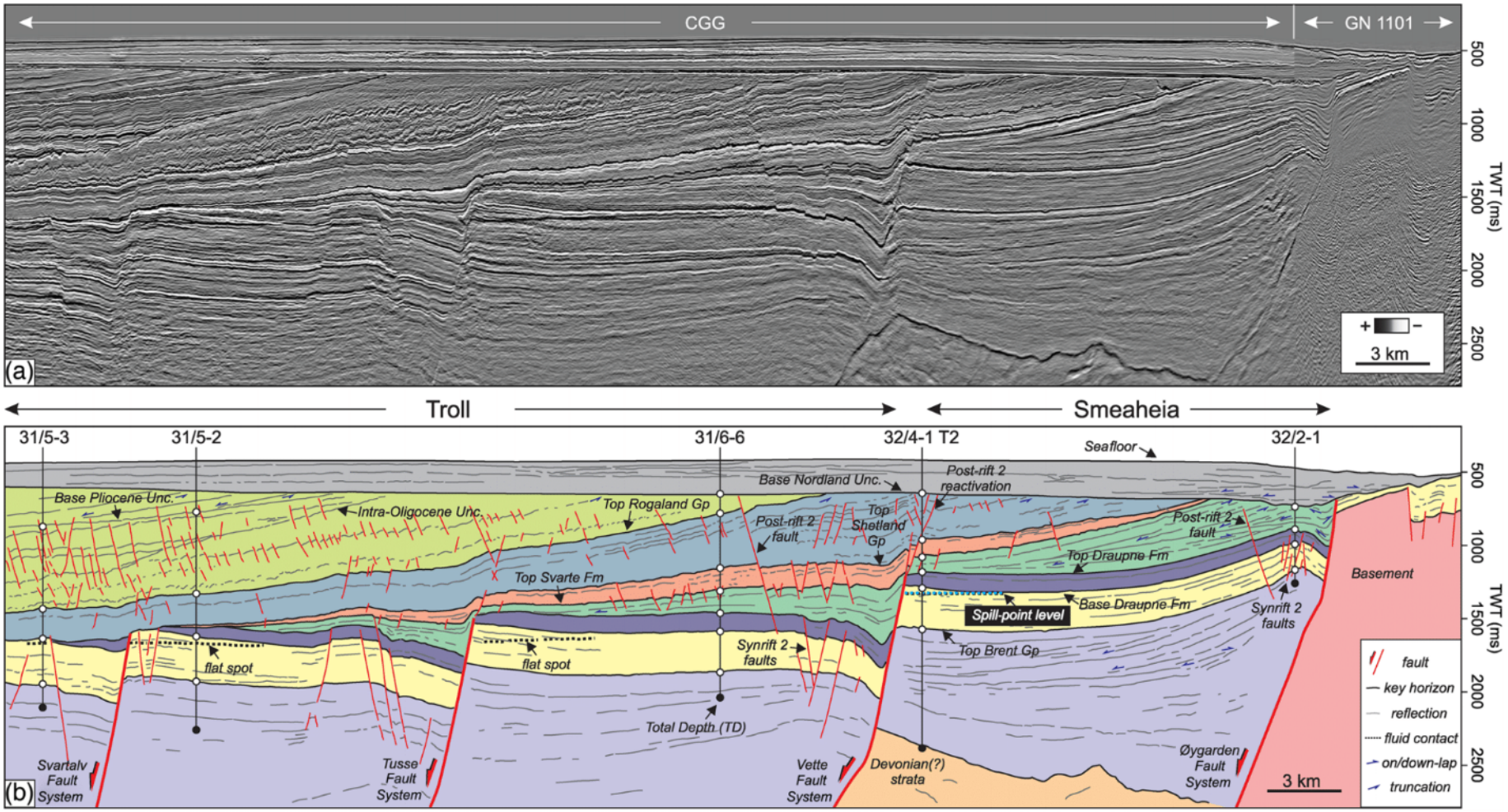

Figure 7: *(a) Uninterpreted seismic line of the Troll-Smeaheia area. Location of the section is in Figure 5. (b) Interpreted seismic section with well control and stratigraphic framework as in Figure 6. The vertical exaggeration (VE) of the section is approximately 6.0. From Wu et al. (2021).*

Two growth Upper Jurassic-Lower Cretaceous strata sequences, GP1 and GP2 (Figure 8), are observed in the Beta structure. These growth sequences are separated by the top Draupne Fm (base of the Cromer Knoll Group, Figure 6), which is an unconformity (marked by dashed line in Figure 8). Thus, the Beta structure experienced at least two folding events during the second synrift phase, as suggested by the two growth packages (Wu et al., 2021). Wu et al. (2021) interprets the Beta structure to have been formed as an extensional fault-bend fold above the non-planar ØFC, during the Late Jurassic-Early Cretaceous rifting. This interpretation is consistent with the synrift 2 normal faults observed in the core of the Beta structure (Figures 7 and 8). In addition, there might have been a phase of minor local inversion and uplift during the Neogene (Figure 6). However, no folding or faulting have been identified above the Base Nordland unconformity (Wu et al., 2021).

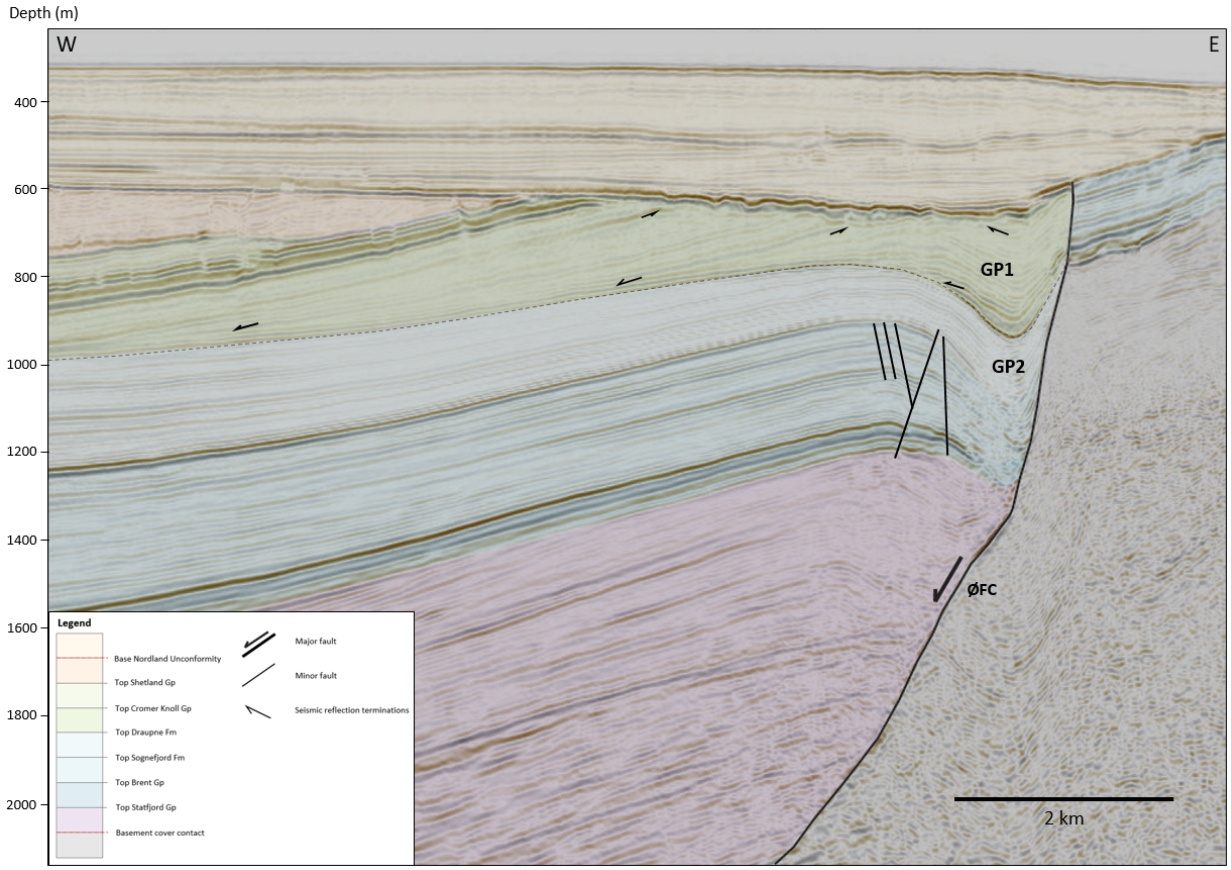

Figure 8: *E-W depth-converted seismic section through the Beta structure showing the stratigraphic units, the ØFC and minor faults, the two growth packages GP1 and GP2, and truncations, onlaps and downlaps marked with arrows. The VE of the section is 4.0. This is section 1 used in the modelling, and the location of this section is in Figure 9.*

3.3.1 Importance of the Beta structure

Carbon capture and storage (CCS) has become an important activity for reducing CO_2 emissions and achieve the global climate goals of the Paris Agreement (Michie et al., 2021; Wu et al., 2021). The Northern Lights Project is under development as the first full-scale CCS project in the Norwegian sector. The main CO_2 storage site in this project is Aurora, which is in tilted fault blocks, down-dip to the Troll Field and SW of the Smeaheia area (Wu et al., 2021) (Figure 5). Since Smeaheia is located between the Aurora storage site and the onshore CO_2 terminal (Figure 5), and it has sufficient storage capacity and great reservoir quality, the area has become an important site for additional CO_2 storage on a temporal or permanent basis (Michie et al., 2021; Wu et al., 2021). Both the Alpha and Beta are potential storage prospects. It is envisaged that the CO_2 will be injected into Alpha, and then it will migrate up-dip and accumulate in Beta (Mulrooney et al., 2020). However, since the Beta structure is right against fractured and weathered basement on the footwall of the ØFC, it has large uncertainties. Certainly, gaining an understanding of the structural evolution of the structure is critical. For example, did the structure experience tectonic inversion in the Neogene, or can the structure be entirely explained by normal faulting during the Late Jurassic-Early Cretaceous? That certainly has implications for evaluating the sealing (both top and fault seal) of the structure.

4 Data and methodology

4.1 Smeaheia Dataset

The dataset used in this thesis was downloaded from the online portal CO_2 DataShare, where reference datasets from pioneering CO_2 storage projects are publicly accessible (CO2 DataShare, 2022). The Smeaheia dataset includes two subsurface reports, 2D and 3D seismic data, horizons, surfaces, fault sticks, a velocity model, simulation models, well logs, well reports, geomechanical data and stress model, and pressure and temperature data. In this thesis, the 3D seismic survey GN1101 was used. This seismic survey was collected by Gassnova in 2011, and covers an area of 442.25 km^2, including the two CO_2 storage prospects of the Smeaheia area, Alpha and Beta (Figure 9). Two wells have been drilled in the Smeaheia area: the well 32/4-1 penetrating the Alpha structure, and the well 32/2-1 penetrating the Beta structure (Mulrooney et al., 2020) (Figure 9). The tops for these wells were imported from NPD FactPages (NPD, 2002, 2010) .

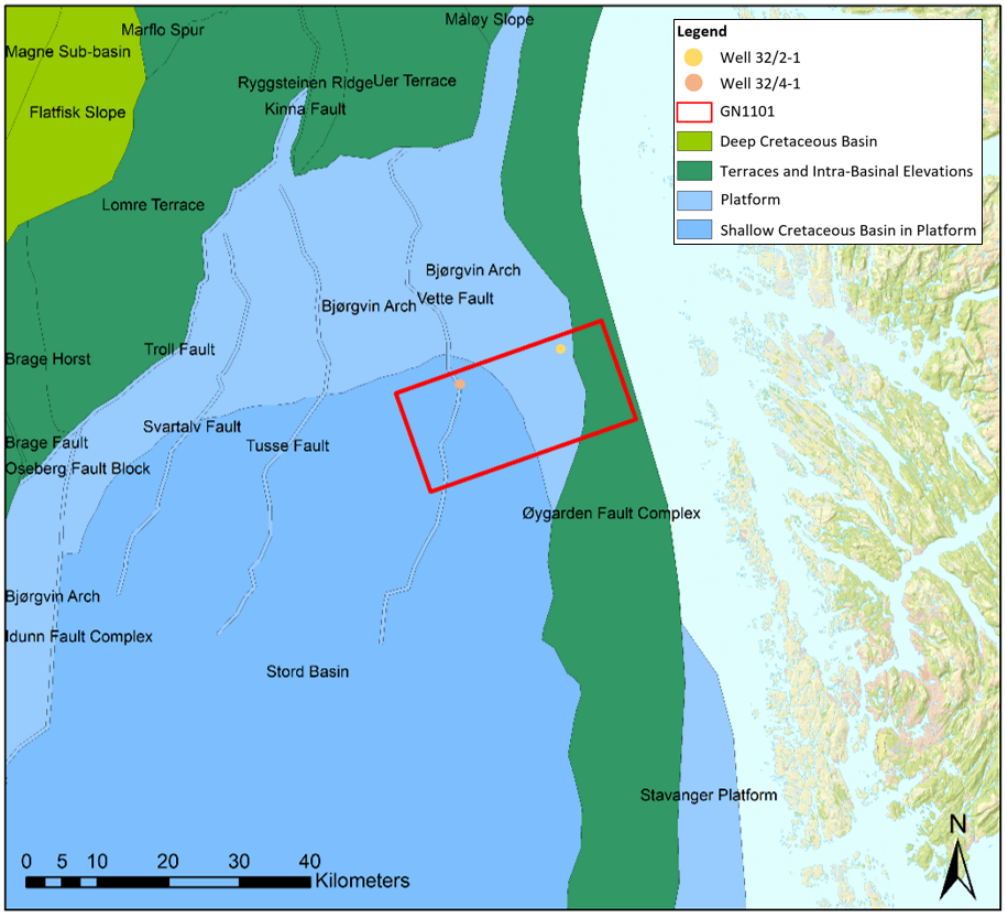

Figure 9: *Map view of the 3D seismic survey and wells used in this thesis. Base map and structural elements from NPD Factmaps (NPD, 2022).*

4.2 Methods

4.2.1 Seismic data

The 3D seismic survey GN1101 was converted from time to depth using the Petrel E&P Software Platform (Schlumberger). The depth conversion was performed to obtain a more "geological", realistic view of the structure without vertical exaggeration (Sofolabo et al., 2018), and to produce depth sections for the mechanical modelling. First, the interval velocities were extracted at the two wells (32/4-1 and 32/2-1) from the well top depths, and the surface times provided in the dataset. The well tops and surfaces of the top Draupne Fm, top Sognefjord Fm, and top Fensfjord Fm were used. Interpolation of the interval velocities was performed using the "moving average" algorithm. The interpolated interval velocities were then applied to two-way traveltime (TWT) thicknesses defined by neighboring seismic surfaces, and the depth converted thicknesses were stacked to get the surfaces in depth. It should be noted that there are some uncertainties associated with the depth converted seismic survey due to few wells in the area, and only surfaces from the uppermost horizons resulting in a larger depth error deeper in the seismic.

Two key seismic sections across the Beta structure were chosen for the kinematic and mechanical modelling (Figures 10 and 11). Both sections are perpendicular to the fold and show different fault-fold geometries. The interpretation of the two seismic sections was carried out using the provided horizons and surfaces in the dataset. The first section, Section 1, is a SW-NE section going across the well 32/2-1 (Figure 10). The ØFC displays a non-planar fault shape, with an upper listric fault segment, followed by a convex upwards fault segment, and a planar ~20° dip fault segment deep in the section (Figure 10). The hanging wall Triassic and Jurassic sediments, shown in purple and blue, are juxtaposed against basement in the footwall. The hanging wall Lower Cretaceous sediments are juxtaposed against sediments in the footwall. Based on interpretations by Mulrooney et al. (2020) and Wu et al. (2021), the sedimentary strata in the footwall is possibly of Jurassic age with no preservation of the Permo-Triassic succession, and has a gentle westward dip (Figure 10). The hanging wall Permo-Triassic to Lower-Cretaceous strata are folded as an anticlinal structure with crestal antithetic and synthetic normal faults. The Jurassic-Cretaceous strata show severe normal drag adjacent to the fault. Two hanging wall, Upper Jurassic and Lower Cretaceous growth packages are identified (GP2 and GP1 in Figure 8). The boundary between these packages (top Draupne Fm) is an unconformity, as evidenced by sediment onlaps and

truncations (Figure 8). The Base Nordland unconformity is also evident by onlaps, downlaps, and truncations (Figure 8). The ØFC does not offset or fold the Neogene strata above the Base Nordland Unconformity.

The second section, Section 2, is an E-W section on the southern end of the Beta structure (Figure 11). In this section, the fault seems to have a more irregular geometry, with more bends. The anticline is broader, and its crest is less faulted than in section 1. Interestingly, the Permo-Triassic to top Sognefjord strata display a hanging wall syncline near the fault, while the strata above the top Sognefjord and below the Norland unconformity display an anticline near the fault. The change from hanging wall syncline to hanging wall anticline coincides with a convex fault bend.

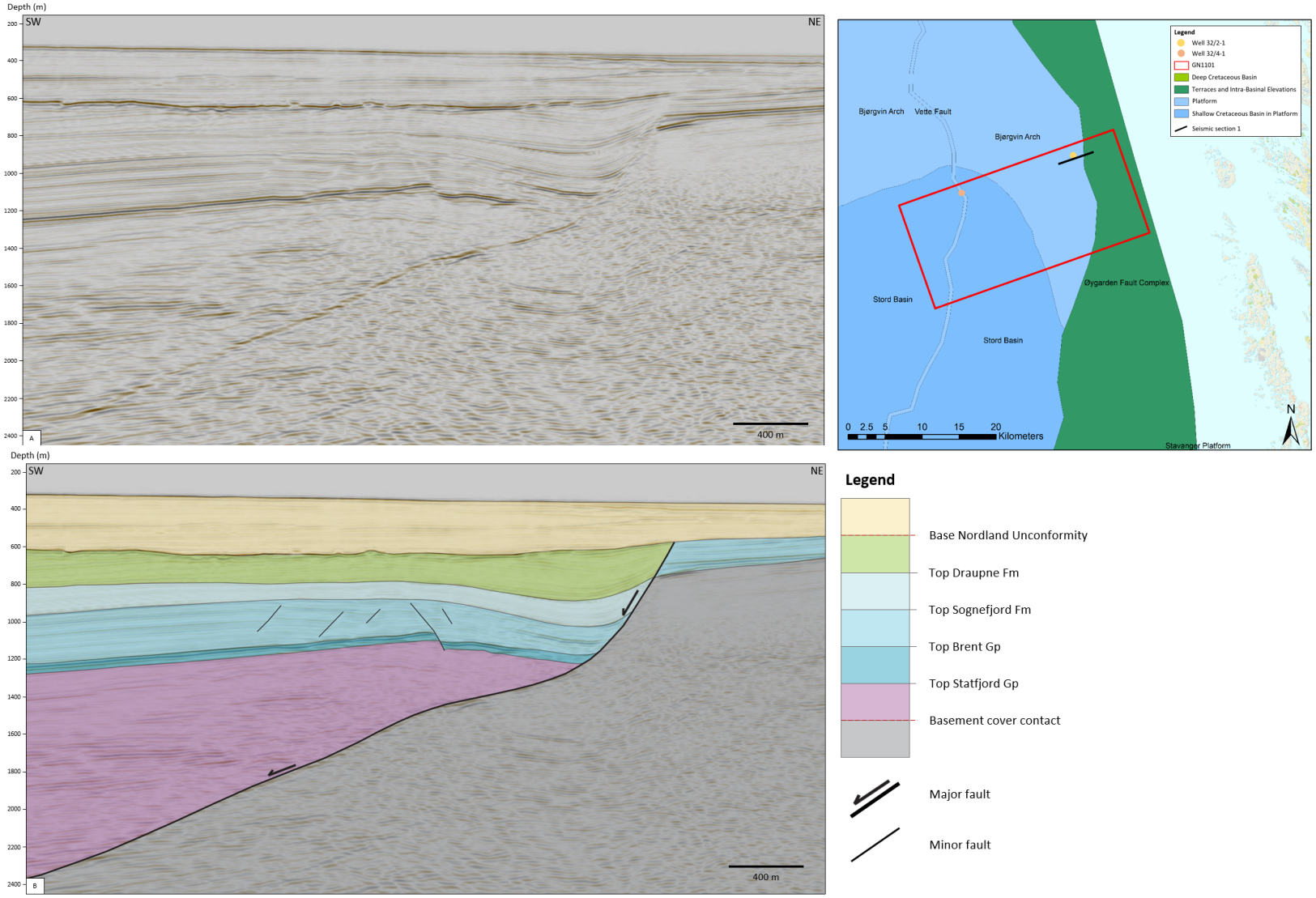

Figure 10: *(A): Seismic section 1 without interpretation. (B): Seismic section 1 with interpretation. Sections are presented without vertical exaggeration. Map shows the location of the section.*

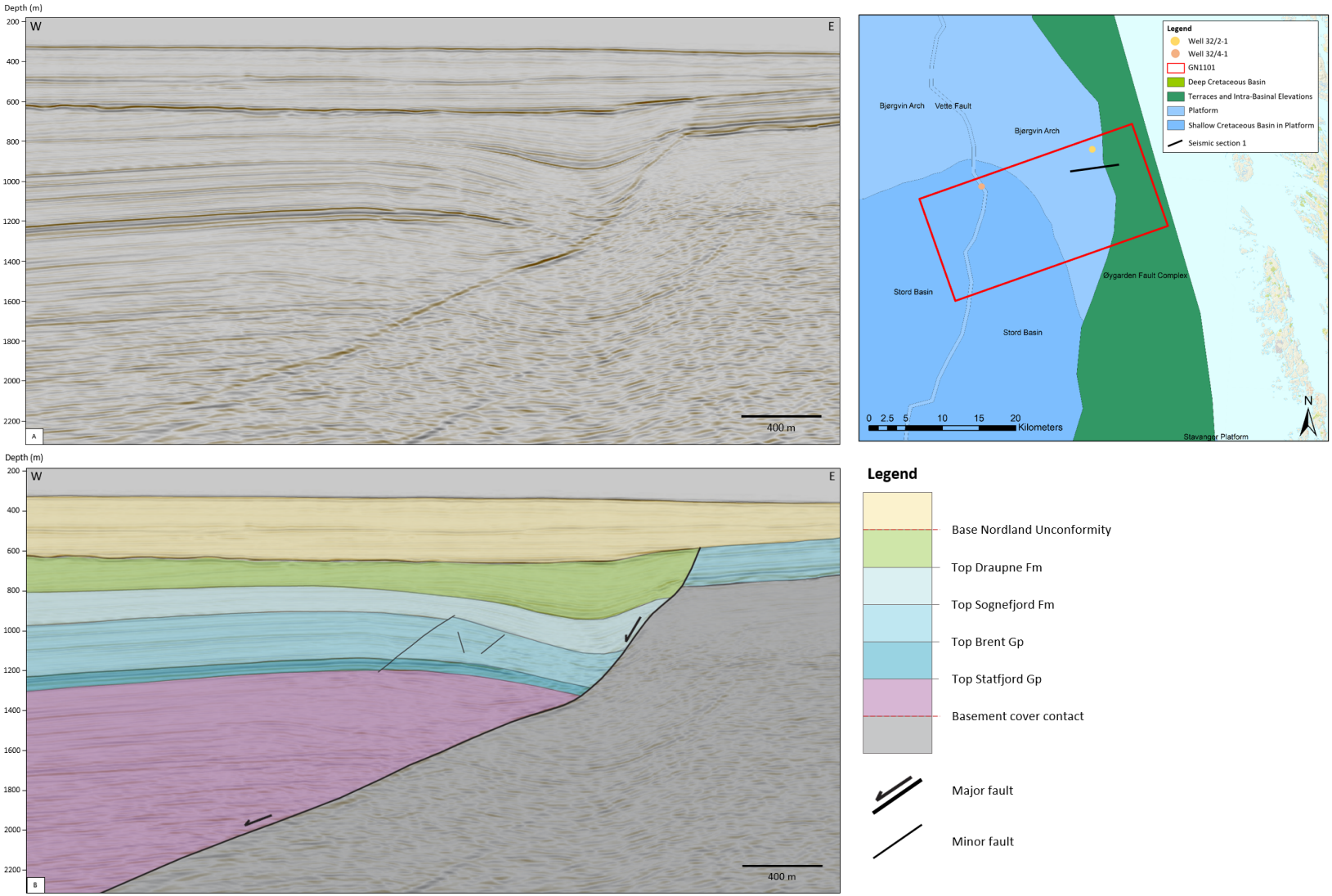

Figure 11: *(A) Seismic section 2 without interpretation. (B): Seismic section 2 with interpretation. No vertical exaggeration. Map shows location of the section.*

4.2.2 Kinematic modelling

Kinematic modelling of the sections 1 and 2 (Figures 10 and 11) was performed using the software StructureSolver. This program uses the fault bend fold method by Xiao and Suppe (1992), which treats the fault as if it were composed of several straight fault segments. At the junction of two of these segments, if the bend is concave upwards, antithetic shear is applied, while if the bend is convex upwards, synthetic shear is applied (Figure 2). The shape of the folds is controlled by several variables, including (1) the shape of the fault (this is by far the most critical input), (2) the total slip after each bed is deposited, (3) the direction of relative particle motion in the collapse of the hanging-wall (which is determined by the shear angle), (4) the sedimentation rate relative to the fault slip rate, and (5) compaction (Xiao & Suppe, 1992). Thus, the software allows modelling these variables, except compaction. As compaction changes the fault shape and the relationship between rollover and fault shape, excluding compaction gives some uncertainties. However, Xiao and Suppe (1992) argue that under common conditions compaction can be neglected if the folding is modeled in the compacted state.

The kinematic modelling of the Beta structure was performed to get a better understanding of how the fault geometry of the ØFC affects the fold structure. Sections 1 and 2 (Figures 10 and 11) were calibrated horizontally and vertically to fit their scales. The main horizons were digitized, and the ØFC was carefully interpreted. Structural surfaces that correspond with the horizons in the hanging-wall were added and linked to the interpreted ØFC, starting with a datum at the sea bottom. The software then automatically determines the shape of the structural surfaces in the hanging wall based on the geometry of the fault. As the interpreted fault includes a set of antithetic and synthetic shear planes that control the deformation within the hanging-wall, changing the fault geometry enables the structural surfaces to be modified to get the best-fit model.

4.2.3 Mechanical modelling

The discrete element method (DEM) can reproduce geologic structures by simulating the rock as an assembly of elements interacting with gravity and contact forces (Gray et al., 2014; Li et al., 2021). In this thesis, I use a 2D DEM modelling code written by Stuart Hardy, namely cdem2D. The use of this code for modelling geological structures is well documented by

Hardy (2019), and it has been applied to many problems including fault-propagation folding (Hardy & Finch, 2007), caldera collapse (Hardy, 2008), and salt flow (Hardy, 2018). In this thesis, I use a modified version of cdem2D that allows reading the fault geometry from a text file containing the *x* and *y* coordinates of the vertices of the fault. Once the fault is read and superimposed on the initial rectangular assembly, the program removes all the elements in the footwall, and leaves only the elements in the hanging wall (Figure 12). Thus, the simulations concentrate only on the hanging wall.

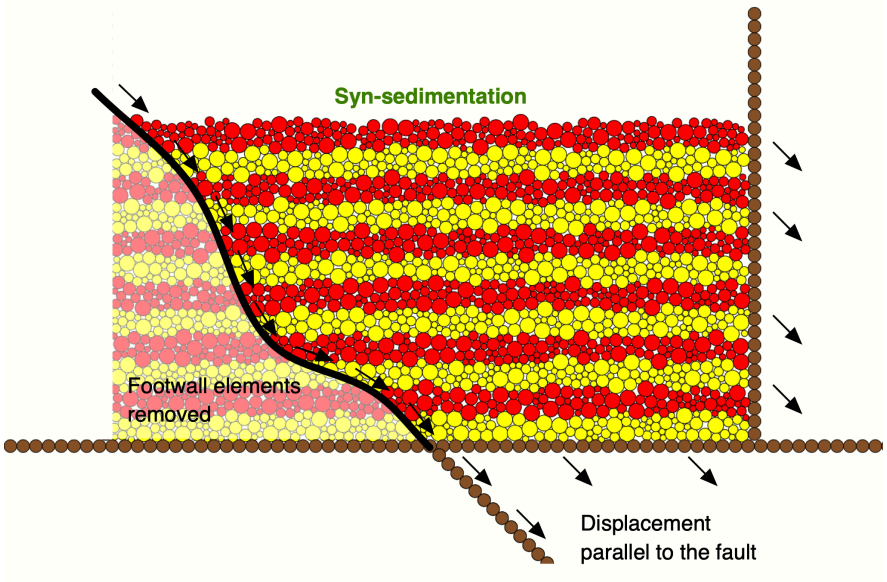

Figure 12: *Setup of the non-planar fault model where the footwall elements are removed.*

cdem2D is a C code that works as a command-based program. The input parameters to the simulation are defined in a runtime.txt file, the rectangular assembly is defined in a med.txt file, and the fault geometry is defined in a fault.txt file. Once these files are ready, the program can be run from a terminal window, using a specific set of commands. Throughout the run, the program outputs the increments of the simulations as they are completed. Each increment is a text file which is numbered sequentially (incr1.txt, incr2.txt, etc.). By the end of the simulation, all increments are in the folder where the program was executed. More details about cdem2D and input files are given in the Appendixes A-C.

Manipulating all the increments (text files) from a cdem2D run is rather difficult. Luckily, Cardozo and Hardy (submitted) have written a Macintosh program, cdem, that reads the increments from cdem2D, and can display the geometry, displacement, strain, and even stress (if output by cdem2D) of the simulation through time. Therefore, I use cdem for visualizing

and processing the results from cdem2D in terms of geometry, displacement, and strain. All the DEM figures in the thesis are made using cdem.

To create simulations equivalent to the two key seismic sections 1 and 2 (Figures 10 and 11), the geometry of the ØFC was digitized from the depth-converted seismic sections, and a text file (fault.txt) containing the vertices of the fault was produced. Then, the dimensions of the assembly were set up to fit the extent of the sections. The assembly at the start of the simulation represents the pre-growth Triassic to Middle Jurassic strata in the Beta structure, and as the simulation progresses there is syn-sedimentation. The growth strata represent the Upper Jurassic-Lower Cretaceous growth sequences below the Nordland unconformity. The models do not include the strata above the Nordland unconformity.

As explained before, parameters such as the number of elements in the simulation, the total run-time, and the element density, were defined in a separate runtime text file (a detailed description of this file is given in the Appendix A and B). The parameters that are pretty much constant in all simulations are listed in Table 1.

Parameters	Value
Number of initial elements	21,000
Element density (kg/m^3)	2,500
Element radii (m)	6.25-15.625
Elastic spring constant K (N/m)	5.54E+09
Damping viscosity v (N.s/m)	3.00E+07
Total run-time (s)	20,000
Time-step (s)	0.002
Contact friction	0.25
Contact cohesion force C0(N)	6.00E+07
Bulk friction	0.7
Bulk cohesion (MPa)	2.8
Assembly width (m)	5,000
Assembly height (m)	1,500

Table 1: *Model parameters that are mostly constant in all simulations. The last two rows of the table give the bulk assembly friction and cohesion.*

In the simulations, the assembly behaves as a frictional-cohesive material with an element-defined friction and cohesion force (Table 1; Hardy, 2019). However, an issue with the DEM is that the bulk properties of the assembly cannot be known a priori from the properties of the

elements. In other words, it is necessary to calibrate the element properties such that the bulk behaviour of the assembly is geologically realistic. The element properties as listed in Table 1 yield a bulk coefficient of friction of 0.7 and bulk cohesion of 2.8 MPa (Hardy & Cardozo, 2021), which are realistic values for rocks at the scale of modelling (5 x 1.5 km assembly size, Table 1). Therefore, I do not present any calibration of the assembly.

5 Results

5.1 Kinematic modelling

In this section, I discuss the results of modelling the two sections using kinematics and StructureSolver. It is important to remember that the model in StructureSolver is that of Figure 2, and therefore the most important parameters are the fault shape, which dictates the upwards concave or convex bends, and the shear angle. Overall, I found that the modelling in StructureSolver is very sensible to the geometry of the fault. Minor changes in the fault geometry induce significant changes in the modelled geometry of the horizons. The modelling is less sensible to the shear angle, though I modified the shear angle to obtain a better fit.

5.1.1 Section 1

Figure 13a shows the interpretation of section 1. The Øygarden fault is interpreted in red, and the interpreted horizons are the tops of the Statfjord Gp., Brent Gp., Sognefjord Fm., and Draupne Fm. The Nordland unconformity is also included. From the interpretation we can see that the sequence below the top Sognefjord is pre-growth, and the sequence above the top Sognefjord and below the Nordland unconformity is syn-growth. It is important to mention that the interpreted fault geometry in Figure 13a is the one that gave the best fit to the interpreted tops, after many iterations with different fault geometries. The modelling strategy was trying to fit the lowermost Statfjord and Brent tops, and then use the kinematic model for these lower tops to fit the two tops above.

Figure 13b shows the best model I could make after many (100s) of iterations. The modelled ØFC has a listric shape with a large concave upwards bend at ~1400 m depth, a convex upwards bend at ~1600 m, and a straight ~20° dip geometry below this bend (Figure 13b). The model was made with a shear angle of 59°. The yellow lines are the modelled beds. The fit to the lowermost Statfjord and Brent tops is reasonable, though the forelimb of the anticline is steeper than the interpreted beds, and the local hanging wall syncline close to the fault is not replicated. The model fit to the Sognefjord and Draupne tops is not good, particularly close to the fault, where the model can't replicate the observed hanging wall syncline but rather it shows a steep anticlinal forelimb. In addition, the Sognefjord and Draupne tops in the footwall are too high in relation to the Statfjord and Brent tops in the same block, giving an unrealistic (and incorrect) high thickness of the Sognefjord Fm. in the footwall. This model therefore has problems. However, it is interesting to see the estimated

displacement of the horizons which is 842 m for the tops Statfjord and Brent, 884 m for the top Sognefjord (clearly wrong), and 752 m for the top Draupne. In addition, in terms of sediment growth, the model estimates the following expansion indexes (expansion index = unit thickness in hanging wall/unit thickness footwall): 0.95 for the Sognefjord Fm, 1.70 for the Draupne Fm., and 1.70 for the Cromer Knoll Gp. Thus, the Draupne Fm and Cromer Knoll Gp have a thicker stratigraphic sequence in the hanging-wall than in the footwall, indicating fault movement during the sedimentation of these sequences.

5.1.2 Section 2

The interpretation of section 2 is shown in Figure 14a, with the same interpreted horizons and major fault as in Figure 13a. Like in section 1, the interpreted fault geometry is the one that gave the best fit with the lowermost Statfjord and Brent tops after trying many different fault geometries. The kinematic model for these lower tops were then used to fit the other two tops above.

Figure 14b shows the best-fit model for section 2. Like section 1, the modelled fault of section 2 has a listric shape with a straight ~20° dip geometry below 1500 m depth. However, in this section the modelled ØFC yields a better fit by adding more fault bends. The ØFC has a small concave upwards bend at ~800 m depth followed by a small convex upwards bend at ~1000 m depth. At ~1300 m depth, there is a larger concave upwards bend followed by a small convex upwards bend at ~1400 m (Figure 14b). In this model, a shear angle of 67° was used.

The model fit to the Statfjord and Brent horizons is reasonably good across most of the structure in the hanging wall, although the modelled forelimb of the anticline is steeper than the interpreted horizons. Compared to section 1, the model for section 2 does a better job at replicating the local hanging wall syncline close to the fault. The fit to the top Sognefjord in the hanging wall is very satisfactory as it replicates the local hanging wall syncline and has a reasonable fit to the rest of the anticline. The model fit to the top Draupne is not as good as it doesn't replicate the steep eastern limb of the hanging-wall syncline. The fit in the backlimb away from the fault is also worse than the other horizons, as the modelled horizon is deeper than the interpreted one. As for the tops Sognefjord and Draupne in the footwall, they are located further down, giving a more realistic thickness of the the Sognefjord Fm than in section 1. For section 2, the estimated displacement of the horizons is as follows: 759 m for the tops Statfjord and Brent, 580 m for the top Sognefjord, and 492 m for the top Draupne.

The model estimates an expansion index of 0.9 for the Sognefjord Fm, 1.28 for the Draupne Fm, and 1.24 for the Cromer Knoll Gp. This again corroborates that the Draupne Fm. and the Cromer Knoll Gp. are growth strata.

5.1.3 Conclusion

Overall, inclined shear does a reasonable job in replicating the Beta structure. However, there are significant problems in section 1, and less problems in section 2. Most of these problems are around the hanging wall syncline close to the fault. Section 1 suggests a ØFC displacement of ~850 m, while section 2 suggest a displacement of ~750 m. Both sections clearly indicate that the Draupne Fm and Cormer Knoll Gp. are growth strata, and their expansion indexes most likely are ~ 1.25, as suggested by section 2. Expansion indexes for section 1 are unreliable since the modelled footwall stratigraphy in this section is not reasonable.

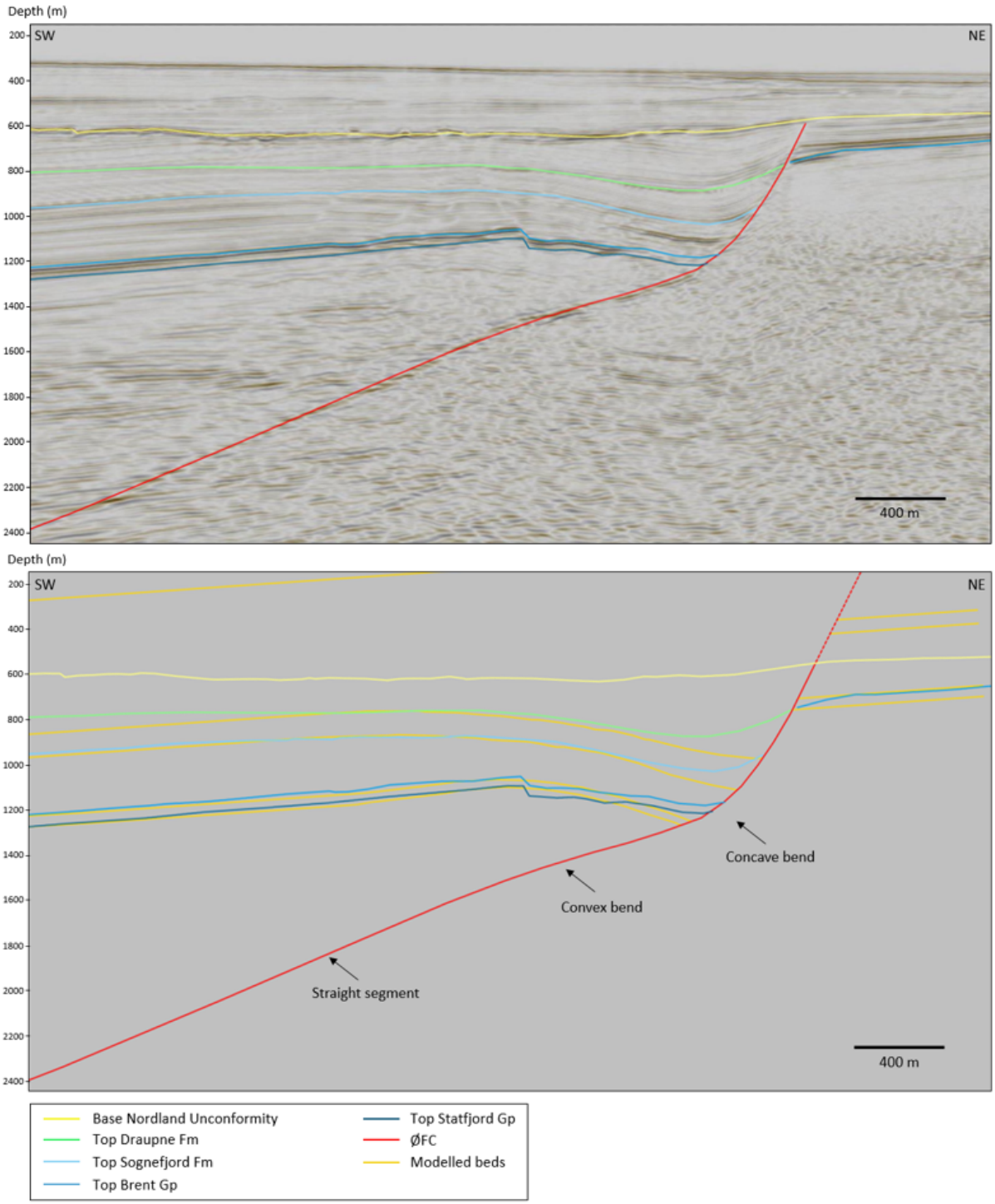

Figure 13: *The upper figure (a) displays section 1 with interpreted horizons. The lower figure (b) displays the best modelling results.*

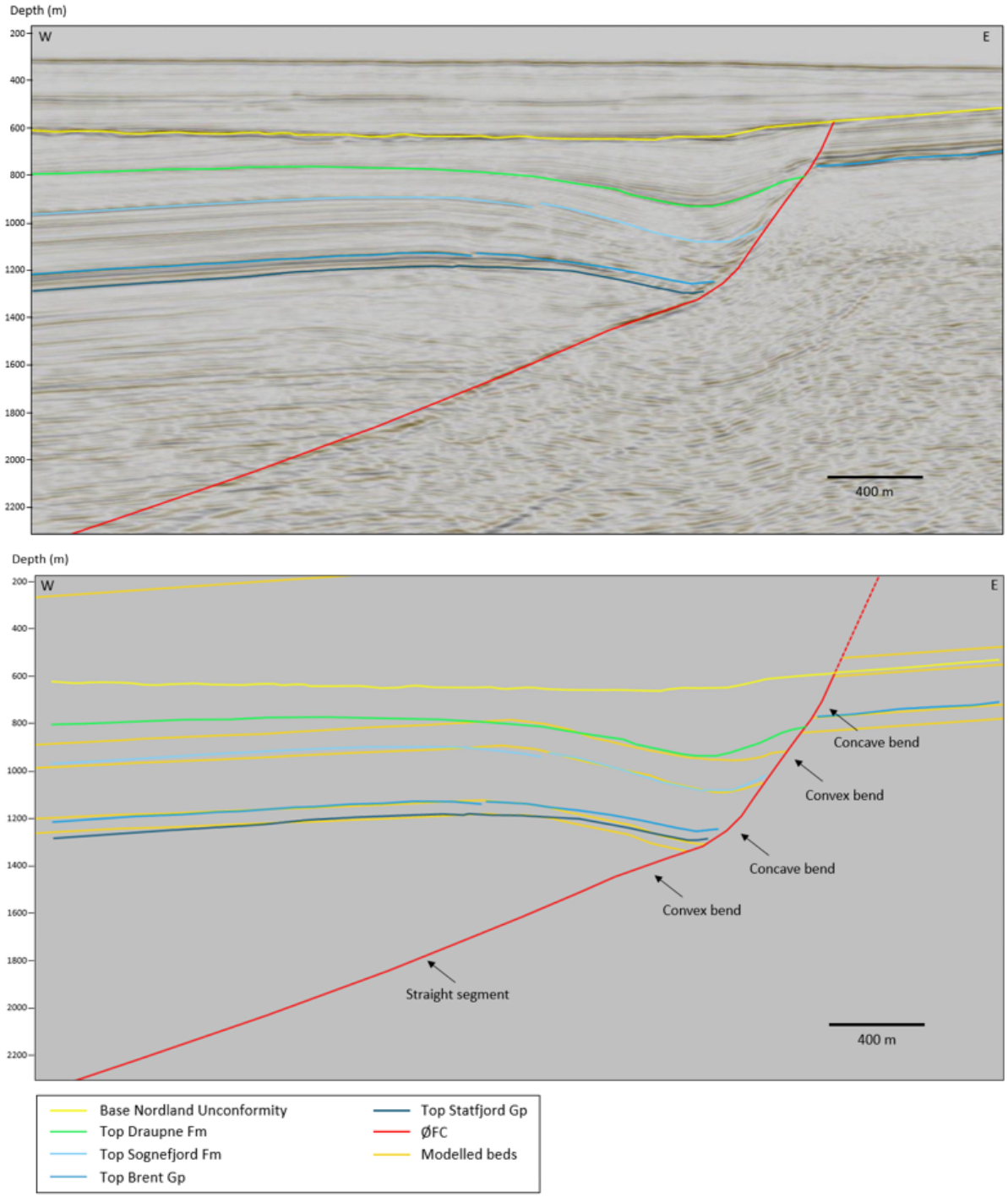

Figure 14: *The upper figure (a) displays section 2 with interpreted horizons. The lower figure (b) displays the best modelling results.*

5.2 Mechanical modelling

In this section, the results of the DEM mechanical modelling are described. As stated previously, the initial thickness of the assembly in the DEM model is ~1.5 km. This thickness was estimated through trial and error, attempting to match the final depth of the top of the pre-growth in the model with the depth of the top of the pre-growth (top Sognefjord) in the seismic section. After trying different thicknesses and runs, an initial thickness of the assembly of 12.5 model units (1.562 km for a unit scaling of 125 m) gave a reasonable match. This initial thickness is also consistent with the top of the pre-growth in the footwall predicted by kinematic modelling (Figure 15), although as discussed before, the kinematic model for section 1 has problems in the footwall area.

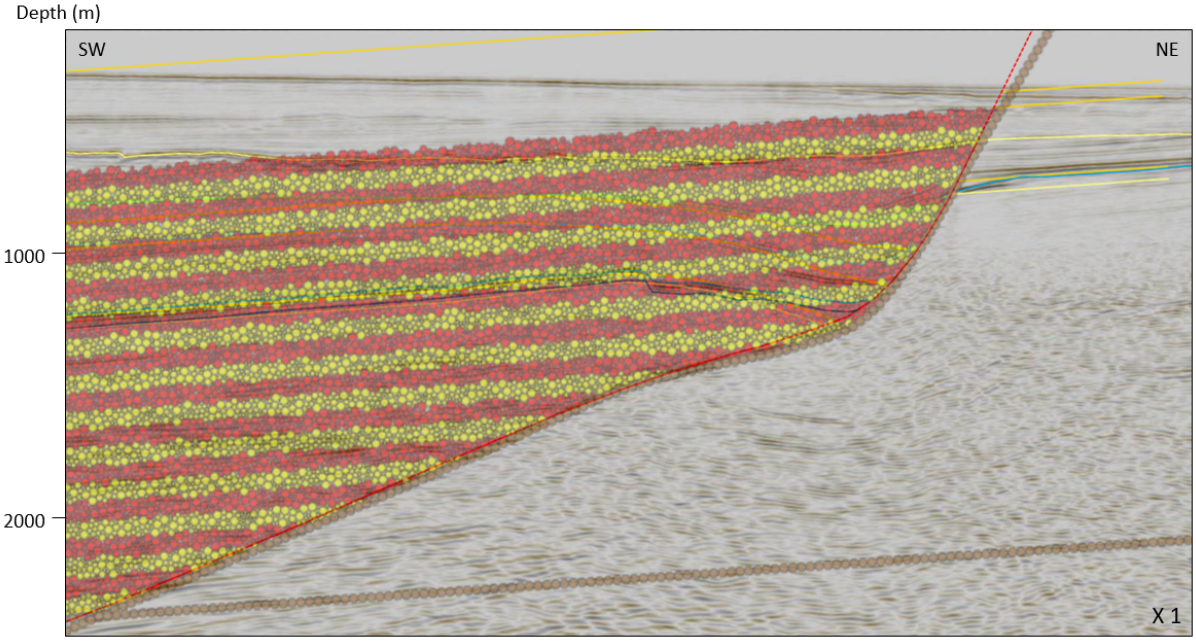

Figure 15: *Initial geometry of the assembly superimposed on the kinematic model for section 1 (Figure 13). The top of the assembly is consistent with the top of the pre-growth in the kinematic model.*

Total displacement in all DEM models (except the inversion model) is ~1 km. This is higher than the total displacement suggested by the kinematic modelling, which is ~850 m for section 1 and ~750 m for section 2. The final geometry of the simulations was superimposed to the seismic sections in order to compare the models to the Beta structure (e.g., Figure 16). In the models, the pre-growth strata are coloured in layers of red and yellow, while the growth strata are divided into two growth packages which represent the GP1 (green and pink layers in the models) and GP2 (orange and blue layers in the models) growth packages in the section.

In the seismic section, the blue line represents the top of the pre-growth (top Sognefjord), the dashed purple line represents the top GP1/base GP2, the black line represents the base Nordland unconformity, and the red dashed line represents the ØFC.

To get insight about the models' evolution, the results of the simulations are also shown at 33%, 66% and 100% total displacement, and they include the geometry of the model, the total vertical displacement u_y (positive is upward and negative is downward displacement), and the total maximum shear strain γ_{max} (e.g., Figure 17). As the simulations were analysed, the models that gave the best fit to the seismic sections were further used in other simulations, where changes were introduced to try to obtain a better fit. The input for all the simulations can be found in Table 2.

	Section	Total run time (s)	Base level rise (m/timestep)	Coeff. friction	Base coeff. friction	Wall coeff. friction	Fault coeff. Friction	C0 (N)	Mylar sheet	Flexural slip	Inversion start
Model A	1	20000		0.25	0.25	0.25	0.25	60000000	yes		
Model B	1	20000		0.25	0.25	0.25	0	60000000	no		
Model C	1	20000		0.125	0.125	0.125	0.125	30000000	yes		
Model D	1	20000		0.25	0.25	0.25	0.25	60000000	yes	yes	
Model E	1	20000	0.00001	0.125	0.125	0.125	0.125	30000000	yes		
Model F	1	20000	0.00001	0.25	0.25	0.25	0.25	60000000	yes	yes	
Model G	1	20000	0.00004	0.125	0.125	0.125	0.125	30000000	yes		
Model H	1	20000	0.00004	0.25	0.25	0.25	0.25	60000000	yes	yes	
Model I	2	20000		0.25	0.25	0.25	0.25	60000000	yes		
Model J	2	20000		0.125	0.125	0.125	0.125	30000000	yes		
Model K	2	20000		0.25	0.25	0.25	0.25	60000000	yes	yes	
Model L	2	20000	0.00001	0.125	0.125	0.125	0.125	30000000	yes		
Model M	2	20000	0.00001	0.25	0.25	0.25	0.25	60000000	yes	yes	
Model N	2	20000	0.00004	0.125	0.125	0.125	0.125	30000000	yes		
Model O	2	20000	0.00004	0.25	0.25	0.25	0.25	60000000	yes	yes	
Model P	1	25000		0.25	0.25	0.25	0.25	60000000	yes	yes	0.75
Model Q	2	25000		0.25	0.25	0.25	0.25	60000000	yes	yes	0.75

Table 2: *Key parameters in the DEM simulations.*

5.2.1 Section 1

Model A (default model)

Model A is the default simulation for section 1, where elements above the ØFC are under constant displacement (CD), and they are displaced parallel to the fault, like sandbox models where a mylar sheet moves along the fault and drag the material above it (McClay & Scott, 1991). The contact friction between the elements, and between the elements and the base, lateral and fault walls is 0.25, and the cohesive force between the elements is 6e7 N. The growth strata are as strong as the pre-growth strata, and the base level is static, and it represents the uppermost surface of the growth strata (Table 2).

Figure 16 shows the final geometry of the default model superimposed on seismic section 1. A hanging wall anticline is formed, with normal faults offsetting the forelimb of the structure, and a reverse fault offsetting the backlimb of the structure. On the backlimb of the anticline, the top of the pre-growth in the model fits reasonably well with the top of the pre-growth (top Sognefjord) in the seismic section, although it is a bit lower which also makes the growth strata to be too low as well. The crest of the modelled fold is however too high. There is also significant mismatch near the ØFC as the model fails to simulate the hanging wall syncline. The modelled forelimb in the pre-growth sequence is too deep and steep in comparison to the actual section.

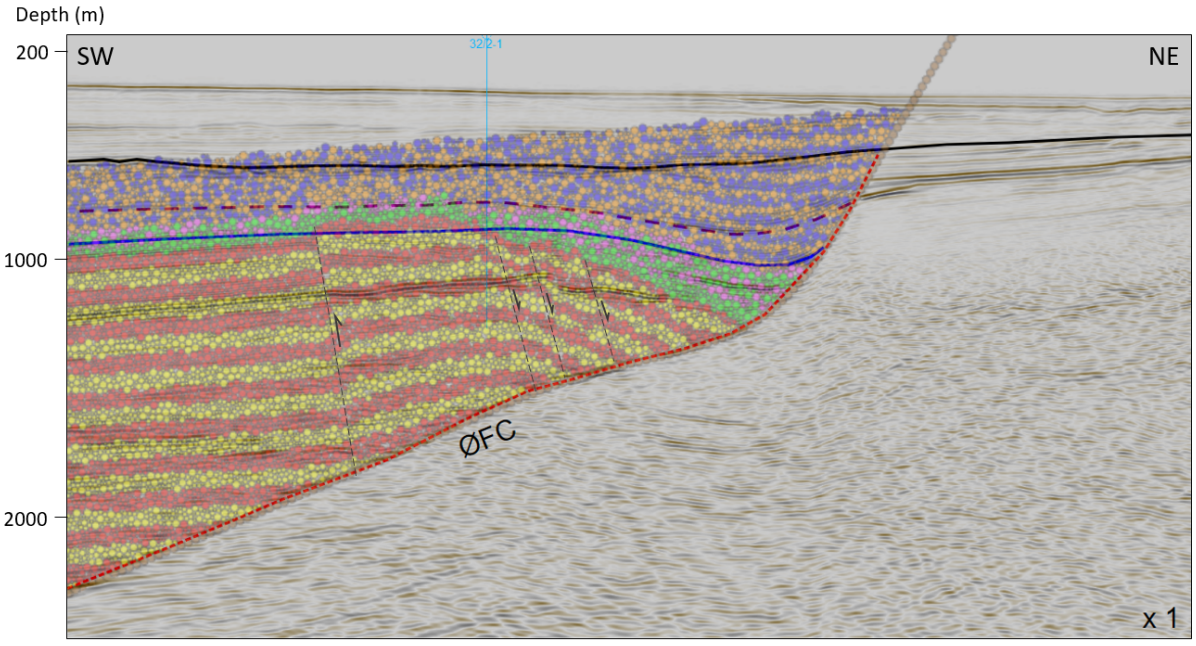

Figure 16: *Final geometry of model A, default model, compared with seismic section 1. Blue line is top pre-growth (top Sognefjord), dashed purple line is top GP1, and black line is base Norland unconformity on seismic section.*

The evolution of the structure is shown in Figure 17. At 33% total displacement (Figure 17a), a syncline is formed above the concave upwards fault bend, and an anticline is formed above the convex upwards fault bend below. The forelimb of the structure has collapsed along antithetic normal faults, which are highlighted by γ_{max}. A triangular area near the uppermost, steepest segment of the ØFC shows the maximum downward displacement (lowest u_y). At 66% total displacement (Figure 17b), a syncline has formed close to the ØFC both in the pre-growth and growth strata. The collapse of the forelimb area of the anticline is more intense as displayed by γ_{max}, and the area of maximum downward displacement (lowest u_y) has expanded downwards. At this stage, it is also clear that there is a reverse fault in the backlimb of the anticline, which is focused on the convex upwards fault bend. This area displays upward vertical displacement (highest u_y) relative to adjacent areas. At 100% total displacement (Figure 17c), the hanging wall syncline in the pre-growth sequence has almost disappeared, as the elements have been dragged over the low-angle segment of the fault, and the forelimb has become steep. More normal fault collapse occurs in the forelimb of the anticline as evidenced by γ_{max}, and the maximum downward displacement (lowest u_y) is at the concave upwards fault bend. Finally, the reverse fault on the backlimb of the anticline has been translated downwards towards the planar segment of the fault, without further deformation in this area. Thickening of growth strata towards the ØFC can be seen in both growth packages GP1 and GP2 (Figures 17a-c), but especially in GP2 towards the end of the structure's evolution (Figure 17c).

From this evolution it is clear that:

- The syncline is related to the concave upwards fault bend, while the anticline is related to the convex upwards fault bend below.
- The syncline forms in the early to intermediate stages of the structure's evolution, while the elements are dragged along the uppermost planar and concave segments of the fault. However, this structure is destroyed in a later stage, when the elements are dragged along the low angle segment of the fault below.
- Reverse faulting in the backlimb is associated with movement of the elements over the convex upwards fault bend. Once the backlimb passes this bend, the reverse fault is just translated, without further deformation.
- Collapse of the anticlinal forelimb along antithetic normal faults occurs over the entire structure´s evolution.

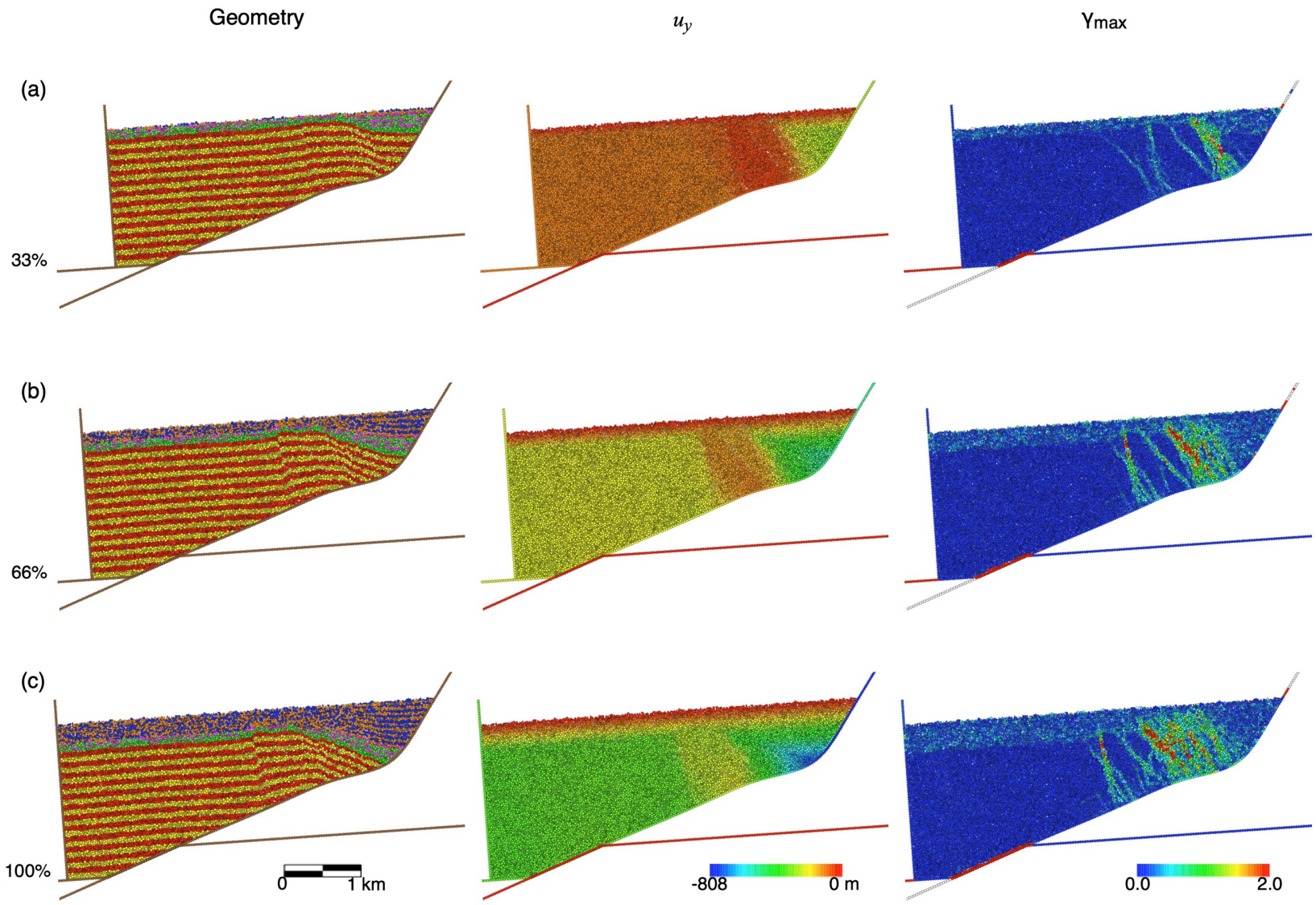

Figure 17: *Results of model A, default model, at (a) 33%, (b) 66% and (c) 100% total displacement. The geometry is shown on the left, total vertical displacement in the middle, and total maximum shear strain on the right.*

Model B (Constant heave)

In the second model, model B, the elements above the ØFC are under constant heave (CH). In this case, normal fault movement is simulated by displacing the fault elements horizontally and the hanging-wall elements vertically in order to match the displacement along the lowermost fault segment (arrows in Figure 18) (Cardozo & Hardy, submited). As in model A, the contact friction between the elements, and between the elements and the base, lateral and fault walls is 0.25, and the cohesive force between the elements is 6e7 N. The growth strata are as strong as the pre-growth strata, and the base level is held static (Table 2).

Figure 18 shows the final geometry of model B superimposed on seismic section 1. A deep graben has formed in the hanging wall above the convex upwards and lower planar segments of the fault. Both the pre-growth and growth strata have collapsed along synthetic and antithetic normal faults, which propagated from the convex upwards fault bend. The layers on both sides of the graben are close to their regional, and there is barely any relative displacement of the elements close to the uppermost planar segment of the fault. Therefore, very little growth strata were deposited above these elements, and most were deposited within the graben and above the SW pre-growth strata further away from the fault. This model does not fit at all the Beta structure. Therefore, constant heave is disregarded and not used in further simulations.

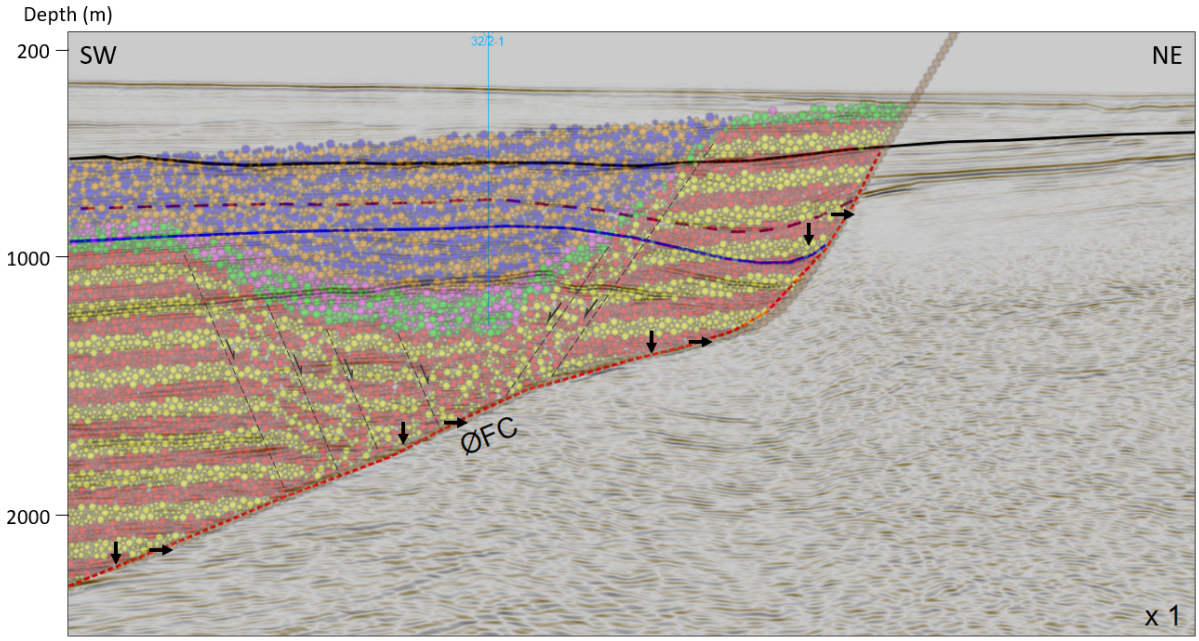

Figure 18: *Model B, constant heave, compared with seismic section 1. Arrows show the displacement of the hanging wall and fault elements to simulate normal movement along the ØFC.*

Model C (Half friction and cohesion)

Since applying constant displacement to the elements above the ØFC gave much better results than constant heave, model A (constant displacement) was used as the base for the other models in section 1. In model C, the contact friction between the elements, and between the elements and the base, lateral and fault walls is reduced from 0.25 to 0.125, and the cohesive force is also reduced from 6e7 N to 3e7 N (Table 2). This model has therefore half the strength of model A.

Figure 19 shows the final geometry of model C superimposed on seismic section 1. As in model A, an anticline is formed in the hanging wall. The forelimb of the structure is offset by normal faults, and the backlimb by a reverse fault. However, compared to model A, the amount of offset of the normal and reverse faults in model C is smaller, which results in the crest of the anticline to be lower, giving a better fit to the top of the pre-growth (top Sognefjord) in this area. The fit to the top pre-growth in the backlimb is as good as in model A, but the model also fails to simulate the hanging wall syncline close to the ØFC. The modelled forelimb in the pre-growth sequence is even steeper than in model A, but the top of the modelled GP1 has a much better fit along the backlimb and crest of the fold.

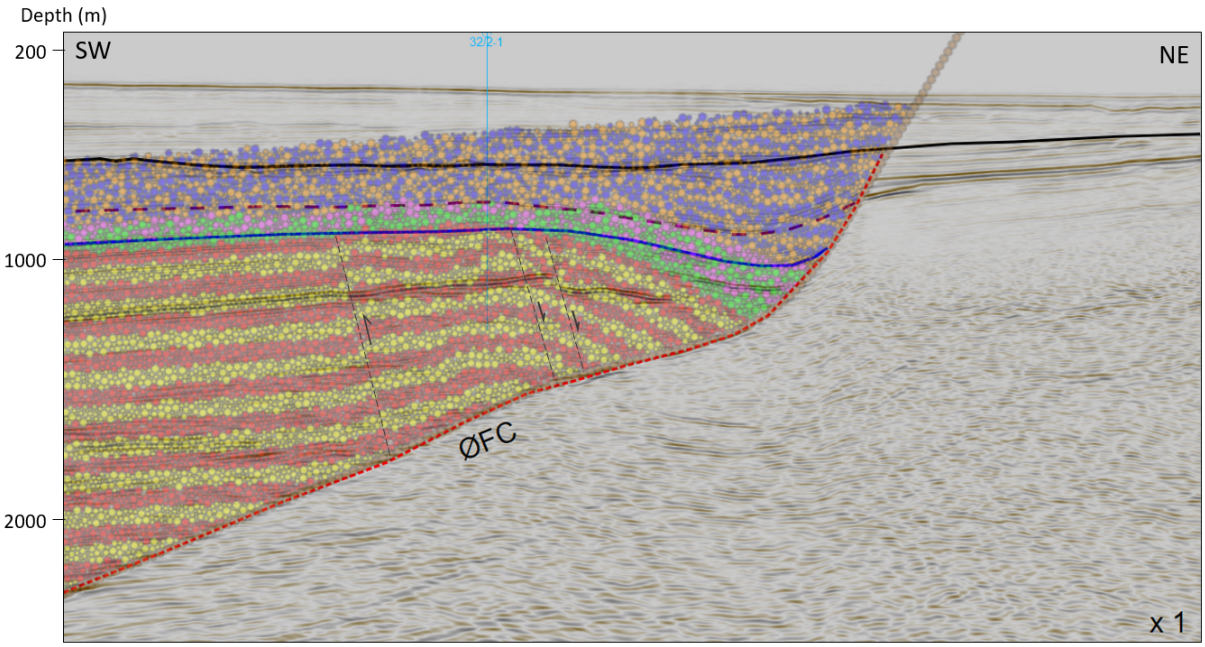

Figure 19: *Final geometry of model C superimposed on seismic section 1.*

Figure 20 shows the evolution of the structure. At 33% total displacement (Figure 20a), models A and C are similar, with a syncline above the concave upwards fault bend, and an anticline above the convex upwards fault bend. Like in model A, antithetic normal faults develop from the concave upwards bend, but in this case, there is also a lower dip antithetic normal fault propagating from the concave upwards bend. This is well illustrated by γ_{max} (Figure 20a). A triangular area of downward displacement (lowest u_y) develops near the uppermost segment of the ØFC, but due to the lower dip antithetic normal fault, this area is wider than in model A. At 66% total displacement (Figure 20b), a syncline is formed in both the pre-growth and growth strata close to the ØFC. A reverse fault in the backlimb of the anticline is clear at this stage (Figure 20b, γ_{max} and u_y), but in comparison to model A, the amount of uplift on this fault is smaller. The crest of the anticline is therefore lower. This is clear by lower values of u_y (more downward displacement) in the crestal area. At 100% total displacement (Figure 20c), the hanging wall syncline has disappeared, and the forelimb is even steeper than in model A. Thickening of the growth strata (GP1 and GP2) towards the ØFC can be observed throughout the entire evolution of the structure (Figure 20a-c).

From the evolution of model C, it is clear that:

- Models A and C are similar.
- A lower element friction and cohesive force results in less brittle, more distributed deformation, with less offset of normal faults in the forelimb and the reverse fault in the backlimb of the structure. This results in a lower crest of the fold.
- A lower angle antithetic normal fault develops in the forelimb. This fault also contributes to less uplift of the crest of the anticline.
- Though the fit in the backlimb and crest of the structure is good, the fit to the local syncline is not good and the modelled forelimb is even steeper than in model A.

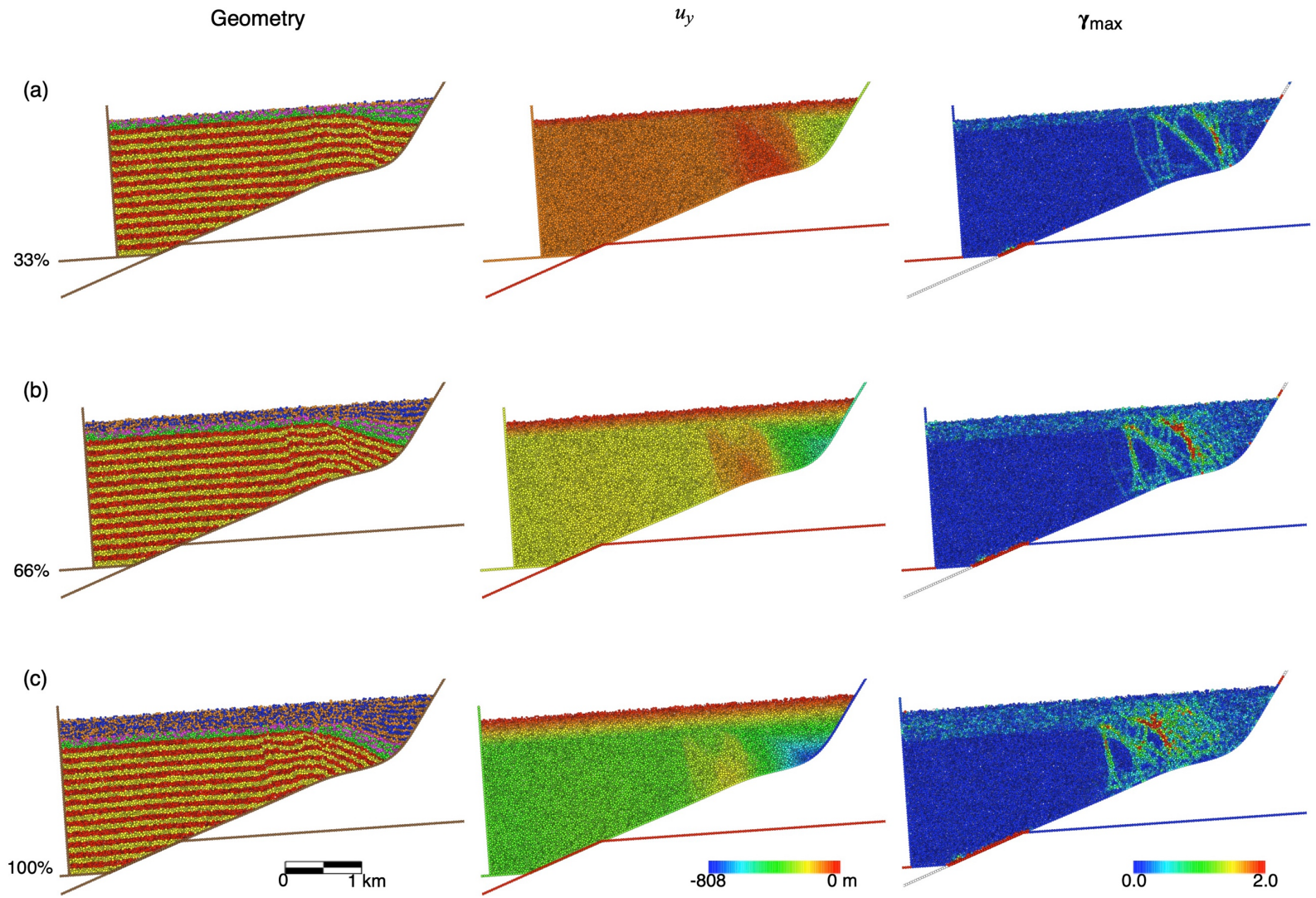

Figure 20: *Results of model C at (a) 33%, (b) 66% and (c) 100% total displacement. The geometry is shown on the left, total vertical displacement in the middle, and total maximum shear strain on the right.*

Model D (Flexural slip)

For model D, the parameters of model A were also used, but in this case flexural slip was included (Table 2). Flexural slip adds anisotropy to the assembly by making the layer contacts frictionless, thus favouring layer-parallel slip (Cardozo & Hardy, submitted). Adding flexural slip can help better approximate the typically anisotropic mechanical stratigraphy of sedimentary cover rocks, such as layered sandstone-shale sequences (Hardy, 2019).

Figure 21 shows the final geometry of model D superimposed on seismic section 1. The final geometry has many similarities to model A, where an anticline forms in the hanging wall. However, in this model, there is no prominent reverse fault offsetting the backlimb of the anticline, but rather synthetic normal faults. Normal faults in the forelimb of the structure can be seen with a greater offset than in models A and C. The crest of the fold is slightly tilted towards the SW, and does not fit the top of the pre-growth in the seismic section as well as model C. It does however give a better fit than model A. The backlimb and forelimb of the anticline have a similar fit to the pre-growth as in models A and C. The growth strata also have a similar geometry to models A and C.

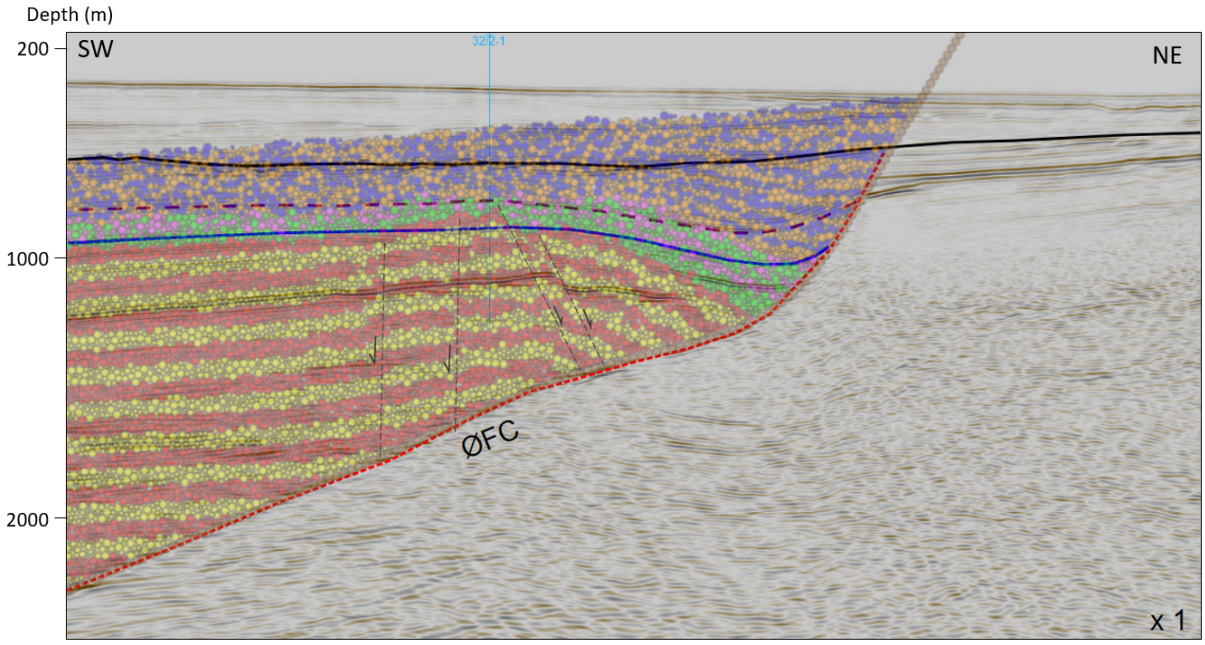

Figure 21: *Final geometry of model D compared with seismic section 1.*

Figure 22 shows the evolution of the structure. At 33% total displacement (Figure 22a), the model looks very similar to model C (Figure 20a). However, the antithetic normal faults

displacing the forelimb are more localized, and the low angle antithetic normal fault is less developed than in model C (γ_{max}, Figure 22a). At 66 % total displacement (Figure 22b), a syncline is formed close to the ØFC, as in the other models, and the collapse of the forelimb as well as the backlimb is more intense (γ_{max}). At this stage, strain localisation is lower than in models A and C, and the dip of the faults vary much more in this model. The crest of the fold, which is offset by normal faults, is slightly tilted towards the SW, and in the area of uplift (high u_y) above the convex fault bend, a synthetic normal fault rather than an antithetic reverse fault has developed. At 100% total displacement (Figure 22c), the hanging wall syncline in the pre-growth sequence has disappeared and the forelimb has become steeper. The crest of the fold and the backlimb of the anticline have been translated downwards, and a new synthetic normal fault has formed in the backlimb closer to the crest. As in the other models, the growth strata thicken towards the ØFC.

From this evolution it is clear that:

- Model D is similar to models A and C.
- The crest of the fold is slightly tilted towards the SW as the structure moves across the convex upwards bend. Rather than a reverse fault, synthetic normal faults develop in the backlimb area.
- Strain localisation is lower (deformation is more distributed) than in models A and C.
- This model fits better seismic section 1 than model A, but since the top of the pre-growth at the crest of the fold is tilted to the SW, it has a slightly worse fit than model C.

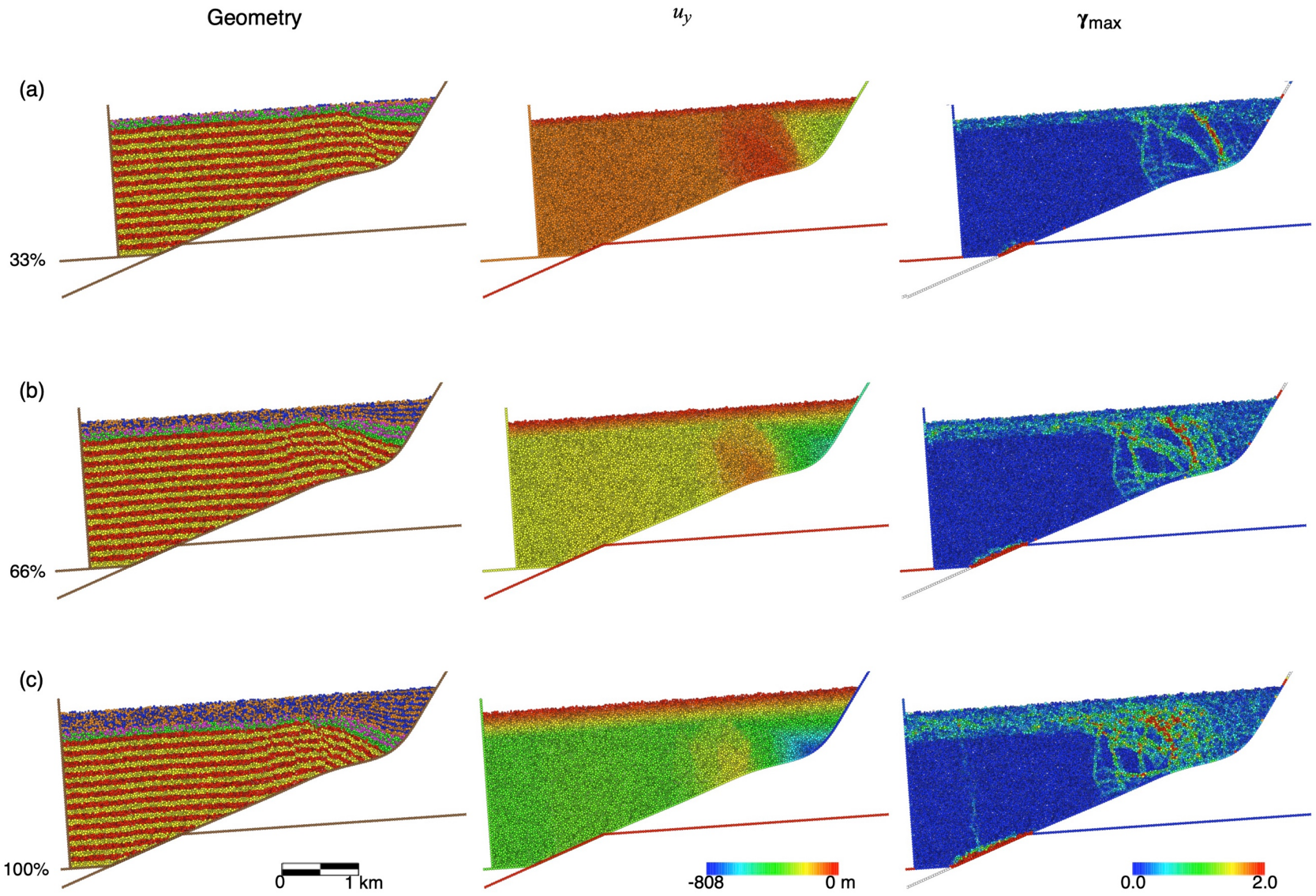

Figure 22: *Results of model D at (a) 33%, (b) 66% and (c) 100% of total displacement. The geometry is shown on the left, total vertical displacement in the middle, and total maximum shear strain on the right*

Models E, F, G and H

Models C and D have a better fit with seismic section 1 than models A and B. However, they still have some problems, especially replicating the local hanging wall syncline near the ØFC. The next models test the influence of sediment growth on Models C and D. Models E and G add more growth to model C, while models F and H add more growth to model D. For these four models, more growth was simulated by rising sea level throughout the simulation, instead of being static like in previous models. Models E and F have a moderate base level rise of 1e-5 m/timestep, while models G and H have a strong base level rise of 4e-5 m/timestep (Table 2).

Figure 23a-d shows the final geometry of the four models superimposed on seismic section 1. In all four models, a hanging wall anticline is formed like in previous models (except model B), but with slightly different geometries. Model E is similar to model C. However, a small anticline near the crest of the fold is formed between an antithetic and a synthetic normal fault (Figure 23a). At first (33% total displacement), antithetic normal faults form above the concave upwards bend of the ØFC and offset the forelimb of the structure. With more displacement (66% total displacement), a synthetic normal fault develops in the backlimb, and the antithetic and synthetic normal faults create a small horst at the crest of the fold. This horst is not seen in the actual section, and therefore, the top of the pre-growth strata in model E has a worse fit to the section than model C. Model E also fails to replicate the local syncline in the hanging wall near the ØFC, like previous models.

Model F has a different fold geometry than model D, especially near the crest and forelimb of the fold (Figure 23b). In this model, two anticlines (marked with upwards triangles in the figure) form near the crest of the fold, with a small graben in the middle (downward triangle). As in model D, antithetic normal faults displace the forelimb of the structure and a synthetic normal fault displaces the backlimb of the structure. In this model, a second antithetic normal fault develops breaching the crest of the fold, and as displacement increases (66% total displacement), a synthetic normal fault develops offsetting the antithetic fault. This results in a small graben (downward triangle in the figure) with two small anticlines (upward triangles) on each side (Figure 23b). The faulting also affects the growth strata. The modelled top of GP1 is, however, fairly reasonable in the backlimb and crest of the fold structure. As in the

other models, the local syncline near the ØFC is not replicated in this model. Overall, this model gives a worse fit to the seismic section than model D.

Model G has more growth than model E. This model is similar to model C, but the growth strata are much thicker in GP1 above the backlimb of the fold (Figure 23c). GP1 is also slightly thicker towards the ØFC. The thickness of GP1 in this model fits the GP1 in the seismic section, but the model also fails to replicate the hanging wall syncline close to the ØFC.

Model H has more growth than model F. This model is similar to model D, but the antithetic normal faults offsetting the forelimb of the fold shows less displacement (Figure 23d). The synthetic normal fault in the backlimb of the fold has approximately the same offset as in model D and F. The crest of the fold is not tilted as in model D, resulting in a better fit of the pre-growth strata to the seismic section. This model, however, also fails to simulate the syncline near the ØFC.

As shown by models E to H, adding more sediment growth to the simulations resulted in slightly different fold and growth strata geometries. The models with moderate growth (base level rise of 1e-5 m/timestep) gave a slightly worse fit to the seismic section than the models with strong growth (base level rise of 4e-5 m/timestep). More sediment growth therefore seems to improve the fit to the section. However, there are still major problems replicating the local hanging wall syncline close to the ØFC.

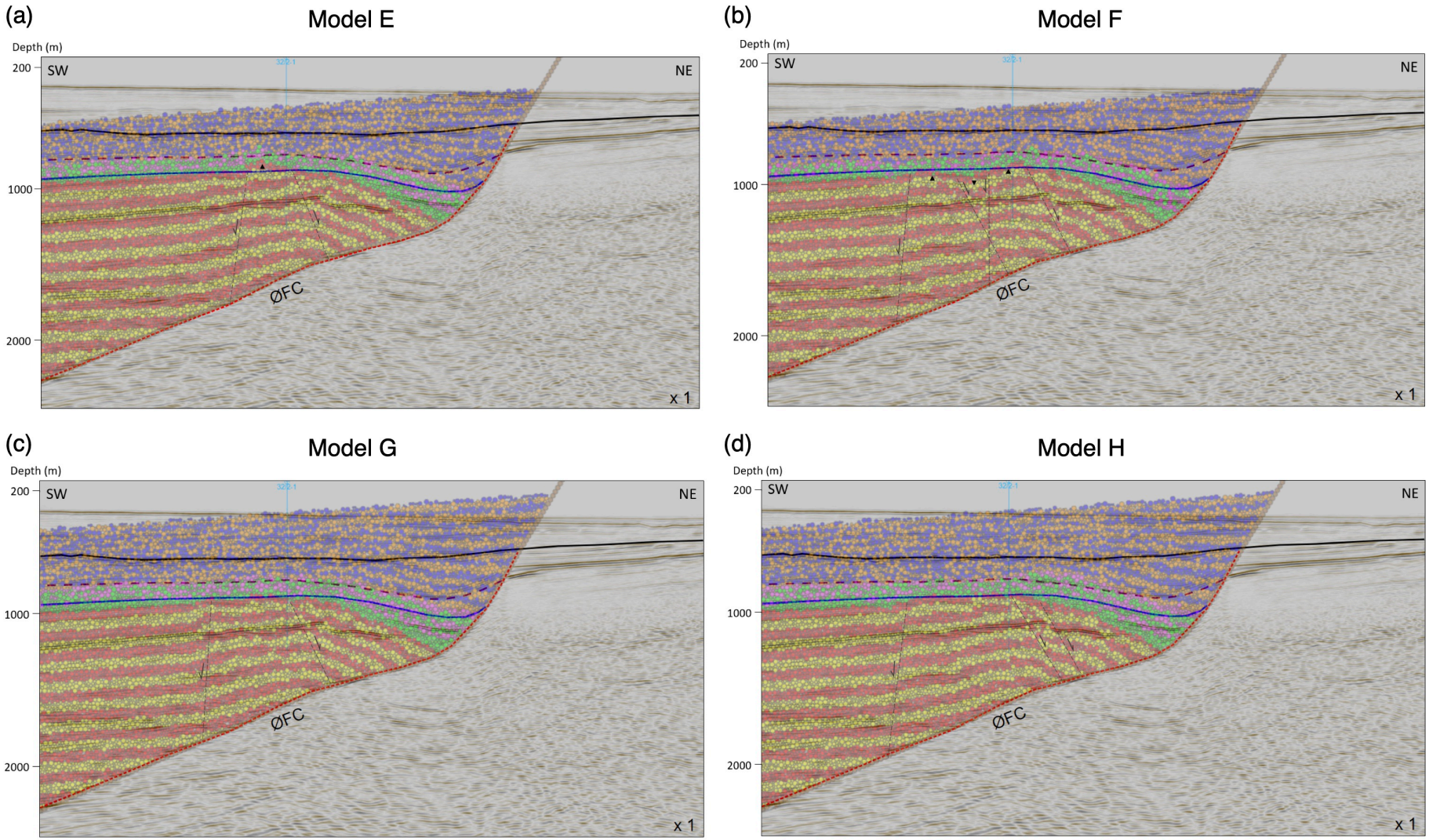

Figure 23: *Variations of model C (half friction and cohesion) and model D (flexural slip) with more growth. (a) Model E: model C with moderate growth, (b) Model F: model D with moderate growth, (c) Model G: model C with strong growth, and (d) Model H: model D with strong growth. Upward triangles indicate anticlines, downward triangles indicate grabens.*

Fault Friction

In an attempt to get a better fit with the seismic section, and to create a "drag" effect close to the ØFC, the effect of fault friction was tested. Using models C and D, the fault friction was both reduced and increased. The contact friction between the elements and the fault walls in both models was first reduced to 0.05, and then increased to 1.0. The results of the reduced and increased fault friction models (not included here) are very similar to the original models C and D. The fold geometry has only minor changes, and with no improvement in the fit to the local syncline close the ØFC. Therefore, fault friction doesn't have any significant impact on the modelled fold and is not considered any further.

5.2.2 Section 2

Model I (Default)

Model I is the default model for section 2 and uses the same parameters as model A, but with the ØFC geometry from seismic section 2 (Table 2). Figure 24 shows the final geometry of model I superimposed on seismic section 2. A hanging wall anticline has formed, with antithetic normal faults offsetting the forelimb of the structure. A synthetic reverse fault can also be seen on the western part of the model, offsetting the pre-growth strata in the backlimb. On the backlimb and crest of the structure, the top of the pre-growth fits well with the pre-growth in the seismic section. In the forelimb near the ØFC, there is mismatch as the pre-growth strata are too deep and steep, and they fail to simulate the hanging wall syncline. The modelled growth strata near the fault also fail to model the syncline but have a good fit with the rest of the section. The modelled top of GP1 is better near the crest of the structure than in the backlimb where it is too deep. Overall, the fit of model I to section 2 is better than any of the other models for section 1.

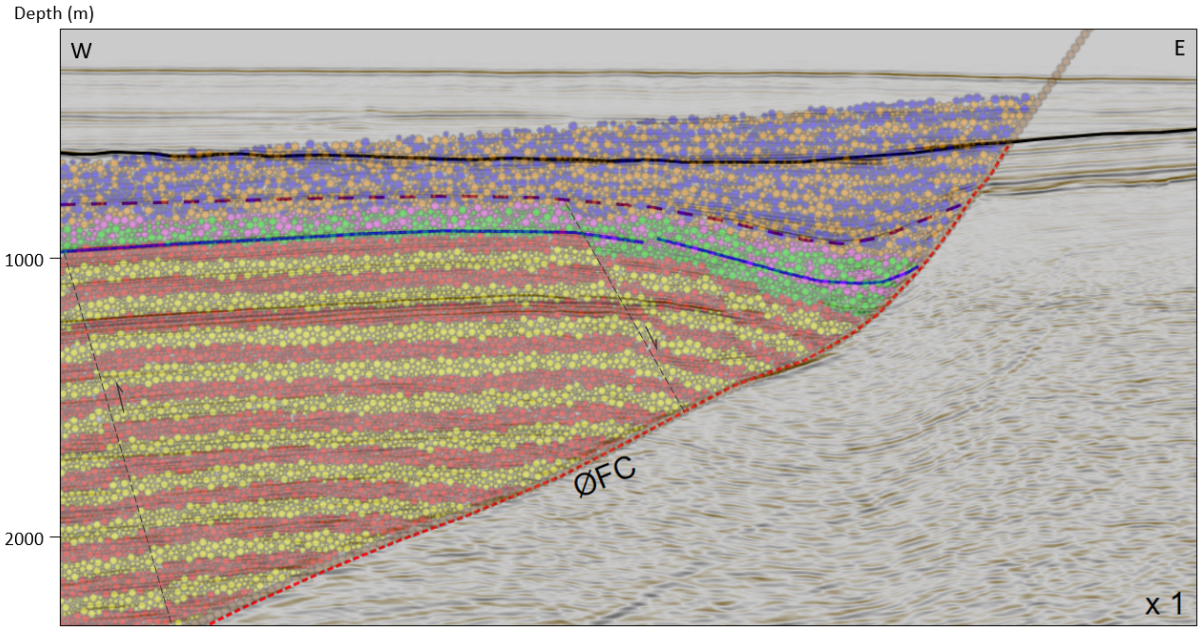

Figure 24: *Final geometry of model I superimposed on seismic section 2.*

Figure 25 illustrates the evolution of the structure. Early in the evolution of the model at 33% total displacement (Figure 25a), a syncline is formed above the concave upwards fault bend (1), and an anticline above the convex upwards fault bend (2). As displayed by γ_{max} and the low u_y triangular area near the fault, the forelimb of the structure has collapsed along

antithetic normal faults. At 66% total displacement (Figure 25b), the forelimb of the structure has collapsed more as it has been translated downwards along the convex upwards fault bend (2). At this stage, a syncline has developed in the pre-growth and growth strata. A synthetic reverse fault has also started to develop above a lower concave upwards fault bend (3), breaching through the pre-growth strata on the western part of the model. At 100% total displacement, this reverse fault has been translated downwards over a slight convex upwards fault bend (4) in the lower fault segment and its offset increased (Figure 25c). The collapse of the forelimb and offset of antithetic normal faults have also increased. At this stage, the hanging wall syncline in the pre-growth strata has disappeared, but in the growth strata it is still present. Thickening of the strata towards the ØFC occurs throughout the evolution of the model in both growth packages GP1 and GP2 (Figure 25a-c).

From this evolution it is clear that:

- Just like in section 1, the syncline is related to the concave upwards fault bend, and the anticline to the convex upwards fault bend. The syncline forms in the early to intermediate stages of the structure, but it collapses when the elements are dragged along the low angle segment of the fault.
- Reverse faulting in the backlimb occurs more to the west, and it first develops over a concave upwards fault bend, and amplifies latter over a convex upwards fault bend.
- Collapse of the forelimb of the structure occurs over the entire structure´s evolution.
- As in section 1, there are still problems replicating the local syncline near the ØFC.
- For the more complex fault geometry of section 2 with more bends, the default model displays more distributed deformation than in section 1, and the fit to section 2 is better than in section 1.

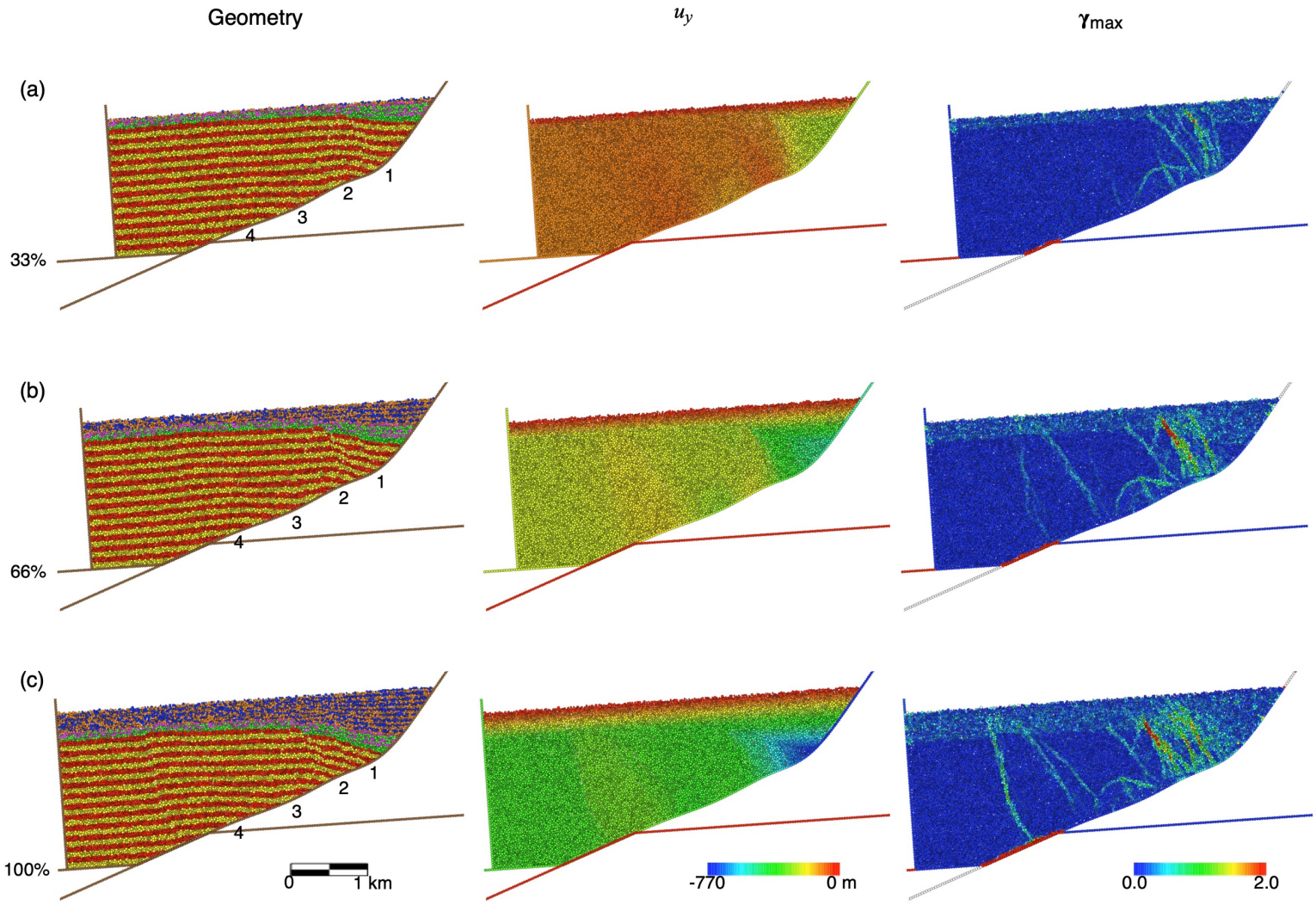

Figure 25: *Results of model I shown at (a) 33%, (b) 66% and (c) 100% total displacement. The geometry is shown to the left, the total vertical displacement on the middle, and the total maximum shear strain on the right. The concave and convex fault bends are labelled from 1-4.*

Model J (Half friction and cohesion)

Model J uses the same parameters than model I, except in this case the contact friction between the elements, and between the elements and the walls have been reduced to 0.125, and the cohesive force between the elements have been reduced to 3e7 N (Table 2). This model therefore has half the strength of model I.

Figure 26 shows the final geometry of the model superimposed on seismic section 2. As in Model I, a hanging wall anticline is formed. However, in this model, the forelimb of the fold is not clearly offset by normal faults. Normal faults are present in the forelimb, but with a smaller offset and they don't reach the top of the pre-growth. Synthetic and antithetic normal faults can be seen in the backlimb of the structure, creating a small graben (downward triangle). The fit to the pre-growth strata in the seismic section is good, except for a slight mismatch near the ØFC where the syncline is not replicated. The model also fits reasonably well the growth strata in the section, but there are some problems to the west away from the fault where the normal faults offsets the growth sediments, and the eastern limb of the syncline close to the ØFC, where the modelled growth strata are gentler than in the seismic section.

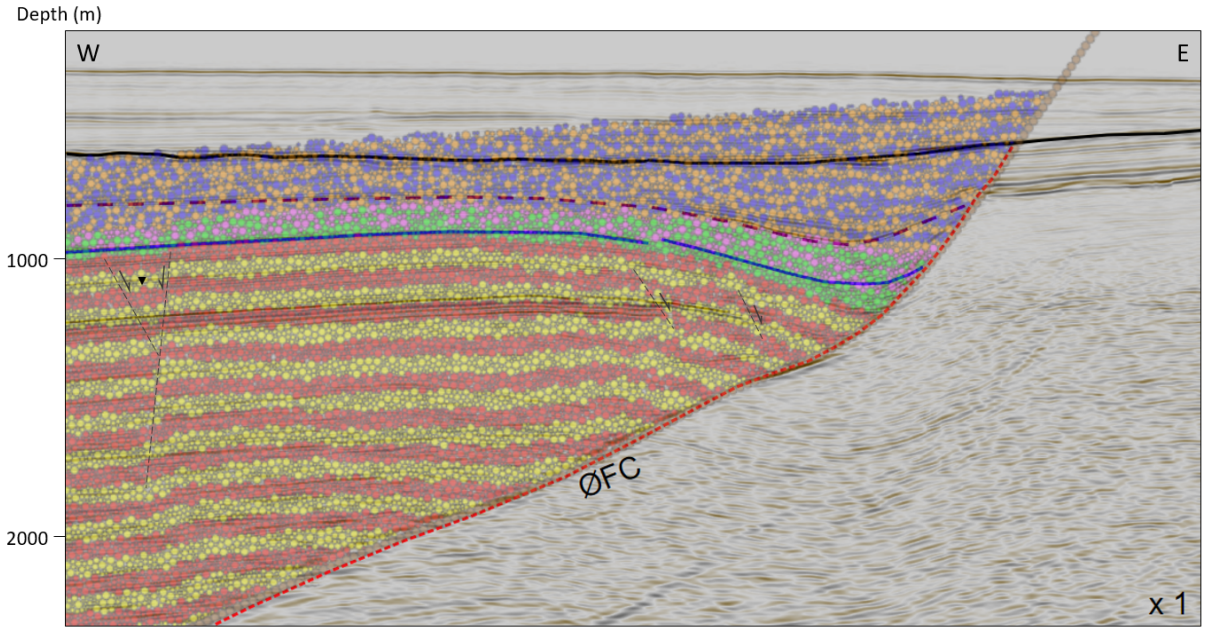

Figure 26: *Final geometry of model J superimposed on seismic section 2. Downward triangle indicates a graben.*

Figure 27 shows the evolution of the structure. At 33% total displacement (Figure 27a), the model is similar to model I, with a syncline above the concave upwards fault bend (1) and an anticline above the convex upwards fault bend (2). However, at 66% total displacement, the model differs from model I near the ØFC. As displayed by γ_{max}, model J has less strain localisation than model I. Therefore, the forelimb of the fold is not clearly offset by antithetic normal faults but collapses in a more distributed manner, as displayed by the model's geometry and u_y (Figure 27b). In this model, a synthetic normal fault develops on the western part of the model, and in addition, an antithetic normal fault also develops crossing the antithetic normal fault as displayed by γ_{max}. At 100% total displacement (Figure 27c), the forelimb of the fold has collapsed further. The normal faults also continue to offset the pre-growth strata as they are translated over the lower convex upwards fault bend (4) creating a small graben.

From this evolution it is clear that:

- An anticline forms in the hanging wall, but compared to model I, the forelimb of the structure is not clearly offset by antithetic normal faults but collapses in a more distributed manner.
- This model fits better the seismic section than the default model I.
- The model still has some problems replicating the hanging wall syncline close to the ØFC, both in the pre-growth and growth strata.

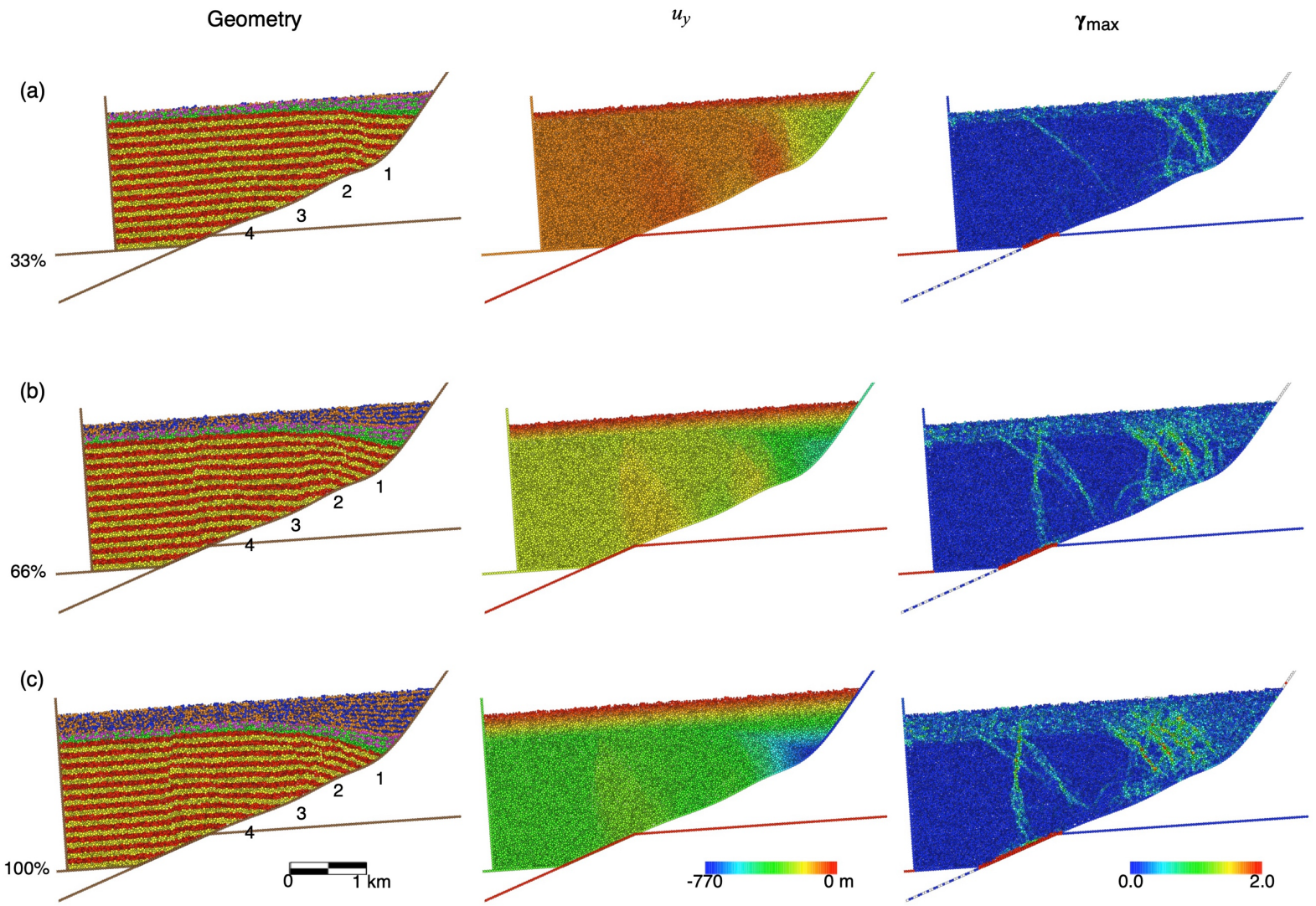

Figure 27: *Results of model J at (a) 33%, (b) 66% and (c) 100% total displacement. The geometry is on the left, the total vertical displacement in the middle, and the total maximum shear strain on the right. The concave and convex fault bends are labelled from 1-4.*

Model K (Flexural slip)

Model K uses the parameters of model I, but in this case flexural slip is added (Table 2). Figure 28 shows the final geometry of model K superimposed on seismic section 2. Compared to models I and J, in this model antithetic normal faults offset the crest of the fold creating a local anticline (triangle in figure). The top of the pre-growth strata in the backlimb has a reasonable fit to the seismic section. However, the fit is not as good at the crest of the fold where the modelled pre-growth strata is too deep. The model also fails to replicate the hanging wall syncline close to the ØFC. The modelled growth strata in the eastern limb of the syncline is too gentle in comparison to the observed growth strata dips, and the top of GP1 is also too deep in the backlimb of the structure.

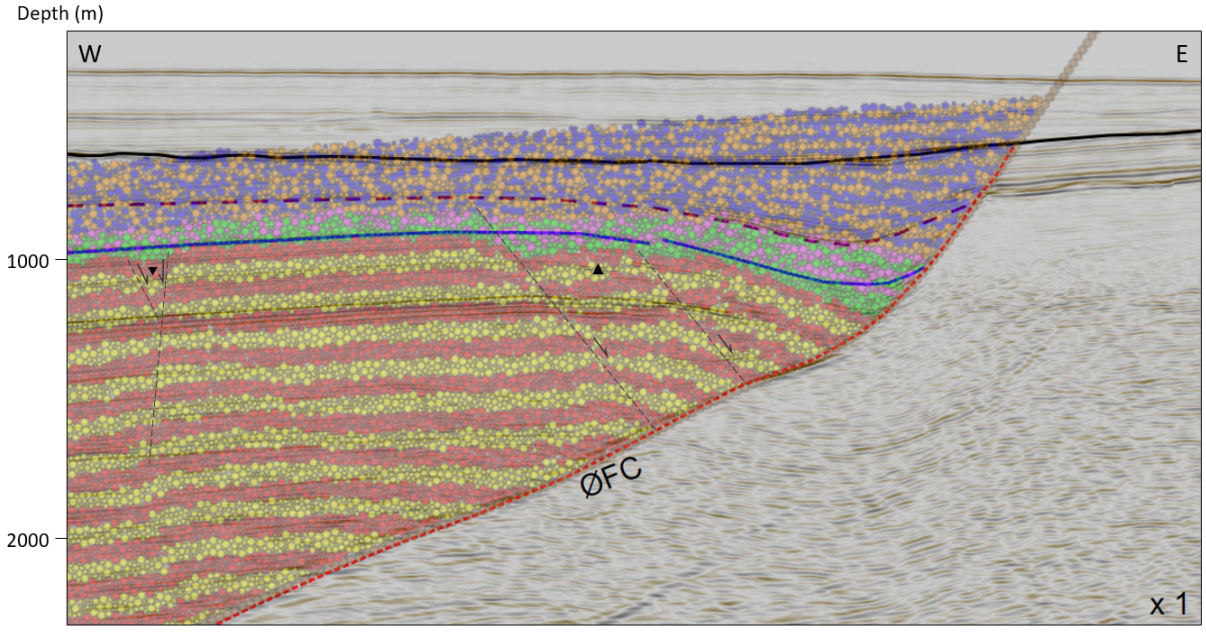

Figure 28: *Final geometry of model K compared to seismic section 2. Upward triangle indicates a local anticline, and downward triangle a graben.*

Figure 29 shows the evolution of model K. Early in the evolution of the model at 33% total displacement (Figure 29a), the results differ from models I and J. There is more strain localisation in the antithetic normal faults (γ_{max}, Figure 29a), and the faults nucleate further down the ØFC, with a lower dip than in the other models. Therefore, the faults breach the fold further west, which is at the crest. This is also displayed well by u_y, where the triangular area with the maximum downward displacement is wider than in the other models, stretching further west. At 66% total displacement (Figure 29b), the forelimb of the fold continues to collapse, and a local anticline (upward triangle) forms in the hanging wall of the antithetic

normal fault. There is also a syncline in both the pre-growth and growth strata near the ØFC. At this stage, normal faults similar to those formed in model J offset the pre-growth strata. At 100 % total displacement (Figure 29c), the syncline near the ØFC has disappeared and the layers show a steep forelimb.

From this evolution it is clear that:

- Antithetic normal faults offset the forelimb further west (close to the crest) than in the other models.
- This model has a slightly better fit with the seismic section than model I, but a worse fit than model J due to the offset of pre-growth strata near the crest.
- The model has problems replicating the local hanging wall syncline close to the ØFC, both in the pre-growth and growth strata.

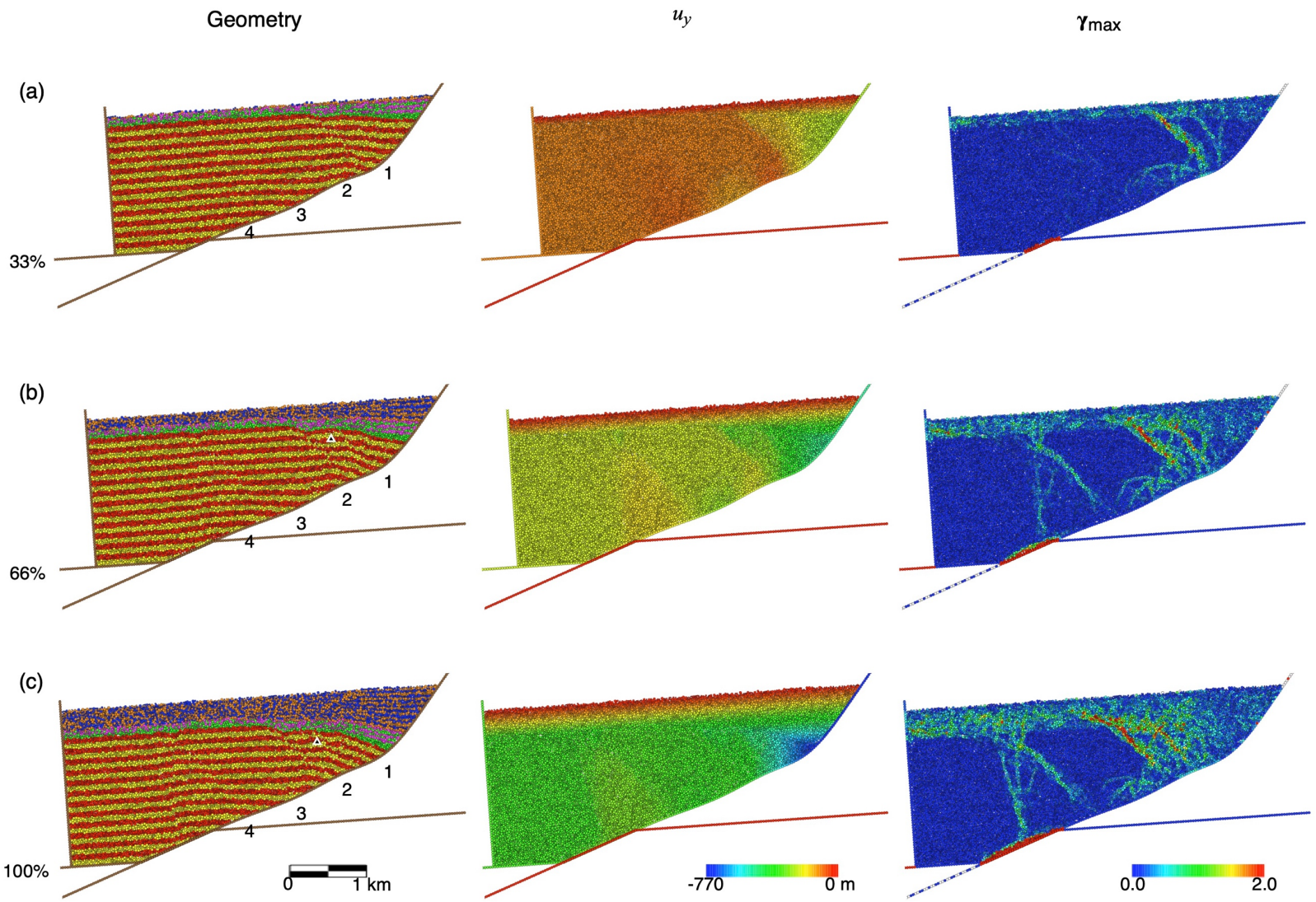

Figure 29: *Results of model K at (a) 33%, (b) 66% and (c) 100% total displacement. The geometry is shown on the left, the total vertical displacement in the middle, and the total maximum shear strain on the right. The concave and convex upwards fault bends are labelled from 1-4, and the local anticline is marked with a triangle.*

Models L, M, N and O

As in section 1, more sediment growth was added to models J and K. Model J yields models L and N, and model K yields models M and O. Models L and M have a moderate base level rise of 1e-5 m/timestep, while models G and H have a strong base level rise of 4e-5 m/timestep (Table 2).

Model L in Figure 30a shows a very similar fold geometry than model J. The most significant difference is the slightly down-faulted segment at the crest of the fold. In this model, there are antithetic normal faults in the forelimb of the fold, as in model J. However, a synthetic normal fault also forms, creating a small graben (marked by a triangle) at the crest of the structure. The growth strata are also affected by the small graben. The fit to the top of the pre-growth in the section is worse than in model J, as the crest of the fold is too deep. This model also fails to model the syncline close to the ØFC.

In Model M (Figure 30b), increased sediment growth did not introduce any significant changes to the final geometry of the structure. Compared to model K, the antithetic and synthetic normal faults display a higher shear strain and offset. This also affects the growth strata above, which results in a slightly worse fit to the seismic section than in model K.

Model N (Figure 30c) is very similar to Model L. The small graben at the crest of the fold can also be seen in this model, but with a slightly thicker GP1 than in model L. Antithetic and synthetic normal faults like in models J and L develop, but the offset of the pre-growth strata along these faults is smaller. The model has a similar fit to the seismic section than model K, with a slightly better fit to the top of GP1 in the backlimb of the structure.

For model O (Figure 30d), adding even more sediment growth to the simulation results in a better fit to the seismic section than in models K and M. In this model, the sediments in the graben at the crest of the fold have a smaller offset than in model M, and therefore the fit at the crest of the fold is better. The offset of the pre-growth and growth strata along the reverse fault is also less in this model. The modelled top of GP1 is better in the backlimb and crest of the structure, but it is too thick in the forelimb.

From the models L to O, it is clear that adding more sediment growth can make the fit of the models to the seismic section better or worse. Adding moderate growth gives slightly worse results, while adding strong growth gives both slightly worse (model N) and slightly better (model O) results.

Conclusion about models A to O

From the observations of the different models A to O for sections 1 and 2, it is clear that they all have problems replicating the local syncline close to the ØFC. However, some models gave better fits than others. Models with half strength (C, E, G, J, L and N), or flexural slip (D, F, H, K, M and O) give better results than the default models (A and I). Half strength or flexural slip results in more distributed deformation and less uplift of the backlimb and crest of the anticline. It is however hard to say which of these two sets of models are better, as both have their problems. Regardless, the models with strong sediment growth (G, H, N and O) gave the best fit to both the pre-growth and the growth strata, and the fit in section 2 (more complex fault geometry) is better than in section 1.

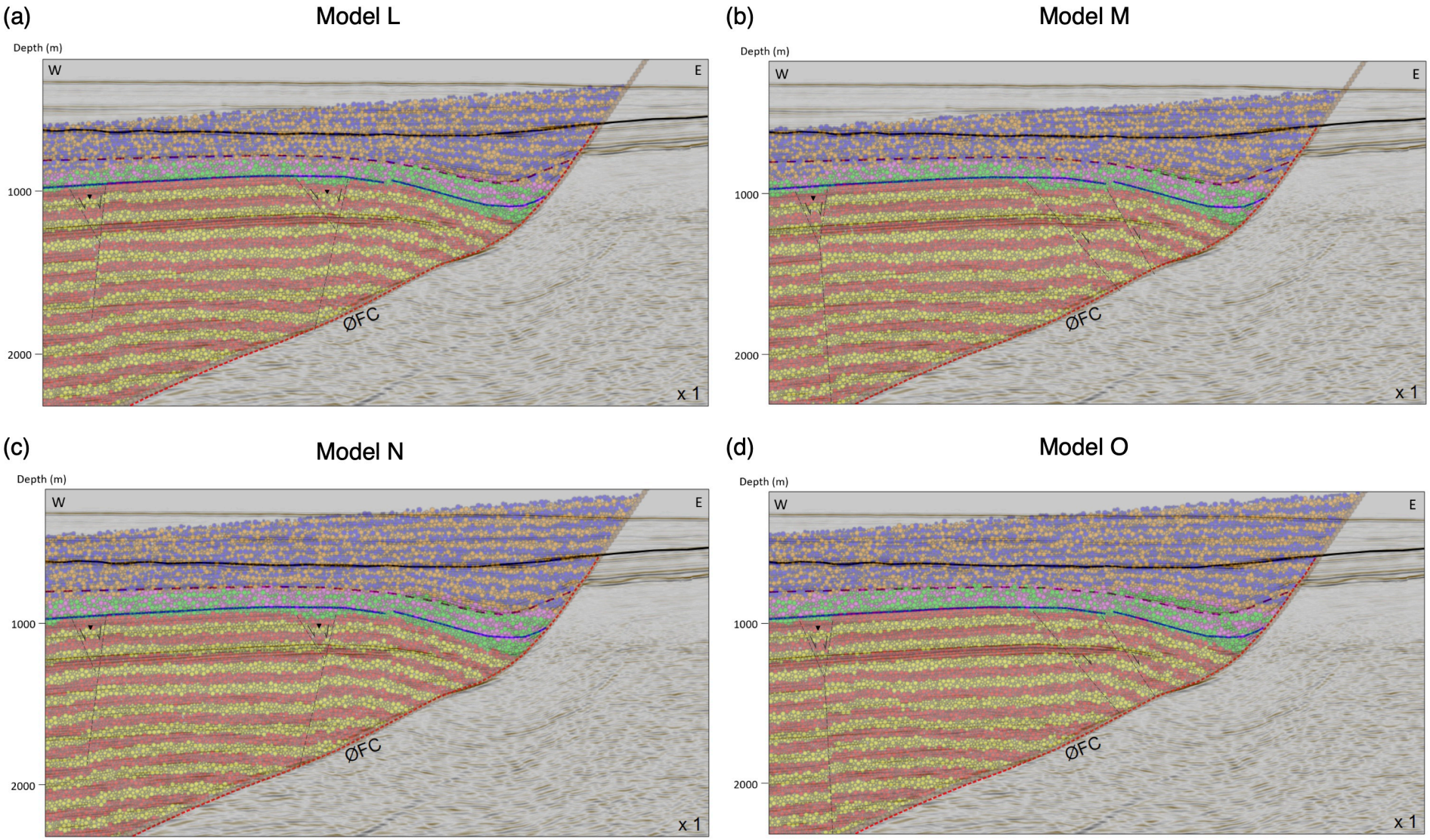

Figure 30: *Variations of model J (half friction and cohesion) and model K (flexural slip) with more growth. (a) Model L: model J with moderate growth, (b) Model M: model K with moderate growth, (c) Model N: model J with strong growth, and (d) Model O: model K with strong growth. Downward triangles indicate grabens.*

5.2.3 Inversion

In all the models above, the structure is simulated as an extensional fault-bend fold, with normal-fault movement along the ØFC. However, as stated by Wu et al. (2021), it is possible that the Beta structure was affected by tectonic inversion during the Neogene. In this section, I analyse the effect of tectonic inversion on the simulations.

Model P (Inversion)

For modelling tectonic inversion on section 1, I use the parameters of model D which includes flexural slip. In this model, the total run time was increased from 20,000 to 25,000 s, and the inversion started at 75% of the total run time (Table 2).

Figure 31 shows the final geometry of model P superimposed on seismic section 1. The final geometry shows that the model is quite different to model D in the crest of the fold and close to the ØFC. In this model, the modelled top of the pre-growth strata and the growth strata closest to the ØFC fit better the seismic section as the modelled forelimb of the fold is less steep, and the growth strata displays a syncline near the fault. However, the fit is still not sufficiently good as the eastern limb of the hanging-wall syncline is steeper in the seismic section compared to the modelled pre-growth and growth strata. The GP1 is also way too thick in this area. In the backlimb of the fold, the model does a good job in replicating the top of the pre-growth strata as well as the top of GP1. In the crest of the fold, the modelled pre-growth strata and growth strata are too high and do not fit well the seismic section.

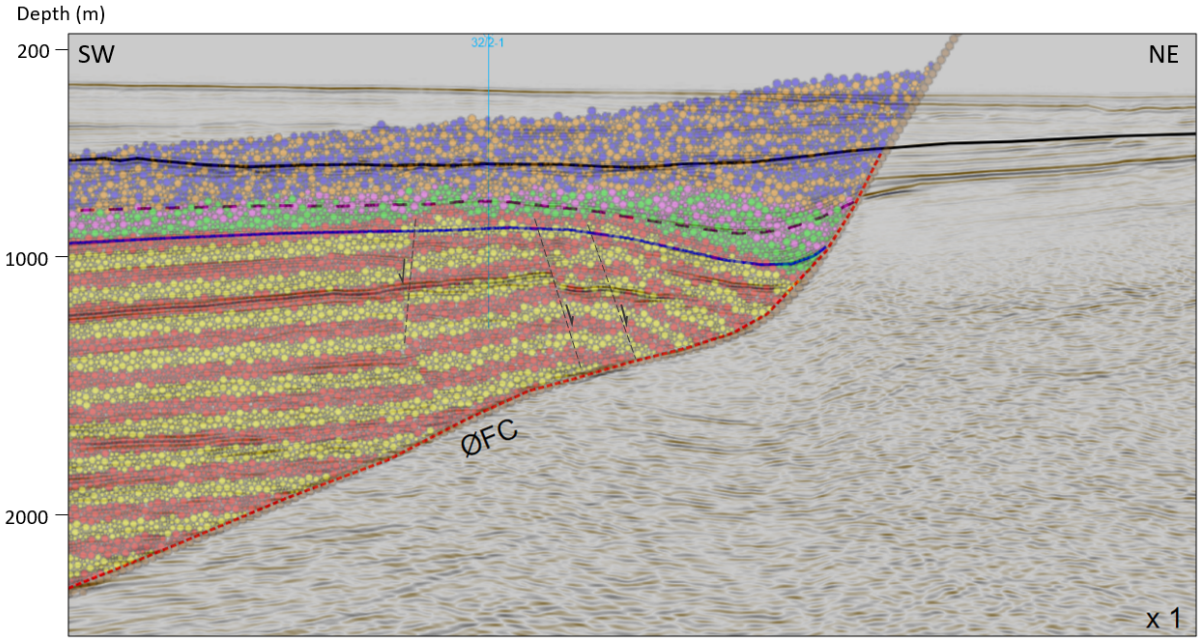

Figure 31: *Final geometry of model P, tectonic inversion, compared to seismic section 1.*

Figure 32 shows the evolution of model P during the phase of tectonic inversion. Figure 32a shows the model at the maximum normal fault displacement, Figure 32b at the middle of the inversion, and Figure 32c at the end of the inversion. At the maximum normal fault displacement, a fold structure has formed in the hanging wall similar to the final geometry of model D (Figure 21). The forelimb of the structure is steep as it has collapsed and the elements have been translated over the concave upwards fault bend (Figure 32a, geometry and u_y). A synthetic normal fault offsets the backlimb of the structure, and antithetic normal faults have developed at the crest. At this stage, inversion starts and half-way through the inversion (Figure 32b) the forelimb of the fold has become gentler as the sediments have been translated upwards along the concave upwards fault bend (Figure 32b, geometry and u_y). Tectonic inversion continues, and the elements are translated upwards over the concave fault bend. By the end of the inversion (Figure 32c), the forelimb of the anticline is gentler, and a gentle syncline in the pre-growth and growth strata has formed.

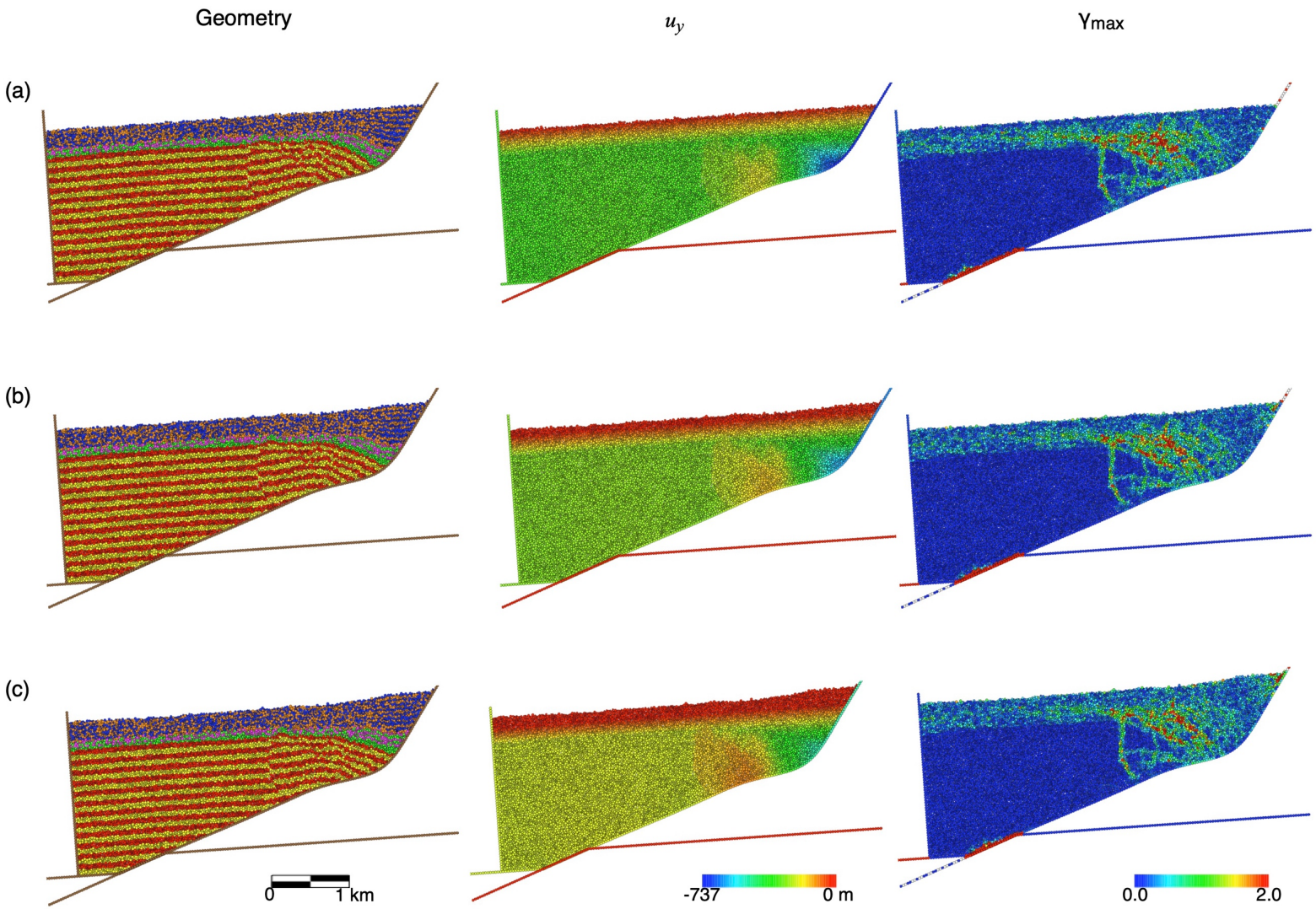

Figure 32: *Results of model P, tectonic inversion-section 1, at (a) maximum normal fault displacement, (b) mid-inversion and (c) end of inversion. The geometry is shown on the left, the total vertical displacement in the middle, and the total maximum shear strain on the right*

Model Q

For the modelling of inversion on section 2, I used the parameters of model K. As in model P, the total run time is increased from 20,000 to 25,000 s, and the inversion starts at 75% of the total run time (Table 2).

Figure 33 shows the final geometry of model Q superimposed on seismic section 2. Compared to the final geometry of model K, the backlimb and the crest of the fold is less faulted. The forelimb is less steep, with a small graben near the crest. The modelled pre-growth and the growth strata in the backlimb of the fold have a good fit to the seismic section, but is too high in the forelimb, especially the top of GP1. Compared to model K, this model has a slightly better fit overall.

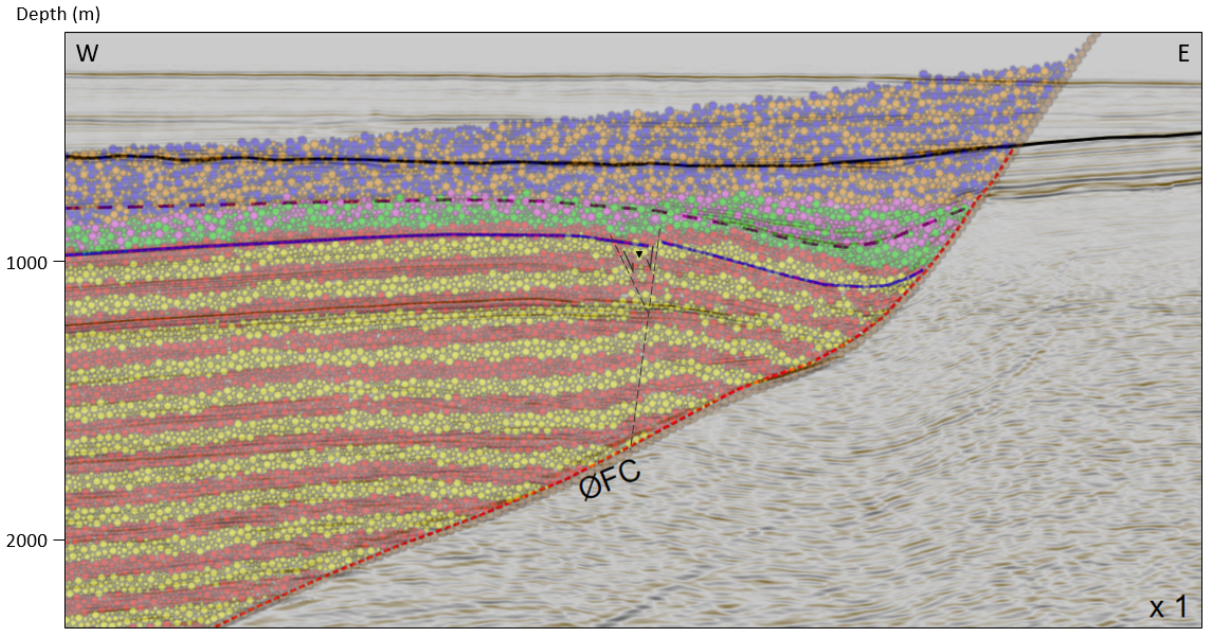

Figure 33: *Final geometry of model Q, tectonic inversion, compared to seismic section 2. Downward triangle indicates a graben.*

Figure 34 shows the evolution of model Q during the phase of tectonic inversion. Figure 34a shows the model at the maximum normal fault displacement, Figure 34b at the middle of the inversion, and Figure 34c at the end of the inversion. Figure 34a shows a similar geometry as model K in Figure 29b. An anticline has developed, with normal faults offsetting both the crest and backlimb of the fold. At the middle of the tectonic inversion (Figure 34b), the forelimb has been translated upwards along the concave upwards fault bend, making it gentler

(Figure 34b, geometry and u_y). At the end of the tectonic inversion (Figure 34c), the forelimb is even gentler, and the growth strata above have been translated upwards.

By displacing the elements upwards along the concave upwards bend of the ØFC, tectonic inversion results in a gentler forelimb in the pre-growth strata, and a local syncline in both the pre-growth and growth strata (Figures 32 and 34). These features resemble more sections 1 (Figure 31) and 2 (Figure 33). However, the eastern limb of this syncline is too gentle in comparison to the actual one, and this dip difference is more marked in the growth-strata (e.g. GP1-GP2 contact) than in the pre-growth strata (e.g. top pre-growth).

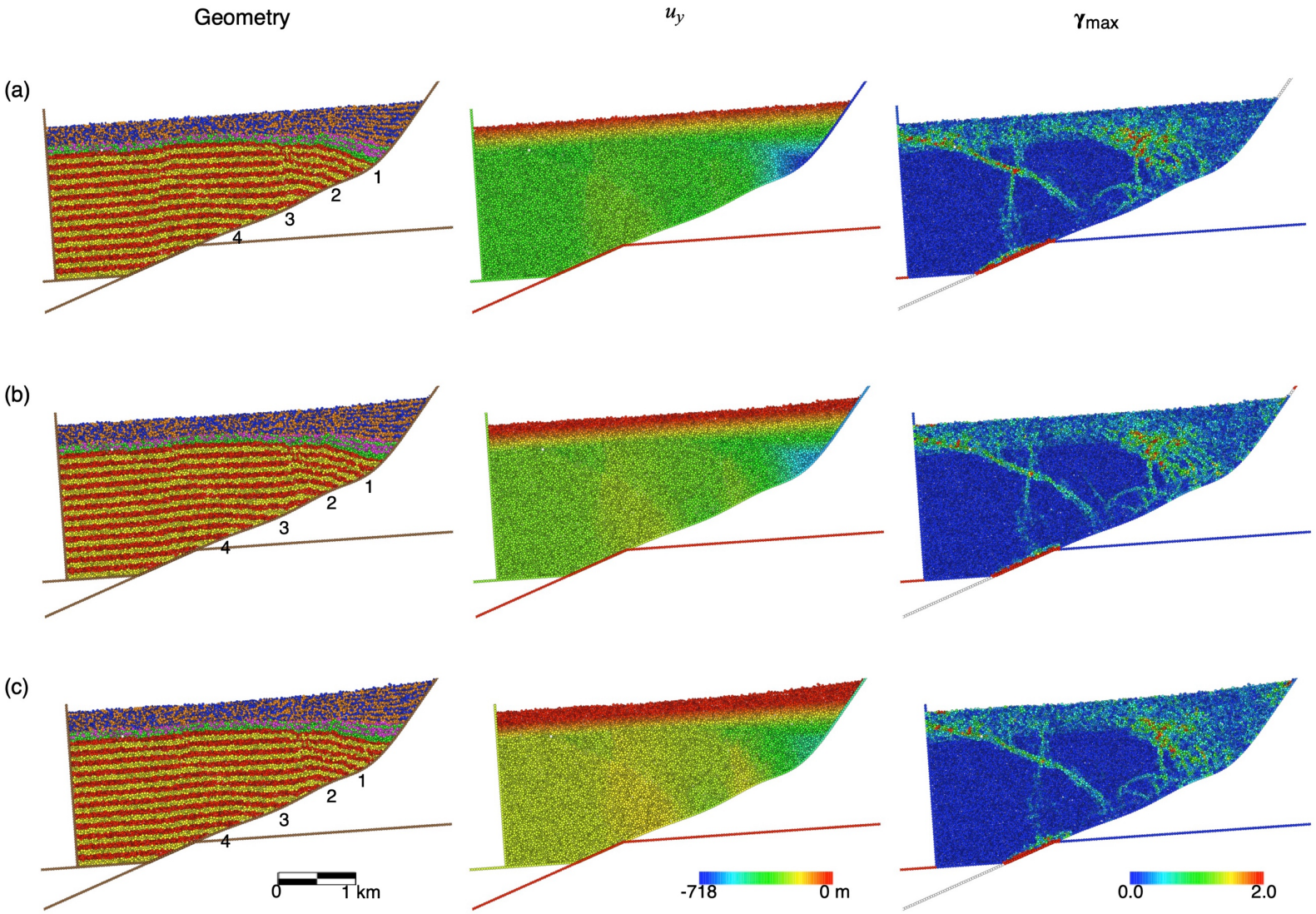

Figure 34: *Results of model Q, tectonic inversion-section 2, at (a) maximum normal displacement, (b) mid-inversion and (c) end of inversion. The geometry is shown on the left, the total vertical displacement in the middle, and the total maximum shear strain on the right.*

6 Discussion

6.1 DEM modelling vs. kinematic modelling

Kinematic modelling based on inclined shear does a reasonable job in replicating the Beta structure. However, this model is very sensible to the geometry of the fault, where small changes in fault geometry result in significant changes in the modelled horizons. Getting a good fit with the interpreted horizons took a great amount of time, and it involved making very small changes to the geometry of the fault at a given try. Secondary faults can be predicted via strain ellipses, but they cannot be modelled explicitly with this technique.

DEM mechanical modelling also gave a reasonable fit to the Beta structure. Compared to the kinematic model, the DEM gives a much more detailed picture of the evolution of the structure and sediment growth. Secondary faults are a natural outcome of the model, and their development can be tracked via incremental or total strain. DEM enables studying the effect of sediment growth, material strength, and material anisotropy (flexural slip). Analysing the impact of tectonic inversion was also possible using mechanical modelling. A disadvantage of DEM with respect to kinematic modelling, is that it is much more difficult to fit a structure with the DEM. The initial setup of Figure 15 is just a "possibility" that yields a high fault displacement model (~1 km), which is somewhat consistent with the kinematic model (~ 0.8 km). There might be lower fault displacement DEM models that provide similar or better fits.

For both modelling techniques, it is important to notice that the modelling is based on seismic interpretations, which have uncertainties especially regarding time-to-depth conversion and the geometry of the ØFC. As seen in the kinematic and mechanical modelling, small changes in the fault geometry can result in significant changes in the hanging wall structure. The interpretations of the different horizons are also challenging, especially close to the fault where the signal to noise ratio is lower.

6.2 Structural evolution

In this thesis, the Beta structure was mainly simulated as an extensional fault-bend fold, in both the kinematic and DEM models. The ØFC geometry as interpreted today was "there" at the beginning of the model, and the structure formed by normal movement of the hanging

wall along the non-planar ØFC. The results support this hypothesis; the anticlinal structure is related to a convex upwards fault bend, and the synclinal structure to a concave upwards fault bend above. The forelimb of the structure collapses towards the ØFC along antithetic normal faults, and the backlimb is affected by either synthetic reverse or synthetic normal faults. The fit is better in section 2, where the ØFC has a more complex geometry (more fault bends) than in section 1. More distributed deformation by either decreasing rock strength (models C and J), or flexural slip (models D and K), and increased syn-sedimentation (models G, H, O) give better fits. However, extensional fault bend folding alone does not explain the structure, especially the local syncline and the steep westward dips (synthetic dips; Ferrill et al., 2005) of pre-growth and growth strata close to the ØFC. The following mechanisms may have additionally contributed to the development of the structure.

6.2.1 Inversion

The Beta structure may have experienced minor local inversion during the Neogene uplift (Wu et al., 2021). Tectonic inversion and reactivation of the ØFC as a reverse fault (Indrevær et al., 2016) gave a variable result with regards to the fit with the seismic section (Models P and Q, Figures 31 and 33). Although tectonic inversion resulted in a better fit in some parts of the fold, it created some problems at the crest of the fold, especially in section 1. Tectonic inversion did, however, result in a more reasonable forelimb when compared to the seismic section, which is less steep than in the other models without inversion, and displays a local syncline, especially in section 2 (Figures 31 and 33). However, tectonic inversion does not replicate the steep westward dips close to the ØFC, the modelled syncline in section 2 is too open in comparison to the actual one. Based on these results, it is not clear that inversion has affected the structure, but still it cannot be ruled out. It should also be noticed, that inversion was applied to the flexural slip models D and K. Different models with or without inversion may result in a better fit.

6.2.2 Other mechanisms

Results from both the kinematic and mechanical modelling suggest that other mechanisms may be the cause of the local hanging wall syncline near the ØFC. There are several mechanisms capable of producing hanging wall synclines in normal faults, and below I discuss two of the most important.

Compaction

Skuce (1996) shows that compaction can be the cause of large fold structures in the hanging-wall of normal faults, and this effect can be considerable above listric faults that involve basement. As described earlier, compaction hanging wall synclines are formed if the footwall is rigid and the hanging wall is less consolidated. The hanging wall will then compact more than the footwall and a syncline will form. Compaction is often hard to recognize as the anticlinal structures of rollovers have a magnitude equal to or greater than the synclinal structures produced by the compaction. The product of compaction and rollover folding is a syncline near the fault and a larger anticline further away (Skuce, 1996). Withjack and Peterson (1993) show how the shape of fault-bend folds can be altered by compaction, by compacting the hanging-wall strata of a fault-bend fold. The result is a small hanging wall syncline near the listric fault (Withjack & Peterson, 1993) (Figure 35). This is a reasonable description for what may have happened in the Beta structure. As the ØFC puts in contact basement in the footwall with sediments in the hanging wall, it is realistic that differential compaction may have affected the hanging wall geometry in some way. The crucial question is if the resultant syncline by compaction will have the size and asymmetry of the syncline close to the ØFC. This needs to be investigated further.

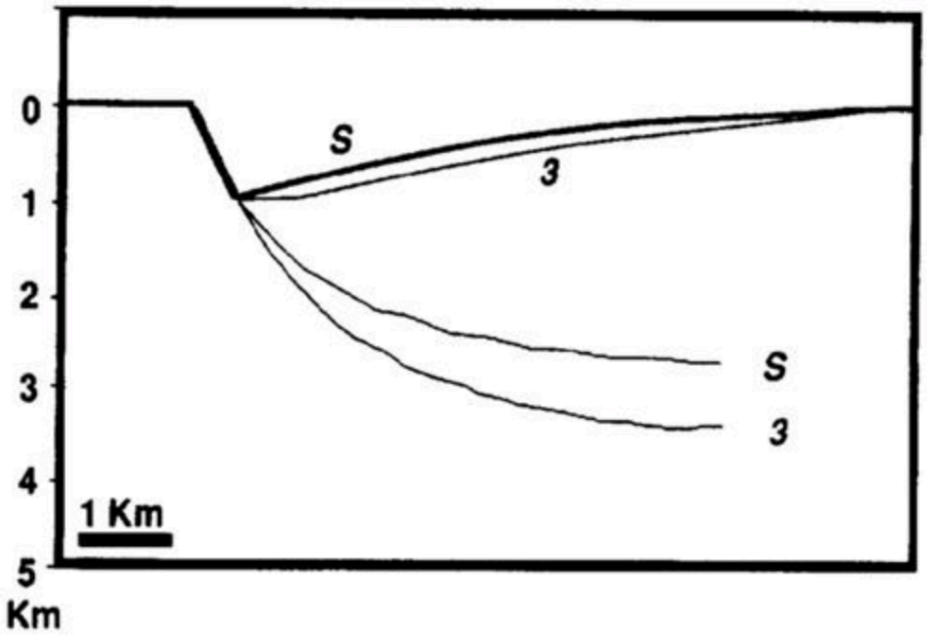

Figure 35: *Fault-prediction model showing a standard fold (S) which has been modified by compacting the hanging-wall strata (3). Modified from Withjack & Peterson (1993).*

Fault propagation folding

Extensional fault propagation folding is recognized as an important process in extensional basins, and results in distinctive hanging wall synclines and minor footwall anticlines (Hardy, 2019). In the Beta structure, there is only a thin package of strata preserved in the footwall, making it hard to use as evidence for vertical propagation of the fault. Though there is a clear hanging wall syncline present along the ØFC. The "normal drag" observed in the seismic sections is consistent with the breach of a monocline forming ahead of a fault as it propagates up section (Mulrooney et al., 2020). In addition, as mentioned earlier, the preserved sediments in the footwall of the structure dip to the west (towards the hanging wall). This synthetic dipping nature of the sediments also correspond to the breach of monoclines as most of the folding is preserved in the hanging wall (Ferrill et al., 2005; Mulrooney et al., 2020) (Figure 1).

The Goliat anticline in the hanging wall of the Troms Finnmark Fault Complex (TFFC), Barents Sea, is a structure similar to Beta, formed by normal movement along a non-planar fault. A similar "drag effect" close to the main fault as observed in the Beta structure, can be seen in the Goliat structure (Mulrooney et al., 2017) (Figure 36). Mulrooney et al. (2017) suggest that this geometry is indicative of a breached fault propagation monocline.

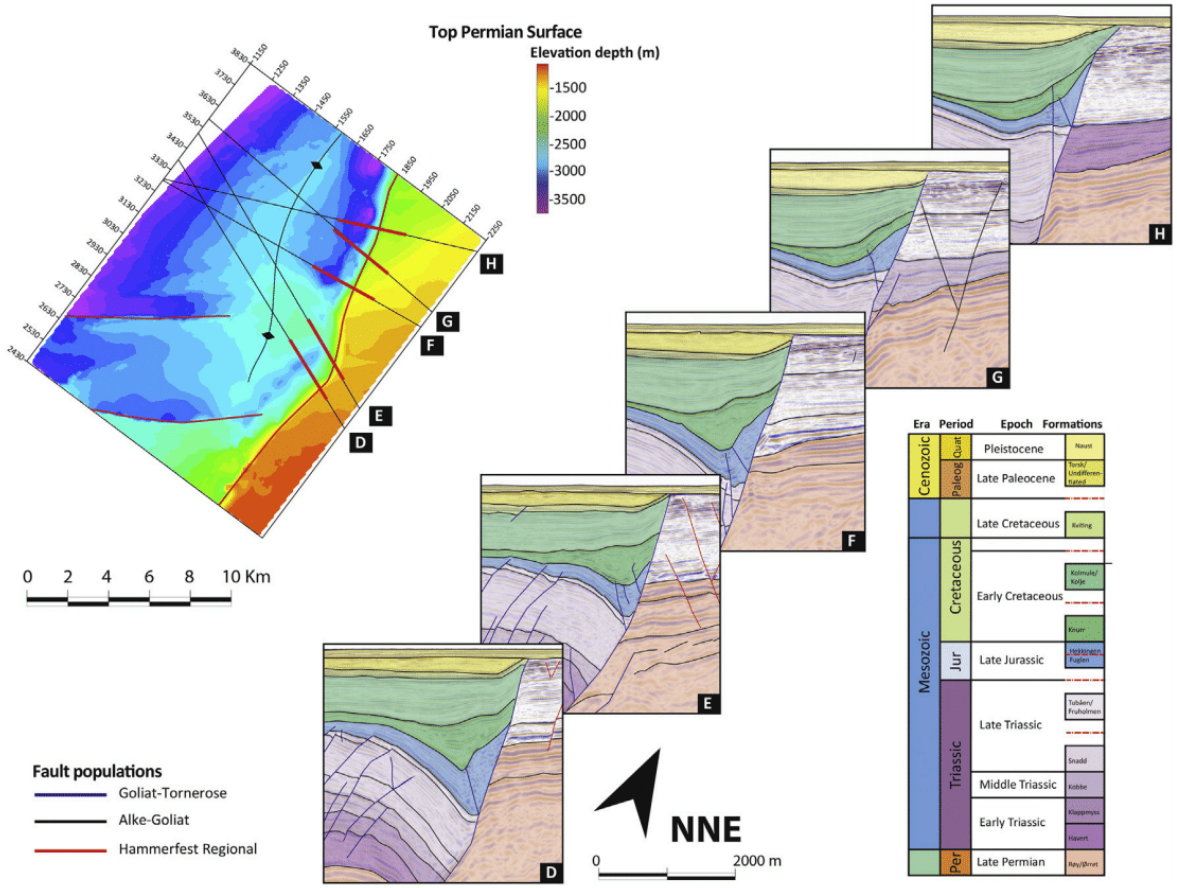

Figure 36: *The Goliat anticline with drag effect near the main fault. From Mulrooney et al. (2017).*

The Goliat structure also experienced a phase of local inversion, creating local compression structures above blind faults (Mulrooney et al., 2017). Mulrooney et al. (2017) proposed a conceptual evolutionary model of the Goliat structure (Figure 37). This model includes progressive growth and propagation of a normal fault, with trishear-like folding ahead of the fault and secondary faulting and rotation in the backlimb (Figure 37 A-B). Then, a phase of tectonic inversion accentuates the hanging wall structure (Figure 37 C), followed by erosion (Figure 37 D). A similar evolution of the Beta structure, with perhaps the effect of tectonic inversion during the Neogene could be a reasonable hypothesis.

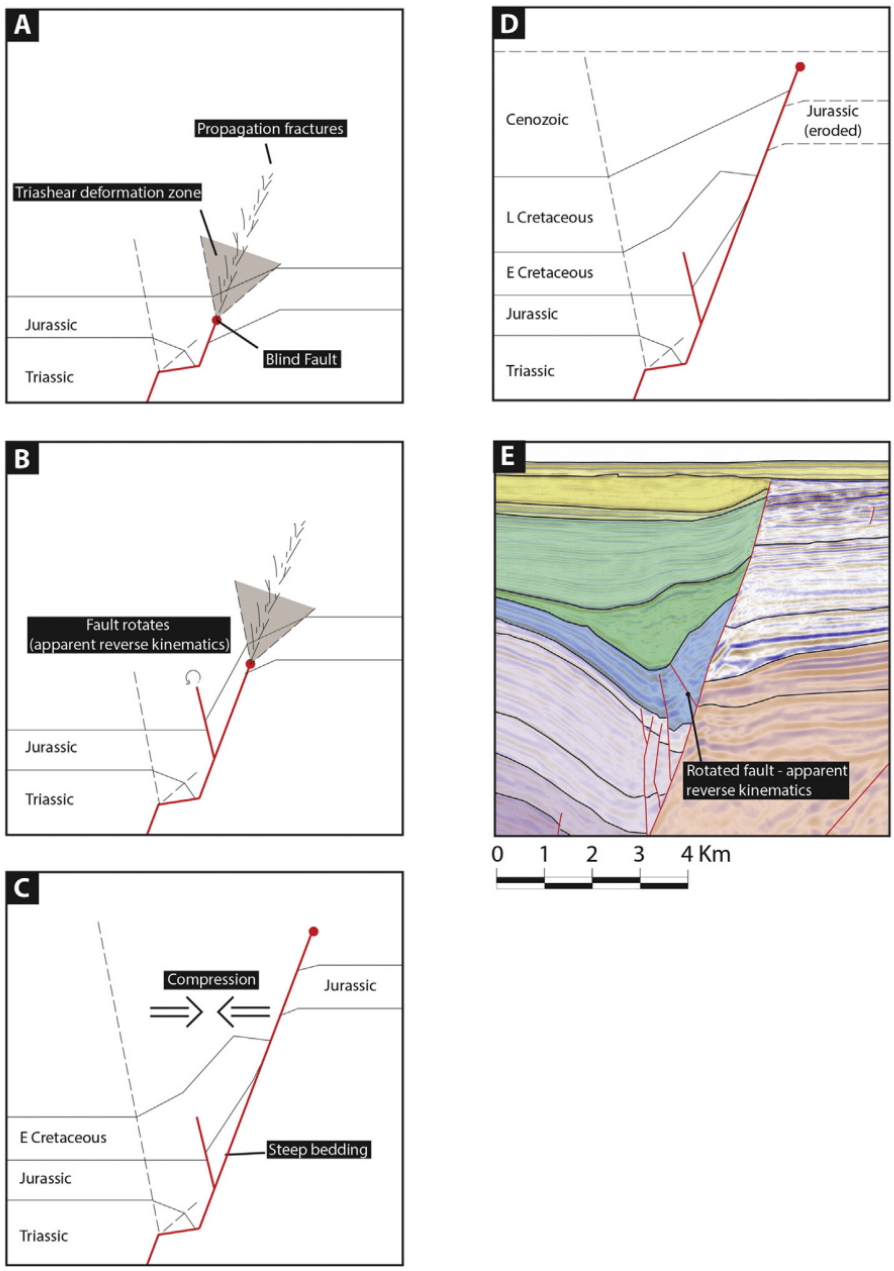

Figure 37: *Evolutionary block diagram from the Goliat structure, showing progressive growth of a blind normal fault. (A) Monocline has formed in the overlying strata. (B) Upward fault propagation and breaching of the monocline. (C) A phase of inversion affecting the hanging wall structure. (D) Final stage of evolution. (E) Final stage as interpreted seismic line of the hanging wall architecture. From Mulrooney et al. (2017).*

Conceptual forward model

To evaluate the effect of fault-propagation folding, I use a model similar to Cardozo & Brandenburg, (2014). In this model, the fault follows the trajectory of the ØFC, and the deformation is simulated by inclined shear in the backlimb, and trishear in front of the fault tip. Similar to Cardozo and Brandenburg (2014), I ran an inversion for the models that best fit the top of the pre-growth (top Sognefjord) in section 1, using a Matlab program written by

Nestor Cardozo. Figure 38 shows the best model (the one with the lowest objective function) for the top Sognefjord in section 1. The red dots are the input data (interpreted top Sognefjord), the green dots are the restored points by the best model, the blue line is the fit to the input data, and the gray line is the fit to the restored data.

Though this implementation has some problems in the backlimb since it only uses antithetic shear planes for both concave and convex upwards fault bends, resulting in a backlimb with a non-planar geometry, the best model fits nicely the synclinal structure (drag fold) near the ØFC. It also gives an initial location of the fault tip (red circle in Figure 38) just below the steeper segment of the ØFC. Interestingly, the best model suggests a fault displacement of 0.46 km, which is ~50% the displacement in the DEM models. However, the model in Figure 38 is not the only model that fits the structure, there are also other models with larger fault displacement (e.g. 0.7 to 0.8 km) that fit the structure equally well. These models have a lower location of the initial fault tip, at ~200 m below the initial fault tip in the model of Figure 38.

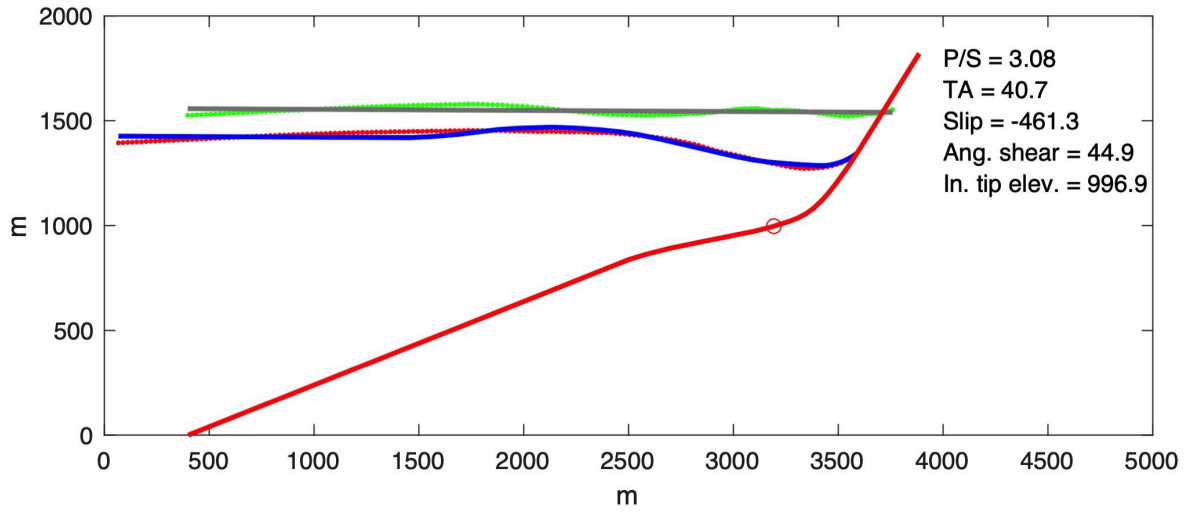

Figure 38: *Inverse modelling of the top Sognefjord in section 1. The red dots are the input horizon data (top Sognefjord), the green dots are the restored horizon, the blue line is the model fit to the horizon, and the gray line is the model fit to the restored data. The ØFC is shown in red, and the initial location of the fault tip as predicted by the model is shown as a red circle. The parameters of the best model are listed. P/S: Propagation to slip ratio, TA: Trishear angle, Ang. shear: Shear angle in backlimb, and In. tip elev.: Initial elevation of the fault tip. The y axis is elevation in the model. Matlab code by Nestor Cardozo.*

7 Conclusions

This study has analyzed the structural evolution of a basement fault-bounded fold structure in the northern North Sea, the Beta structure, using DEM modelling and kinematic modelling. The study explores how different mechanisms (e.g. rock strength and anisotropy, fault displacement, fault geometry, syn-sedimentation) affect the Beta structure geometry, displacement and strain.

The main findings are:

- The ØFC geometry changes along strike (N-S), with an accompanying change of fold structure and secondary faulting in the hanging wall.
- Based on DEM modelling, the Beta structure formed as the hanging wall sediments were translated over concave and convex upwards bends of the ØFC. The anticline of the structure relates to the convex upwards fault bend, and the forelimb and local syncline of the structure relates to the concave upwards fault bend.
- Antithetic normal faults develop from the concave upwards bends and facilitate collapse of the forelimb towards the ØFC, while synthetic reverse or normal faults develop from the convex upwards fault bends.
- The fit of the DEM to the seismic section is better in section 2 where the ØFC displays more bends. In both sections 1 and 2, the fit improves by having more distributed deformation (either by making the rocks weaker or layered anisotropic), and increasing syn-sedimentation.
- Tectonic inversion in the DEM models improves the fit to the sections, but its existence is not conclusive. None of the DEM models, including higher fault friction and tectonic inversion, can replicate the local syncline (drag folding) close to the ØFC.
- Compaction and fault propagation folding may explain the local drag fold (syncline) near the ØFC. Trishear modelling indicates that fault propagation modelling is indeed a likely process for the evolution of the Beta structure.
- The estimated displacement along the ØFC is varied: 0.8 km for inclined shear modelling, 1.0 km for DEM modelling, and 0.5 km for trishear-like modelling. However, neither the DEM nor the kinematic models are unique. It may be possible to fit the structure with a DEM model of lower fault displacement (e.g. 0.5 km), and fault propagation.

Future work

- The DEM models in this thesis are on the high fault displacement range (~1 km). With the current fault bend-folding setup (Figure 12), it would be interesting to see if one can fit the Beta structure with DEM models that require less fault displacement, similar to the one suggested by the kinematic model in Figure 38.
- Figure 38 suggests that the Beta structure maybe had a component of fault propagation folding. This could be tested by having a different setup in the DEM model, where the non-planar fault (ØFC) is at the base of the assembly, and propagates through it. The DEM is ideal for that, because both the direction and rate of fault propagation are naturally outcomes of the model.
- Once the two points above are tested, one could also look at the necessity of including tectonic inversion.

8 References

Aker, E., Kjønsberg, H., Fawad, M., & Mondol, N. H. (2021, June 23). *Estimation of thickness and layering of Johansen and Cook sandstones at the potential CO2 storage site Aurora*. Trondheim Conference on CO2 Capture, Transport and Storage.

Alghuraybi, A., Bell, R. E., & Jackson, C. A.-L. (2022). The geometric and temporal evolution of fault-related folds constrain normal fault growth patterns, Barents Sea, offshore Norway. *Basin Research*, *34*(2), 618–639. https://doi.org/10.1111/bre.12633

Baig, I., Faleide, J. I., Mondol, N. H., & Jahren, J. (2019). Burial and exhumation history controls on shale compaction and thermal maturity along the Norwegian North Sea basin margin areas. *Marine and Petroleum Geology*, *104*, 61–85. https://doi.org/10.1016/j.marpetgeo.2019.03.010

Bell, R. E., Jackson, C. A.-L., Whipp, P. S., & Clements, B. (2014). Strain migration during multiphase extension: Observations from the northern North Sea. *Tectonics*, *33*(10), 1936–1963. https://doi.org/10.1002/2014TC003551

Cardozo, N., & Brandenburg, J. P. (2014). Kinematic modeling of folding above listric propagating thrusts. *Journal of Structural Geology*, *60*, 1–12. https://doi.org/10.1016/j.jsg.2013.12.004

Cardozo, N., & Hardy, S. (Submitted). *cdem: A macOS program for discrete element modelling of tectonic structures* [Paper submitted for publication].

Ciftci, B., & Bozkurt, E. (2008). Folding of the Gediz Graben Fill, SW Turkey: Extensional and/or contractional origin? *Geodinamica Acta - GEODIN ACTA*, *21*, 145–167. https://doi.org/10.3166/ga.21.145-167

CO2 DataShare. (2022). *Smeaheia Dataset*. CO2 DataShare. https://co2datashare.org/dataset/smeaheia-dataset

Deng, C., Fossen, H., Gawthorpe, R. L., Rotevatn, A., Jackson, C. A.-L., & Fazlikhani, H. (2017). Influence of fault reactivation during multiphase rifting: The Oseberg area, northern North Sea rift. *Marine and Petroleum Geology*, *86*, 1252–1272. https://doi.org/10.1016/j.marpetgeo.2017.07.025

Deng, H., & McClay, K. (2019). Development of extensional fault and fold system: Insights from 3D seismic interpretation of the Enderby Terrace, NW Shelf of Australia. *Marine and Petroleum Geology*, *104*, 11–28. https://doi.org/10.1016/j.marpetgeo.2019.03.003

Duffy, O. B., Bell, R. E., Jackson, C. A.-L., Gawthorpe, R. L., & Whipp, P. S. (2015). Fault growth and interactions in a multiphase rift fault network: Horda Platform, Norwegian

North Sea. *Journal of Structural Geology*, *80*, 99–119. https://doi.org/10.1016/j.jsg.2015.08.015

Færseth, R. B. (1996). Interaction of Permo-Triassic and Jurassic extensional fault-blocks during the development of the northern North Sea. *Journal of the Geological Society*, *153*(6), 931–944. https://doi.org/10.1144/gsjgs.153.6.0931

Ferrill, D. A., Morris, A. P., Sims, D. W., Waiting, D. J., & Hasegawa, S. (2005). *Development of synthetic layer dip adjacent to normal faults*. https://doi.org/10.1306/1033720M853133

Fossen, H. (2016). *Structural geology*. Cambridge University Press.

Gawthorpe, R. L., Sharp, I., Underhill, J. R., & Gupta, S. (1997). Linked sequence stratigraphic and structural evolution of propagating normal faults. *Geology*, *25*(9), 795–798. https://doi.org/10.1130/0091-7613(1997)025<0795:LSSASE>2.3.CO;2

Gray, G. G., Morgan, J. K., & Sanz, P. F. (2014). Overview of continuum and particle dynamics methods for mechanical modeling of contractional geologic structures. *Journal of Structural Geology*, *59*, 19–36. https://doi.org/10.1016/j.jsg.2013.11.009

Hardy, S. (2008). Structural evolution of calderas: Insights from two-dimensional discrete element simulations. *Geology*, *36*(12), 927–930. https://doi.org/10.1130/G25133A.1

Hardy, S. (2018). Coupling a frictional-cohesive cover and a viscous substrate in a discrete element model: First results of application to thick- and thin-skinned extensional tectonics. *Marine and Petroleum Geology*, *97*. https://doi.org/10.1016/j.marpetgeo.2018.06.026

Hardy, S. (2019). Discrete element modelling of extensional, growth, fault-propagation folds. *Basin Research*, *31*(3), 584–599. https://doi.org/10.1111/bre.12335

Hardy, S., & Cardozo, N. (2021). Discrete element modelling of sedimentation and tectonics: Implications for the growth of thrust faults and thrust wedges in space and time, and the interpretation of syn-tectonic (growth) strata. *Frontiers in Earth Science*, *9*. https://doi.org/10.3389/feart.2021.742204

Hardy, S., & Finch, E. (2007). Mechanical stratigraphy and the transition from trishear to kink-band fault-propagation fold forms above blind basement thrust faults: A discrete-element study. *Marine and Petroleum Geology*, *24*(2), 75–90. https://doi.org/10.1016/j.marpetgeo.2006.09.001

Horstad, I., & Larter, S. R. (1997). Petroleum migration, alteration, and remigration within Troll Field, Norwegian North Sea. *AAPG Bulletin*, *81*. https://doi.org/10.1306/522B42F3-1727-11D7-8645000102C1865D

Indrevær, K., Gabrielsen, R. H., & Faleide, J. I. (2016). Early Cretaceous synrift uplift and tectonic inversion in the Loppa High area, southwestern Barents Sea, Norwegian shelf. *Journal of the Geological Society*, *174*, 242–254. https://doi.org/10.1144/jgs2016-066

Lauritsen, H., Kassold, S., Meneguolo, R., & Furre, A. (2018, November). *Assessing potential influence of nearby hydrocarbon production on CO2 storage at Smeaheia*. Fifth CO2 Geological Storage Workshop. https://doi.org/10.3997/2214-4609.201802970

Li, C., Yin, H., Wu, C., Zhang, Y., Zhang, J., Wu, Z., Wang, W., Jia, D., Guan, S., & Ren, R. (2021). Calibration of the Discrete Element Method and Modeling of Shortening Experiments. *Frontiers in Earth Science*, *9*, 394. https://doi.org/10.3389/feart.2021.636512

McClay, K. R., & Scott, A. D. (1991). Experimental models of hangingwall deformation in ramp-flat listric extensional fault systems. *Tectonophysics*, *188*(1), 85–96. https://doi.org/10.1016/0040-1951(91)90316-K

McHarg, S., Elders, C., & Cunneen, J. (2020). Extensional fault–related folding of the North West shelf, Western Australia. *AAPG Bulletin*, *104*(4), 913–938. https://doi.org/10.1306/08301918030

Michie, E. A. H., Mulrooney, M. J., & Braathen, A. (2021). Fault interpretation uncertainties using seismic data, and the effects on fault seal analysis: A case study from the Horda Platform, with implications for CO2 storage. *Solid Earth (SE)*, *12*(6), 1259–1286. https://doi.org/10.5194/se-12-1259-2021

Mulrooney, M. J., Leutscher, J., & Braathen, A. (2017). *A 3D structural analysis of the Goliat field, Barents Sea, Norway*.

Mulrooney, M. J., Osmond, J. L., Skurtveit, E., Faleide, J. I., & Braathen, A. (2020). Structural analysis of the Smeaheia fault block, a potential CO2 storage site, northern Horda Platform, North Sea. *Marine and Petroleum Geology*, *121*, 104598. https://doi.org/10.1016/j.marpetgeo.2020.104598

NPD. (2002). *Norwegian Petroleum Directorate FactPages*. 32/4-1. https://factpages.npd.no/no/wellbore/PageView/Exploration/All/2918

NPD. (2010). *Norwegian Petroleum Directorate FactPages*. 32/2-1. https://factpages.npd.no/no/wellbore/PageView/Exploration/All/5839

NPD. (2022). *Norwegian Petroleum Directorate FactPages*. NPD Factmaps. https://factmaps.npd.no/factmaps/3_0/

Phillips, T. B., Fazlikhani, H., Gawthorpe, R. L., Fossen, H., Jackson, C. A.-L., Bell, R. E., Faleide, J. I., & Rotevatn, A. (2019). The influence of structural inheritance and multiphase extension on rift developement, the northern North Sea. *Tectonics*, *38*(12), 4099–4126. https://doi.org/10.1029/2019TC005756

Phillips, T. B., Jackson, C., & Norcliffe, J. (2020). Pre-inversion normal fault geometry controls inversion style and magnitude, Farsund Basin, offshore southern Norway. *Solid Earth*, *11*, 1489–1510. https://doi.org/10.5194/se-11-1489-2020

Rahman, M. J., Fawad, M., Chan Choi, J., & Mondol, N. H. (2022). Effect of overburden spatial variability on field-scale geomechanical modeling of potential CO2 storage site Smeaheia, offshore Norway. *Journal of Natural Gas Science and Engineering*, *99*, 104453. https://doi.org/10.1016/j.jngse.2022.104453

Rotevatn, A., & Jackson, C. A.-L. (2014). 3D structure and evolution of folds during normal fault dip linkage. *Journal of the Geological Society*, *171*(6), 821–829. https://doi.org/10.1144/jgs2014-045

Schlische, R. W. (1995). Geometry and origin of fault-related folds in extensional settings. *AAPG Bulletin*, *79*. https://doi.org/10.1306/7834DE4A-1721-11D7-8645000102C1865D

Serck, C. S., & Braathen, A. (2019). Extensional fault and fold growth: Impact on accommodation evolution and sedimentary infill. *Basin Research*, *31*, 967–990. https://doi.org/10.1111/bre.12353

Shaw, J. H., Hook, S. C., & Sitohang, E. P. (1997). Extensional fault-bend folding and synrift deposition: An example from the Central Sumatra Basin, Indonesia. *AAPG Bulletin*, *81*. https://doi.org/10.1306/522B434D-1727-11D7-8645000102C1865D

Skuce, A. (1996). Forward modelling of compaction above normal faults: An example from the Sirte Basin, Libya. *Geological Society, London, Special Publications*, *99*, 135–146. https://doi.org/10.1144/GSL.SP.1996.099.01.11

Sofolabo, A. O., Dagogo, T., & Jephter, D. I. (2018). Velocity modelling using well data: Depth conversion "A case study of K-Field, onshore Niger Delta area." *Journal of Applied Geology and Geophysics*, *6*, 18–26. https://doi.org/10.9790/0990-0604031826

Stewart, D. J., Schwander, M., & Bolle, L. (1995). Jurassic depositional systems of the Horda platform, Norwegian north sea: Practical consequences of applying sequence stratigraphic models. *Norwegian Petroleum Society Special Publications*, *5*, 291–323. https://doi.org/10.1016/S0928-8937(06)80073-1

Vetti, V. V., & Fossen, H. (2012). Origin of contrasting Devonian supradetachment basin types in the Scandinavian Caledonides. *Geology*, *40*, 571–574. https://doi.org/10.1130/G32512.1

Whipp, P. S., Jackson, C. A.-L., Gawthorpe, R. L., Dreyer, T., & Quinn, D. (2013). Normal fault array evolution above a reactivated rift fabric; a subsurface example from the northern Horda Platform, Norwegian North Sea. *Basin Research*, *26*(4), 523–549. https://doi.org/10.1111/bre.12050

Withjack, M. O., & Peterson, E. T. (1993). Prediction of normal-fault geometries—A sensitivity analysis. *AAPG Bulletin*, *77*(11), 1860–1873. https://doi.org/10.1306/BDFF8F60-1718-11D7-8645000102C1865D

Wu, L., Thorsen, R., Ottesen, S., Meneguolo, R., Hartvedt, K., Ringrose, P., & Nazarian, B. (2021). Significance of fault seal in assessing CO2 storage capacity and containment risks – an example from the Horda Platform, northern North Sea. *Petroleum Geoscience*, *27*(3). https://doi.org/10.1144/petgeo2020-102

Xiao, H., & Suppe, J. (1992). Origin of rollover. *AAPG Bulletin*, *76*, 509–529. https://doi.org/10.1306/BDFF8858-1718-11D7-8645000102C1865D

Appendix

Appendix A – Input files

A.1 Assembly file

First ten lines of the rectangular assembly file of Model A (med.txt). The first line contains the number of elements (first entry), limits of the assembly in x (second and third entries), and limits of the assembly in y (fourth and fifth entries). These limits are in model units, so for a unit scaling of 125 m, the assembly size is 40*125 m = 5000 m by 12.5*125 m = 1562.5 m. The other lines describe the elements, each line contains the x and y coordinates of the element's center (first and second entry), and the element radius (third entry), all three in model units.

```
20872 0.0 40.0 0.0 12.5
5.137509 0.086657 0.125
0.033616 0.043560 0.050
0.213338 0.042361 0.050
0.495795 0.120048 0.125
0.722154 0.069570 0.075
0.895164 0.067993 0.100
1.122409 0.087282 0.125
1.373052 0.058630 0.100
1.520929 0.045030 0.050
```

A.2 Fault file

First ten lines of the fault geometry file of Model A (leftfault.txt). The first line contains the number of vertices defining the fault, and the other lines contain the x and y coordinates of the vertices in meters (actual scale). Notice that the fault must dip to the right, and the vertices are defined from the base to the top of the assembly.

```
85
4500 0
4460 14
4419 29
4379 43
4339 57
4299 70
4258 84
4218 98
4178 112
```

A.3 Runtime file

Input parameters to the simulation from Model A (runtime.txt). This file is made of keywords and values of parameters controlling the simulation. These are explained in Appendix B. A parameter common to all the simulations is the unit_length (unit scaling) which is set to 125 m.

```
density  2500.0

spring_constant  5544871985.0

tangent_stiff 1.0

damping_adaptor 1.0

unit_length  125.0

display_metres  2.0

total_run_time 20000.0

high_res  1

very_high_res  1

ultra_high_res  0

include_sedimentation 1

static_baselevel 1

risefromruntime 1

baselevel_rise 0.00004

include_friction  1

layered_friction 0

frictionless_walls  0

frictionless_base   0

frictionless_fault 0

include_variable_friction  0

include_variable_ductility  0

varfrict_bottom  1

varfrict_top  24

vertical_layering 0

verhor_layering 0

chess_layering 0

coeff_friction  0.25

friction_shale 0.1

```

```
base_coeff_friction  0.25

wall_coeff_friction  0.25

fault_coeff_friction 0.25

c_0  60000000.00

initial_bonding 0

add_shear_force 1

homog_bonding  1

percent_broken 0

breakpercentage  0.0250

wall_bst  0.0050

basal_bst  0.005

internal_bst  0.005

regolith  0

flexural_slip  0

walls_bonded  1

base_bonded  1

initial_equilibrate  1

equi_time 200.0

equi_nofrict  1

high_grav  0

martian  0

shoogle_media  0

shoogle_amount  0.0

displacement_sign  -1.0

regional_stretch  0

faultdipdegrees  20.00

fault_xloc  36.00

fault_offset  10.00

caldera_piston  0

dilational_void  0
```

```
dilational_displacement  0

caldera_trapdoor  0

angle_of_repose_open  0

sudden_tilt 0

tilt_angle 8.0

open_tilted_wall  0

both_walls  0

lateral_push_fromright  0

lateral_push_fromleft  0

widen_dike  0

percent_ext 0.0

finite_dike 0

top_dike 280

bottom_dike 70

unibiax_test  0

confining_pressure 0.0

overburden 0

fault_sculpt 1

irregular_fault 1

mylar_sheet 1

include_inversion 0

start_inversion 0.7

```

Appendix B – Explanation of parameters in runtime file

The table below explains the meaning of the keywords in the runtime.txt file. The rows in red are the parameters relevant for the simulations in this thesis.

Name	Meaning
density	Density of the elements
spring_constant	Spring constant
tangent_stiff	Tangent stiffness
damping_adaptor	Damping adaptor
unit_length	Unit scaling
display_metres	Display interval in meters. It says at how many meters each increment is written.
total_run_time	Total run time of the model. This controls the amount of displacement. Higher values are more displacement and vice versa.
high_resolution	Flag to indicate high resolution (0 = no, 1 = yes)
very_high_resoltution	Flag to indicate very high resolution (0 = no, 1 = yes)
ultra_high_resolution	Flag to indicate ultra high resolution (0 = no, 1 = yes)
include_sedimentation	Include synsedimentation (0 = no, 1 = yes)
static_baselevel	Static base level (0 = no, 1 = yes)
risefromruntime	Baselevel rise is from runtime file (0 = no, 1 = yes). If 0, baselevel rises as function of deformation style
baselevel_rise	Base level rise
include_friction	Include element (Coulomb) friction (0 = no, 1 = yes)
layered_friction	Include interlayer friction (0 = no, 1 = yes)
frictionless_walls	Walls have no friction (0 = no, 1 = yes)
frictionless_base	Base has no friction (0 = no, 1 = yes)
frictionless_fault	Fault has no friction (0 = no, 1 = yes)
include_variable_friction	Makes friction parameters variable (0 = no, 1 = yes)
include_variable_ductility	Makes variable layers non-frictional and viscoelastic (salt) (0 = no, 1 = yes)
varfrict_bottom	Start of variable layers - inclusive
varfrict_top	End of variable layers - inclusive
vertical_layering	Vertical layers (0 = no, 1 = yes)
verhor_layering	Vertical variable layers and horizontal upper layers (0 = no, 1 = yes)
chess_layering	Chess layering
coeff_friction	Inter-element friction
friction_shale	Inter-element friction in variable layers.
base_coeff_friction	Element-base coefficient of friction, allows weak or strong decollement
wall_coeff_friction	Wall-element friction
fault_coeff_friction	Fault-element friction
c_0	Cohesive shear force (cohesion in Mohr Coulomb)
initial_bonding	All bonds initially unbroken (0 = no, 1 = yes). 0 means all bonds are initially broken
add_shear_force	Add shear force between elements (0 = no, 1 = yes)
homog_bonding	Make bonding/cohesion (breaking strain values) homogeneous (0 = no, 1 = yes)
percent_broken	Make an initial percentage of identified bonds broken (0 = no, 1 = yes)
breakpercentage	Percentage of bonds broken
wall_bst	Wall breaking strain
basal_bst	Base breaking strain
internal_bst	Element breaking strain
regolith	Make the cap rock a regolith (0 = no, 1 = yes)
flexural_slip	Flag for flexural slip (no bonding or frictional interaction between layers) (0 = no, 1 = yes)
walls_bonded	Walls are initially bonded (0 = no, 1 = yes)
base_bonded	Base is initially bonded (0 = no, 1 = yes)
initial_equilibrate	Allow an initial period of equilibration/packing (0 = no, 1 = yes)

equi_time	Equilibration time
equi_nofrict	No friction during equilibration (0 = no, 1 = yes)
high_grav	High gravity during equilibration (0 = no, 1 = yes)
martian	Martian gravity field (0 = no, 1 = yes)
shoogle_media	Uplifts all elements by a set amount to re-organise (shoogle) the media (0 = no, 1 = yes)
shoogle_amount	Uplift in metres
displacement_sign	Displacement sign (-1.0 is extension/normal, 1.0 is contraction/reverse)
regional_stretch	Regional stretch mode test (constant heave) (0 = no, 1 = yes)
faultdipdegrees	Fault dip in degrees. For irregular fault, this is the basal dip
fault_xloc	X location of fault in unit lengths
fault_offset	Offset of second fault in unit lengths
caldera_piston	Caldera or piston (0 = no, 1 = yes)
dilational_void	Static dilational gap at the base of the model (0 = no, 1 = yes)
dilational_displacement	Opening of progressive gap at the base of the model (0 = no, 1 = yes)
caldera_trapdoor	Trapdoor-like subsidence or uplift (0 = no, 1 = yes)
angle_of_repose_open	Angle of repose calculation with an open end wall (0 = no, 1 = yes)
sudden_tilt	A sudden tilting option (0 = no, 1 = yes)
tilt_angle	Angle of tilting in degrees
open_tilted_wall	A sudden tilting option (0 = no, 1 = yes)
both_walls	Make both walls at the same time in either extension or compression, fromright and fromleft must be on (0 = no, 1 = yes)
lateral_push_fromright	Horizontal contraction or extension from right wall (0 = no, 1 = yes)
lateral_push_fromleft	Horizontal contraction or extension from left wall (0 = no, 1 = yes)
widen_dike	A special condition…
percent_ext	Percentage of global widening rate to move the base and the right wall
finite_dike	Define a block with a base dike (0 = no, 1 = yes)
top_dike	Width of top dike
bottom_dike	Width of base dike
unibiax_test	Unibiaxial or biaxial test (0 = no, 1 = yes)
confining_pressure	Confining pressure applied to walls in uni/biax test or overburden
overburden	Apply a top pressure to simulate overburden (0 = no, 1 = yes)
fault_sculpt	Sculpt the left wall to either a listric fault or an irregular fault (0 = no, 1 = yes)
irregular_fault	Irregular fault (0 = listric fault, 1 = irregular fault defined with file leftfault.txt)
mylar_sheet	Constant displacement/mylar sheet (0 = no, 1 = yes). If 0, constant heave
include_inversion	Include a phase of inversion (0 = no, 1 = yes)
start_inversion	Fraction of total time at which to start inversion

Appendix C – Running the simulation and opening the increments in cdem

To run the DEM simulations, the files med.txt, leftfault.txt, and runtime.txt along with the code executable for cdem2D (kindly provided by Stuart Hardy) should be in the same directory. The program can then be run from a terminal window by moving to the model directory:

```
cd path_to_model_directory
```

and typing the following:

```
ulimit –s 65532
```

and then:

```
nohup ./cdem2D run_description 0 &
```

If the files are correct, the program will run and produce a modelparameters.txt file, with a description of the run, then it will write the increments to the same directory as they are completed. The increments are text files numbered sequentially, e.g., modelresults0.txt, modelresults1.txt, etc. The simulations I run delivered about 1,000 increments, and they took about 3 days to run in a 12 core Mac Pro, all cores at 100%. Reading the modelparameters.txt file is important, it is a way to know the run is correct. Also, one can open the existent increments in cdem (see below), and if they are not satisfactory, one can kill the model job:

```
kill cdem2D_job_number
```

Therefore, it is not necessary to wait 3 days to check if a model delivers the right results. By the end of the simulation, all the increments along with the modelparameters.txt files are in the same folder.

To analyze the results, the macOS program cdem (Cardozo and Hardy) is used. In cdem, the cdem2D simulation can be imported by choosing the *File -> Import cdem2D simulation* menu and selecting the directory in which the increments are stored. cdem will then import each increment and display them sequentially in the *Results* view. Once the increments are

imported, any increment can be chosen and visualized, and the simulation can be played back and forth. Increments can be visualized by geometry, displacement, strain, or stress (if stress is written to the increments files; this was not the case in the thesis). The increments can be saved separately as images (to make figures) or as movies (animated GIF). I used the first option to make the figures in this thesis.